

©2016  
Binxing Yu  
ALL RIGHTS RESERVED

LIGHT MANAGEMENT IN ULTRA-THIN CONJUGATED  
POLYMER LAYERS USING PLASMONIC NANOSTRUCTURES

*by*

BINXING YU

A dissertation submitted to the

Graduate School-New Brunswick

Rutgers, the State University of New Jersey

In partial fulfillment of the requirements

For the degree of

Doctor of Philosophy

Graduate Program in Department of Chemistry & Chemical Biology

Written under the direction of

Prof. Deirdre O'Carroll

And approved by

---

---

---

---

New Brunswick, New Jersey

May. 2016

Abstract of The Dissertation

Light Management in Ultra-thin Conjugated Polymer Layers using  
Plasmonic Nanostructures

*by*

BINXING YU

Dissertation Director:

Deirdre M. O'Carroll

Conjugated polymer-based optoelectronic devices have been the focus of a growing body of investigations due to their potential for superb tuneability, high flexibility, low cost and low embodied energy. However, hurdles such as the relatively low efficiency and short operational lifetime are preventing conjugated polymer-based optoelectronic devices from being widely applied in consumer products. One of the main reasons for the low efficiency are the competing requirements for both electrically-thin conjugated polymer active layers (for efficient charge carrier transport) and optically-thick active layers (for efficient solar absorption). As a result, optimization of the device efficiency while maintaining a thin active layer has been an important pursuit for researchers in the field of organic optoelectronics. In that regard, the need for ever-thinner active layers in optoelectronic devices requires effective light trapping at deeply-sub-wavelength scales.

This thesis work focuses on the use of plasmonic nanostructures to improve light trapping in ultra-thin conjugated polymer films. First, we provide a way of applying

plasmonic nanorod arrays onto sub-50 nm polythiophene films on metallic substrates to show significant absorption enhancement ( $>10$  at the polythiophene band edge) and spectral broadening (250 nm increase) relative to polythiophene/metallic films without plasmonic nanorod arrays. Full-field electromagnetic simulations identify horizontal/longitudinal monopole antenna modes and gap modes, with the latter being the primary contributors to polythiophene absorption enhancement.

To further investigate the gap modes and their influence on the ultra-thin conjugated polymer active layer, a sphere-on-plane (SOP) system consisting of a gold nanoparticle on a conjugated polymer thin-film on a metallic substrate is fabricated and studied both theoretically and experimentally. Four different electromagnetic coupling modes are observed: a horizontal image dipole coupling mode, a vertical image dipole coupling mode and horizontal and vertical coupling modes between a localized surface plasmon resonance (LSPR) and a surface plasmon polariton (SPP). Relatively broadband spectral tuning of the modes can be achieved by modification of the thickness of either the absorptive spacer or the underlying metal film. Strong field confinement at longer wavelengths in the polythiophene spacer region, due to the vertical image dipole coupling mode and a LSPR-SPP coupling mode, is also observed in simulations and contributes to absorption enhancement. Furthermore, we find absorption enhancement in the polythiophene spacer increases with decreasing thickness, indicating the increased light trapping ability of the gold nanoparticles for ultra-thin active layers.

Dark-field optical images of SOP systems also reveal the existence of “red” particles for which the signal of the horizontal image dipole coupling mode is quenched. Subsequent defocused imaging and correlated AFM height analysis confirm this is attributed to partial-embedding of gold nanoparticles into the polythiophene spacer and leads to higher scattered light intensities at longer wavelengths. This work demonstrates that light trapping in sub-50-nm-thick semiconductor layers is possible using a “sphere-on-plane” system and offers insight into how coupling modes can be manipulated in this system.

In addition to plasmonic light trapping, energy/electron transfer in blends of organic semiconductors with cascading bandgap energies is investigated to broaden the absorption bandwidth in organic thin-films. Unary, binary, and ternary solutions of the following organic semiconductors: poly(9,9-dioctylfluorenyl-2,7-diyl) (PFO), poly(3-hexylthiophene) (P3HT), and 2,3,9,10,16,17,23,24-octakis(octyloxy)-29H,31H-phthalocyanine (OctPc), were used to prepare sub-55 nm thick unary-phase and blended thin-films. Spectroscopic analysis shows that absorption bandwidth full-width-at-half-maximum (FWHM) values increase from between 60 and 160 nm for the individual materials to greater than 450 nm for the composite thin-film ternary blend. Resonant energy or charge transfer is observed with efficiencies between 90% and 100% for the various blends. Grazing-incidence, wide-angle X-ray scattering data indicate that P3HT and OctPc exhibit the poorest blending. This correlates with the lowest donor photoluminescence quenching efficiency due to the extended separation of the P3HT chains from OctPc molecules, which is confirmed by pump-probe transient absorption spectra. It is notable

that addition of a relatively small fraction of PFO disrupts OctPc crystallinity and enables improved energy/charge transfer between P3HT and OctPc.

## **Acknowledgement**

I would like to acknowledge my mother and father, for supporting me throughout the Ph.D. study, never judging my choices and always prioritizing my future development.

I would like to acknowledge my research collaborators: Sarah Goodman, Joseph Woo, Michael Kong, Zhongkai Cheng, as well as my research group members Christopher Petoukhoff, Zeqing Shen, Catrice Carter, Benjamin Agyei-Tuffour, Gary Cheung, Jill Tracey, who have to put up with my sarcastic, eccentric *modus operandi*, and cooperate to make the group a happy yet professional place to carry out research.

I also would like to acknowledge my thesis committee members Prof. Eric Garfunkel, Prof. Teddy Asefa, Prof. Piotr Piotrowiak for the time and willingness to serve on my committee. I am also immensely grateful for my four and a half years studying under the tutelage of Prof. Deirdre M. O’Carroll – who is a talented scientist, a gifted mentor, and most importantly, an incredible person. I would like to thank her for being patient with me and always having faith in me. She is a role model to me in almost every aspect and joining her research group is the best decision I have made during the past five years. One of the most important lessons I learned from her is that to become a better researcher, I have to first become a better person. This carried me through my years in Rutgers and will always be my motto in my future life.

Chapter 2 and 3 of this dissertation were based upon two first author publications written by me; see List of Publications section below. Chapter 2 is based on the publication entitled “Light management in ultra-thin polythiophene films using plasmonic monopole nanoantennas” (B. Yu et al., *Appl. Phys. Lett.* 101, 151106, 2012), in which plasmonic nanorod arrays were fabricated and applied to ultra-thin conjugated polymer films to enhance absorption. In this work, I was responsible for sample characterization and writing the manuscript. In the follow-on study (Section 2.5), most characterization work was done by collaborators Dr. Jianhua Bao and Prof. Piotr Piotrowiak. I was responsible for fabricating the samples for that follow-on work. Chapter 3 is based on the publication titled “Mode-specific study of nanoparticle-mediated optical interactions in an absorber/metal thin-film system” (B. Yu et al., *Nanoscale* 7, 13196, 2015), in which a single-particle mediated sphere-on-plane system with a conjugated polymer spacer was studied in detail. In this work, I was responsible for fabrication of samples, design and execution of the experimental and theoretical study, interpretation of the results and writing of the manuscript. Chapter 4 is based on a collaboration with Prof. Martin Vacha at Tokyo Institute of Technology (TIT) under the International Collaboration of Chemistry (ICC). This is a shared research project funded by the National Science Foundation (NSF) & Japan Society for the Promoting of Science (JSPS) to promote international collaborations and allow exchanges of students between laboratories at Rutgers & TIT. In this work, I was responsible for fabrication of samples, and the design and execution of the experimental study. Sample fabrication and design was carried out at Rutgers and characterization was



carried out by me during a visit to the Vacha Laboratory at TIT. Chapter 5 is based on a collaboration with an undergraduate researcher, Gary Cheung, in Prof. Deirdre O’Carroll’s lab. In this work, I was responsible for time-resolved pump-probe measurements, data interpretation and I contributed to preparation of the submitted publication. I would like to thank all of the aforementioned collaborators that contributed to or supported the various aspects of my thesis work described above.

## Table of contents

Abstract of the dissertation.....	ii
Acknowledgement.....	vi
List of Tables.....	xiii
List of Illustrations.....	ix
List of Acronyms.....	ix
List of Publications.....	ix
List of Presentations.....	ix
1 Introduction.....	1
1.1 Conjugated Polymers.....	2
1.2 Thin-Film Organic Optoelectronic Devices.....	5
1.3 Surface Plasmon Resonances and Applications in OPV.....	10
1.4 “Sphere-on-plane” (SOP) system.....	14
2 Light-Management in Ultra-Thin Polythiophene Films using Plasmonic Monopole Nanoantennas.....	18
2.1 Abstract.....	18
2.2 Introduction.....	18
2.3 Methods.....	19
2.3.1 Anodic Aluminum Oxide (AAO) Membrane Preparation.....	19
2.3.2 Sample Preparation.....	20

2.3.3	UV-Visible Spectroscopy.....	21
2.3.4	Electromagnetic Simulations.....	21
2.4	Results and Discussion.....	22
2.4.1	Comparison Between Nanoantenna and Traditional Antenna.....	22
2.4.2	Sample Preparation.....	23
2.4.3	Absorption and Extinction Characterization.....	25
2.4.4	Theoretical Simulation and Mechanism Investigation.....	28
2.5	Follow-on Collaboration: Time-resolved Spectral Study of Surface-enhanced Fluorescence in a Nanocone Mediated P3HT Thin-Film System (collaboration with Dr. Jianhua Bao) .....	33
2.6	Conclusion.....	35
3	Mode-specific Study of Nanoparticle-mediated Optical Interactions in an Absorber/Metal Thin-FilmSystem.....	37
3.1	Abstract.....	37
3.2	Introduction.....	38
3.3	Method.....	41
3.3.1	Sample Fabrication.....	41
3.3.2	Dark-field (DF) Scattered Light Spectroscopy.....	42
3.3.3	Finite-difference-time-domain (FDTD) Simulations.....	42
3.4	Results and Discussion.....	43
3.5	Conclusion.....	67

4	Detailed Optical and Physical Analysis of the Sphere-on-Plane System.....	69
4.1	Introduction.....	69
4.2	Method.....	69
4.2.1	Single Nanoparticle Defocused Dark-field Imaging.....	70
4.2.2	DF/PL Simultaneous Measurements.....	70
4.3	Results and Discussion.....	71
4.3.1	Grazing-incidence Defocused Imaging.....	71
4.3.2	AuNP Embedding Investigation.....	75
4.3.3	DF/PL Measurements.....	77
4.4	Conclusion.....	80
5	Effects of Nanoscale Morphology on the Optical Properties of Organic Semiconductor Thin-Film Ternary Blends.....	82
5.1	Abstract.....	82
5.2	Introduction.....	82
5.3	Methods.....	87
5.3.1	Time-resolved Pump-probe Measurements.....	87
5.4	Results and Discussion.....	88
5.4.1	Structure and Energy Diagram of Organic Semiconductors.....	88
5.4.2	Steady-state Optical Properties.....	89
5.4.3	Transient Absorption Measurements.....	94

5.5 Conclusions.....	100
6 Conclusion and Future Work.....	102
Appendix.....	108

## List of Tables

**Table 3.1.** The proportion of “red” and “green” particles in different sample sets. Data were taken over several random areas and, in total, over 50 NPs from each sample type were analyzed. To categorize the dominant scattering color of a NP, analysis was carried out and if the percentage of red color was over 50%, the particle was categorized as “red” regardless of the percentage of green and blue.

**Table 5.1.** Donor fluorescence quenching efficiency values generated for each binary and ternary thin-film blend system calculated using Equation 5.1, along with proposed energy/charge transfer mechanism.

**Table 5.2.** The second order exponential decay fitting equation of P3HT, P3HT:OctPc binary and ternary blend films.  $\tau_1$  represents the fast component and  $\tau_2$  represents the slow component.  $A_1$  and  $A_2$  correspond to the amplitude of fast/slow component, respectively. R-square value is the coefficient of determination which indicates how close the data are to the fitted regression line.

**Table A1.** The second order exponential decay fitting equation of 50-nm-thick P3HT film with or without AuNR present.  $\tau_1$  represents the fast component and  $\tau_2$  represents the slow component.  $A_1$  and  $A_2$  correspond to the amplitude of fast/slow component, respectively.

## List of Illustrations

**Figure 1.1.** Molecular structures of some widely-studied conjugated polymer materials: (a) poly (3-hexylthiophene) (P3HT), (b) Poly(9,9-dioctylfluorene-alt-benzothiadiazole), Poly[(9,9-di-n-octylfluorenyl-2,7-diyl)-alt-(benzo[2,1,3]thiadiazol-4,8-diyl)] (F8BT), (c) poly(9,9-dioctylfluorene) (PFO), (d) poly(p-phenylene vinylene) (MEHPPV).

**Figure 1.2.** Charge collection process of a (a) thicker and (b) thinner active layer. In the thicker spacer, collection of charge is not efficient due to competing mechanism of coulomb attraction that prevents charge carriers from transporting to respective electrodes. Instead, charge recombination occurs. For thinner active layer, the distance from donor-acceptor interface is smaller than the carrier diffusion length, which allows charge carriers to transport to respective electrodes and generate photocurrent.

**Figure 1.3.** A typical SOP system with a thin dielectric spacer (<50 nm) sandwiched between a metal nanoparticle and a metal substrate. The strong electromagnetic interactions between the NP and substrate created a hot spot at the spacer area.

**Figure 2.1.** (a) A conventional receiving monopole antenna with a vertical rod, a quarter wavelength in length, placed above a conductive ground plane. When radiation is incident on the antenna at the resonant frequency a current,  $I$ , is generated in the underlying coaxial feed cable<sup>1</sup>. (b) The configuration studied in this work which consists of a vertically-oriented gold nanorod placed on an ultrathin ( $t \leq 50$  nm) semiconducting polythiophene layer on an optically-thick metal film.

**Figure 2.2.** Fabrication of vertically-oriented AuNRs on P3HT/Ag. (a) SEM image of a 600-nm-thick through-hole AAO membrane. (b) SEM image of an array of cone-shaped AuNRs deposited on a  $\sim 50$  nm P3HT thin-film on 80 nm of Ag on glass. (c) Main image: larger-area SEM image of an array of AuNRs on a P3HT/Ag film on glass; Inset: Schematic of an AuNR array on P3HT/Ag thin-film. (d) Photograph of a sample showing P3HT/Ag and AuNR/P3HT/Ag regions on a glass cover slip (P3HT concentration was  $6 \text{ g L}^{-1}$  in chloroform, giving a film thickness of  $\sim 50$  nm). (e) Bright-field reflected-light microscope image acquired within the AuNR/P3HT/Ag region shown in (d).

**Figure 2.3.** (a) The extinction spectra (acquired using a reflectance microscope coupled to a spectrometer; see inset – dotted arrows represent scattered light not collected) from a P3HT/Ag film region and an AuNR/P3HT/Ag region of the sample shown in Figure 2.2d. (b) Absorption spectra acquired using integrating sphere reflectance measurements (see inset) acquired from the same sample used in (a). Bottom left insets in (a) and (b):



Schematics of experimental setup. Solid arrows indicated the direction of incident and reflected. Dotted arrows indicated the direction of scattered light. Top right inset in (b): Enhancement in extinction/absorption for a AuNR/P3HT/Ag region relative to a P3HT/Ag region. This work was done in collaboration with Sarah Goodman.

**Figure 2.4.** Top images from left to right: Theoretical electric field intensity cross-sections through an AuNR/P3HT/Au monopole nanoantenna system under off-normal (white dashed arrow) plane wave illumination polarized in the direction indicated by the red arrow. AuNR height is 70 nm. The leftmost cross-section displays x-polarized electric field intensity at a free-space wavelength of 530 nm; the center and right-most cross-sections display z-polarized electric field intensity at free-space wavelengths of 640 nm and 740 nm, respectively. Scale bar is 20 nm. (a) Theoretical absorption spectra for AuNRs with varying height,  $h$  (bottom curve is for  $h = 20$  nm and top curve is for  $h = 160$  nm with 10 nm increases in  $h$  in between; AuNR base diameter was 60 nm). (b) Theoretical absorption spectra for the P3HT film region directly under the AuNR, for different  $h$  values. (c) Theoretical integrated absorption in the AuNR (squares) and P3HT (circles) integrated over the wavelength range 430 nm to 800 nm as a function of  $h$ . All theoretical data was acquired using 3-dimensional full-field finite-difference-time-domain simulations with plane-wave excitation at an incident angle between  $19^\circ$  to  $37^\circ$  off-normal incidence (incident angle varied within this range with excitation wavelength).

**Figure 3.1.** (a) Schematic of the AuNP/spacer/metal film sample structure. Spacer and metal film types and thicknesses ( $t_s$ ,  $t_m$ ) were varied. (b) Dark-field microscopy images of 100-nm-diameter AuNPs on a P3HT spacer on a gold film. Inset in (b): true color dark-field images of “red” and “green” particles. (c) SEM image of the same nanoparticles shown in (b). Inset in (c): higher-resolution SEM image of the middle particle in the main panel of (c).

**Figure 3.2.** Schematics of three coupling modes existing in “sphere-on-plane” systems, with a spacer in between.  $L_1$  represents horizontal image dipole coupling;  $L_2$  represents vertical image dipole coupling;  $L_3$  is horizontal LSPR and SPP coupling;  $L_4$  is vertical LSPR and SPP coupling.

**Figure 3.3.** Dark-field scattered light spectra from single AuNPs (a) in dispersion in H<sub>2</sub>O and single AuNPs on dielectric or Si substrates. (b) on a Au film (thickness of 35 nm or 100 nm) and on a PMMA spacer on a 35-nm-thick Au film. Inset in (b): true-color dark-field image of a single 100-nm-diameter AuNP on a 100-nm-thick Au film.

**Figure 3.4,** Single-particle dark-field spectroscopy of AuNP on (a) a thin P3HT spacer with underlying Au film of different thickness; (b) Ag film of different thickness. In both cases with the increase of thickness of underlying plasmonic metal substrate, the

predominant peak at  $\sim 600$  nm red shifts, which indicates a stronger interaction between vertically polarized LSPR and the image dipole. (c) Measured dark-field scattering spectra for a single AuNP on a 16-nm-thick PMMA spacer on a 35-nm-thick Au film. The peak at  $\sim 535$  nm and  $\sim 630$  nm were attributed to  $L_1$  and  $L_2$ , respectively. (d). Measured scattering spectra for a single AuNP on a PMMA film with 700 nm thickness on a 35-nm-thick Au substrate. The spectra still consisted of two major peaks. The peak at 535 nm was attributed to the LSPR peak of the AuNP ( $L_1$ ). In this case, the polarizability of the PMMA still contributed a small shift relative to the value in aqueous solution. Also, since  $t_s$  here was comparable to the wavelength of incident light, we had to consider the possible effect of Fabry-Perot resonances. This may be the reason why the particle LSPR peak was so intense—the cavity created by NP-film system was tuned to the resonance wavelength. The peak at around 630 nm was attributed to just the out-coupling of SPP modes in Au film since hardly any interaction will happen between LSPR and SPP at this distance.

**Figure 3.5.** A representative dark-field image of AuNP/PMMA(16 nm)/Au film(35 nm). Evenly distributed “green” and “red” particles can be observed. The formation of “red” particles might be attributed to the strong vertical image dipole coupling ( $L_2$ ) which can exist at sub-20-nm spacer thickness.

**Figure 3.6.** Measured dark-field scattering spectra for a single AuNP on a P3HT thin-film with (a) 16 nm (b) 50 nm and (c) 65 nm thickness on a 35-nm-thick Au substrate. Left

inset in (a) is a schematic of the system under investigation; rightmost insets in (a) show defocused dark-field images of “red” (left) and “green” (right) particles. Scale bar in rightmost insets of (a) is 2  $\mu\text{m}$ . For 16-nm- and 50-nm-thick P3HT, spectra representing AuNPs with different color under dark-field microscopy were shown (in (a) spectra 1 and 2 are from green AuNPs; spectra 3 and 4 are from red AuNPs). The grey dashed lines are the corresponding spectra from a bare P3HT/Au film region. The pink dashed line in (b) is the normalized absorption spectrum obtained from 50-nm-thick P3HT on glass. (d) Simulated scattering spectra of AuNPs on P3HT, with P3HT thicknesses ( $t_s$ ) the same as those in (a)-(c). (e) and (f): Simulated scattering spectra for a single AuNP on a (e) 20 nm and (f) 50 nm P3HT thin-film with different depth of AuNP embedding ( $t_e$ ) in the P3HT film. Insets show representative electric field intensity profiles in x-polarized ( $|E_x|^2$ ) and z-polarized ( $|E_z|^2$ ) directions and a schematic for the embedded system is shown in the top right inset in (e). Scale bars in the insets are 100 nm. The left and right sets of electric field intensity profiles are at the wavelengths corresponding to (d) the  $L_1$  and  $L_4$  modes for 50-nm-thick P3HT; (e) the  $L_1$  and  $L_2$  modes for the 8 nm embedded case; (f) the  $L_1$  and  $L_3$  modes for the 20 nm embedded case, respectively.

**Figure 3.7.** Simulated dark-field scattering spectra from an AuNP on P3HT (50 nm thick) on either a plasmonic (Au) or non-plasmonic (Ni) metal film under p- or s-polarized excitation.

**Figure 3.8.** Theoretical absorption in the P3HT region from P3HT/Au film and AuNP/P3HT/Au film structures: (a) AuNP/P3HT (20 nm)/Au film (35 nm)/Si; (b) AuNP/P3HT (50 nm)/Au film (35 nm)/Si. Inset in (a) shows the configuration of the simulated structure: the box over which integrated absorption was calculated in the P3HT spacer was 200 nm in width, 200 nm in length and 20 nm in height. (c) Comparison of enhancement in absorption by P3HT for AuNP/P3HT/Au film structures relative to the P3HT/Au film case for a 20-nm-thick and a 50-nm-thick P3HT spacer.

**Figure 4.1.** (a) Schematic diagram of the broadband defocused imaging setup. P-polarized illumination was employed to excite the vertical modes primarily.  $\Psi$  and  $\theta$  indicate out-of-plane and in-plane angles, respectively. Distribution of  $\Psi$  for AuNP/polymer spacer/Au film sphere on plane systems with various polymer spacers: (b) 20 nm-thick P3HT, (c) 20 nm-thick PFO, (d) 50 nm-thick P3HT, (e) 50 nm-thick PFO, (f) 20 nm-thick MEH-PPV. The spacers were all sandwiched between AuNPs of 100 nm diameter and a 35 nm-thick Au film. Representative defocused images are shown beside each column.

**Figure 4.2.** Dark-field images and AFM scans of the corresponding areas with 100 nm AuNP on: (a) 20 nm P3HT, (b) 20 nm PFO, (c) 50 nm P3HT, (d) 50 nm PFO on a 35-nm-thick Au film and (e) directly on glass. (f) represents the histogram of AuNP heights of different sample sets.

**Figure 4.3.** Comparison of DF and PL images of the same area for three different polymers: P3HT, PFO, MEHPPV in an SOP system. SOP samples are prepared using the same method described in Chapter 3, section 3.3.1 and were constructed as follows: 100 nm AuNP/20-nm-thick polymer spacer/35 nm Au film/glass.

**Figure 4.4.** Comparison of DF and PL images for a normally-placed and an inverted 100 nm AuNP/20 nm MEHPPV/35 nm Au film sample.

**Figure 4.5.** PL difference (a) and dark-field spectra (b) of the same AuNP. Left insets in both (a) and (b) show the corresponding DF/PL images. Right inset in (a) shows the raw PL data from the AuNP/MEHPPV/Au film area (red) and the MEHPPV/Au film area (black). The PL difference was obtained by subtracting the PL signal taken from the no NP area from that taken from the NP area.

**Figure 4.6.** (a) PL enhancement (NP area divided by no-NP area) plotted against the DF enhancement at the surface plasmon resonance peaks of DF spectra. (b) Normalized PL enhancement plotted against the surface plasmon resonance peak wavelengths.

**Figure 5.1** Chemical structures of (a) PFO, (b) P3HT, and (c) OctPc. (d) Energy level diagram of the three organic semiconductors shown in (a)-(c) with approximate HOMO, LUMO and band-gap energies shown.

**Figure 5.2.** Optical density, OD, (i.e., absorbance) and PL spectra of: (a-c) single-component; (d-f) binary blend; and (g) ternary blend thin-films with concentration of 2, 5 and 10 mg/mL for PFO, P3HT and OctPc, respectively. Dotted lines represent the laser excitation wavelength, solid black lines represent extinction spectra and solid colored lines represent PL spectra. (h) Bar chart of percentage solar absorption (relative to the AM1.5 solar spectrum) for the single component, binary blend and ternary blend thin-films. Both actual (black; determined from extinction spectra of all film types) and expected (red; determined from a summation of the individual single-phase extinction spectra) solar absorption percentages are shown. Steady-state spectra were acquired by Gary Cheung.

**Figure 5.3.** (a) Transient absorption curves for selected single phase blends, the three binary blends and the ternary blend for a pump wavelength ( $\lambda_{pump}$ ) of 530 nm and a probe wavelength ( $\lambda_{probe}$ ) of 700 nm. (b) Transient absorption profile (black symbols) with a double exponential fit (solid red line) recorded for the ternary blend at 700 nm. The rapidly evolving bleach,  $\tau_1 = 410$  fs, is the signature of the P3HT  $\rightarrow$  OctPc energy transfer. The much slower,  $\tau_2 = 17$  ps component corresponds to subsequent relaxation and recombination processes. A pump wavelength of 530 nm was employed for all transient

absorption curves. (c) and (d) Transient absorption curves for OctPC and PFO:OctPC, P3HT and PFO:P3HT binary blend for a pump wavelength ( $\lambda_{pump}$ ) of 530 nm and a probe wavelength ( $\lambda_{probe}$ ) of 700 nm, respectively.

**Figure A1.** Time-resolved fluorescence decay profile of (a) AuNR/30-nm-thick P3HT/Ag film, (b) 30-nm-thick P3HT/Ag film, (c) AuNR/50-nm-thick P3HT/Ag film, (d) 50-nm-thick P3HT/Ag film and (e) 10-nm-thick P3HT/Ag film areas. (e) shows the comparison of fluorescence decay of 30-nm-thick P3HT between AuNR area and no AuNR area. Insets are the corresponding sample area (data acquired by Jianhua Bao).

**Figure A2.** Integration of fluorescence intensity of AuNR/50-nm-thick P3HT/Ag film sample at different wavelength ranges for specific decay time.



## **List of Acronyms**

LED: Light Emitting Diode

OLED: Organic Light Emitting Diode

OPV: Organic Photovoltaics

SPR: Surface Plasmon Resonance

SPP: Surface Plasmon Polariton

SOP: Sphere-On-Plane

AAO: Anodic Aluminum Oxide

DF: Dark-field

PL: Photoluminescence

FDTD: Finite-difference-time-domain

PCE: Power Conversion Efficiency

## List of Publications

1. Yu, B.; O'Carroll, D. M., *Influence of Au nanoparticle embedding on the light in/out coupling in ultra-thin conjugated polymer films*, manuscript in preparation
2. Yu, B.; Woo, J.; Kong, M.; O'Carroll, D. M., *Mode-specific study of nanoparticle-mediated optical interactions in an absorber/metal thin-film system*, **Nanoscale**, 7, 13196 (2015) **cover article**.
3. O'Carroll, D.M.; Petoukhoff, C.E.; Kohl, J.; Yu, B.; Carter, C.M.; Goodman, S., *Conjugated polymer-based photonic nanostructures*, **Polymer Chemistry**, 4, 5181-5196 (2013).
4. Yu, B.; Goodman, S.; Abdelaziz, A.; O'Carroll, D.M., *Light-management in ultra-thin polythiophene films using plasmonic monopole nanoantennas*, **Applied Physics Letters**, 101, 151106 (2012).
5. Cheung, G. Z.; Yu, B.; Liu, M.; Gong, Z.; Kohl, G.; Petoukhoff, C. E.; Piotrowiak, P.; O'Carroll, D. M., *Broadband absorption and morphology-dependent energy transfer in organic semiconductor thin-film ternary blends*, submitted.

## **List of Presentations**

Talk – Oct. 2015, “Investigation and manipulation of plasmonic modes in a nanoparticle-mediated ultra-thin absorber/metal thin-film system”, B. Yu, D. M. O’Carroll, AVS 62<sup>nd</sup> International Symposium & Exhibition, San Jose, CA.

Poster – Dec. 2015, “Revealing the effect of electromagnetic coupling modes on the spectral response in a nanoparticle-mediated polymer/metal thin-film system”, B. Yu, D. M. O’Carroll, 2015 MRS Fall Conference, Boston, MA.

Poster – Nov. 2014, “Mode-specific study of nanoparticle-mediated optical interactions in an ultra-thin conjugated polymer/metal film system”, B. Yu, D. M. O’Carroll, 2014 MRS Fall Conference, Boston, MA.

Poster – Nov. 2014, “Green is more than just a color - Rutgers’ chronicle in sustainability”, B. Yu, J. Woo, D. M. O’Carroll, 2014 MRS Fall Conference, Boston, MA.

Poster – Dec. 2013, “Effect of single nanoparticle gap modes on the optical properties of conjugated polymer thin-films”, B. Yu, D. M. O’Carroll, 2013 MRS Fall Conference, Boston, MA.

Talk – Nov. 2012, “Light-management in ultra-thin-films on metallic ground planes using vertically-oriented nanoantennas”, B. Yu, S. Goodman, A. Abdelaziz, D. M. O’Carroll, 2012 MRS Fall Conference, Boston, MA.

Talk – Nov. 2012, “Light-management in ultra-thin conjugated polymer films on metallic ground planes”, B. Yu, S. Goodman, A. Abdelaziz, D. M. O’Carroll, 2012 ACS Fall National Meeting, Philadelphia, PA.

Poster – May. 2012, “Plasmonic nanocone monopole antennas”, B. Yu, S. Goodman, A.

Abdelaziz, D. M. O’Carroll, 2012 LSM symposium, Piscataway, NJ.

## **Chapter 1. Introduction**

Over the past several decades, the fields of optics and photonics have been the subject of intense scientific investigation and striking developments in human science and technology have occurred, with the study and manipulation of light waves being one of the important areas. By 1910, the concept of light quanta, i.e., the photon, was beginning to be well-recognized by scientists.<sup>2,3</sup> In 1923, Louis de Broglie, proposed a hypothesis that particles can hold properties of waves.<sup>4</sup> After a few years, the particle-wave duality of light was proven when the photoelectric effect proposed by Albert Einstein introduced firm evidence that waves and particles could overlap.<sup>2</sup> By 1949, high-quality optical mirrors and lenses were being fabricated to manipulate light, with Mt. Wilson's 100-inch telescope being one of the striking examples under way, which have broadened our collective understandings of the natural world.

Today, light has played a tremendously important role in modern-day industrial, medical, consumer and communication technologies. The efficient conversion of electrical energy to light through the development of solid-state, light-emitting diodes is expected to significantly improve the energy efficiency of both general lighting and portable display technologies. Also, the realization of efficient conversion of light into electricity via photovoltaic cells may also play a central role in minimizing our man-made carbon footprint to address the ever-increasing demand for the earth's finite supply of fossil fuels.

## 1.1 Conjugated Polymers

Conjugated polymers are organic molecules in which electrons are delocalized along a molecular backbone, due to p-molecular orbital overlap, which consists of a series of covalently-linked conjugated monomeric repeating units (typically >20; monomer units range from 0.2 to 2 nm in length; see Figure 1.1).<sup>5,6</sup> Conjugated polymers have superb tunability which is largely due to the easy tailoring of substitute groups (e.g., side chain length, degree of copolymerization, endcapping),<sup>7,8</sup> as well as their excellent film forming properties. By adding suitable side chains to the polymer backbone, most conjugated polymers become soluble in common organic solvents, which leads to their ease of application over large surfaces through relatively low-temperature, economically-viable coating techniques such as spin coating, spray coating, ink-jet printing and roll-to-roll processing.<sup>9-12</sup>

Functionalized conjugated polymers, like many molecular systems, possess strongly-bound Frenkel-like excitons (i.e., electron-hole pairs bound by a strong Coulomb attraction).<sup>13</sup> Exciton binding energies for most conjugated organic materials are in the range of 0.1 – 1 eV (one to two orders of magnitude greater than most inorganic semiconductors), which enables observation of excitonic transitions at room temperature.<sup>13</sup> The exciton binding energy is highly dependent on the molecular structure of conjugated polymers and on intra- and inter-chain interactions,<sup>14</sup> and can be construed as the difference between the exciton transition energy (i.e., the optical gap, which is the threshold for photons to be absorbed) and the electrical bandgap. Typically, in a conjugated-polymer-

based photovoltaic device, upon light absorption, tightly-bound excitons form inside the conjugated polymer material, and the exciton binding energy needs to be overcome for electron and holes to be separated and to transport to the electrodes to generate photocarriers.

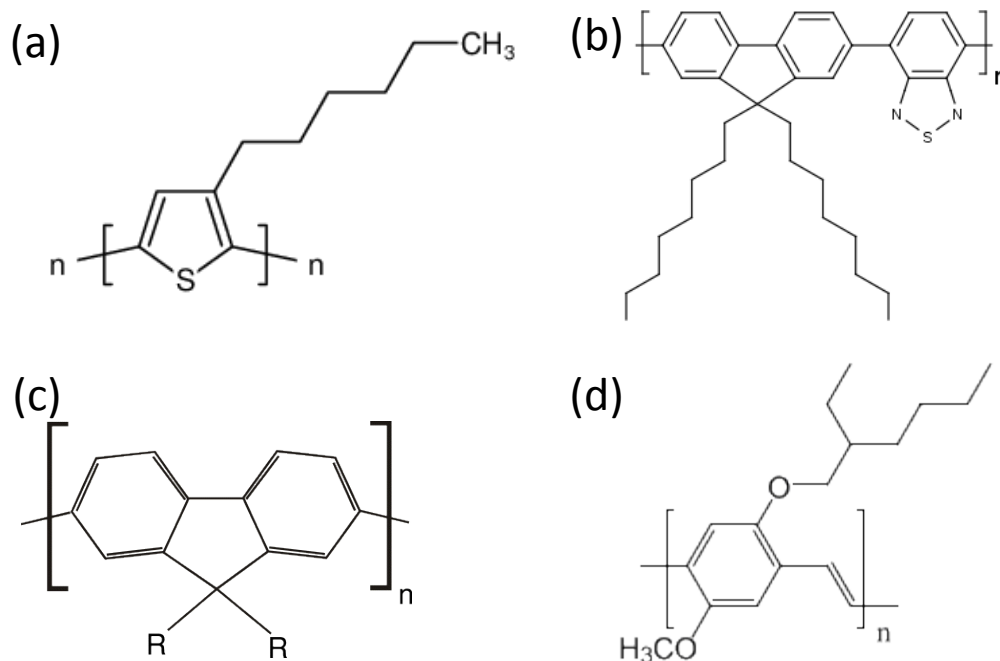


**Figure 1.1** Molecular structures of some widely-studied conjugated polymer materials: (a) poly(3-hexylthiophene) (P3HT); (b) poly(9,9-dioctylfluorene-alt-benzothiadiazole) (F8BT); (c) poly(9,9-dioctylfluorene) (PFO); (d) poly(p-phenylene vinylene) (MEHPPV).

In thin-film geometries, conjugated polymers can exhibit large absorption coefficients with values of up to  $2.8 \times 10^5 \text{ cm}^{-1}$  for polyfluorene derivatives, which are attributed to the promotion of delocalized  $\pi$ -orbital electrons in the singlet exciton ground state ( $S_0$ ) to an excited  $\pi^*$  singlet exciton state ( $S_1$ ).<sup>15</sup> However, the absorption bandwidth of conjugated

polymers is usually limited ( $\sim 150$  nm), due to the large bandgap. The large bandgap indicates the large energy difference between ground and excited state energies, which is mainly due to the difference in bond lengths of single and double bonds. Upon excitation, electrons are promoted to excited states, and double bonds become single bonds, which breaks the steric stability. This is important in aromatic systems which are often found in conjugated polymers. The large energy cost that is required for losing the aromaticity is manifested in a large bandgap.<sup>16</sup>

The polymorphism of many semicrystalline conjugated polymers provides a unique opportunity to study the influence of phase morphology on the photophysics of these materials without further chemical modification. Various phases of the polymers (e.g., semicrystalline, nematic liquid crystalline, mesomorphic) can exhibit distinct absorption spectra due to changes in the polymer molecular chain conformation and conjugation length.<sup>17-23</sup> For example, different phases of poly(9,9-dioctylfluorene) (PFO) show distinct red-shifts in the absorption edge wavelength arising from additional low-energy absorption shoulders or low-energy peaks that occur due to transition from one of the more disordered chain conformations (e.g., glassy-phase or N-phase) to one of the more ordered, extended chain conformations (e.g.,  $\alpha$ -phase,  $\alpha'$ -phase or  $\beta$ -phase).<sup>24-27</sup> It is noteworthy that higher crystallinity has been the typical target during processing because of the high carrier mobility and strong inter-molecular interaction in ordered molecular systems. However, the carrier mobility in conjugated polymers is still relatively low compared to inorganic counterparts (P3HT has a hole mobility of  $\sim 0.1$  cm<sup>2</sup>/V/s compared with amorphous Si with



electron mobility of up to  $1500 \text{ cm}^2\text{V/s}$ ),<sup>7</sup> which is due to the innate low density of conjugated polymer thin-films. The materials properties in the solid state depend on the density of the film, i.e., how closely the molecules pack together. Charge transport depends strongly on the intermolecular spacing as charge has to hop between molecules. The hopping process is strongly dependent on the intermolecular overlap of neighboring molecules and, therefore, also on the density of the molecules.

The photoluminescence (PL) quantum efficiency of conjugated polymer materials can vary substantially from values of just a few percent for polythiophene homopolymers to values approaching 80% for polyfluorenes and polyparaphenylenes.<sup>17-19</sup> The PL quantum efficiency can be related to the degree of intermolecular interactions in conjugated polymer solutions or thin-films – intermolecular interactions often lead to bimolecular emitting species, such as excimers or exciplexes, which typically coincide with lower intramolecular singlet exciton yields.<sup>20,28</sup>

## **1.2 Thin-Film Organic Optoelectronic Devices**

The ability to focus and confine light to sub-wavelength scales has the potential to benefit existing and emerging large-area optoelectronic technologies.<sup>29</sup> Thin-film optoelectronics have experienced dramatic technical advances and have cemented themselves as key enabling technologies for a myriad of industries. In particular, organic semiconductor-based thin-film optoelectronics has been the focus of a growing body of investigation in the fields of physics and chemistry for more than 50 years.<sup>30</sup> In comparison

with their inorganic counterparts, organic optoelectronic devices have certain advantages, such as, light weight, flexibility, low-energy-consumption and low-cost manufacturing, which will be discussed in detail later.

Organic thin-films have proven to be useful in a number of applications, some of them now reaching the consumer market. The most successful is the organic light-emitting diode, or OLED, which is currently used in long-lived and highly-efficient color displays. The first demonstration of an efficiently-working, organic, thin-film light-emitting diode dated back to mid-1980s by Ching Tang and Steven van Skyke at Kodak,<sup>31</sup> which used bilayer organic molecular materials resembling an inorganic semiconductor p-n junction. Later on, in 1990, Richard Friend and co-workers at Cambridge University<sup>32</sup> reported the use of solution-processed semiconducting polymer materials which provided thin-films by simply spin-casting from solution. OLEDs can maintain the same level of luminance at much lower voltage and current levels compared to their inorganic counterparts, significantly reducing the energy consumption and operation costs.<sup>31</sup> Perhaps the most exciting future development to look forward to is the flexible “all-plastic” display - an OLED display that combines a plastic substrate with organic polymer electronics. Typically, the working mechanism of an OLED is as follows: when voltage is applied across the OLED, current flows through the device. Thus, the cathode gives electrons to the emissive layer and holes are injected from the anode, forming exciton pairs in the emissive layer. When the charges in exciton pairs are combined, they give rise to light emission. The color of the light emitted depends on the energy difference of HOMO and LUMO of the emitting organic material.

The intensity or brightness of the light is determined by the amount of electrical current applied. Consequently by changing these active materials the emission color can be varied across the entire visible spectrum. However, the major challenges lies in the availability of materials with higher efficiency and longer operating lifetimes. Despite the progress made in the past decade, the OLED industry still has major hurdles to overcome. One particularly important issue is the efficiency. A molecule in its excited state  $S_1$  can undergo various competing pathways. It can relax non-radiatively in which the excitation energy is dissipated as heat to the solvent. Excited organic molecules can also relax via conversion to a triplet state, which may subsequently relax via phosphorescence or by a secondary non-radiative relaxation step. Other reasons also include the light trapping inside the semiconductor structure due to the total internal reflection. All the divergence results in the decrease of the quantum yield of OLED and, hence, decreases the efficiency. Ultimately the essence of this issue is whether we can enhance the radiative decay rate of the emissive organic molecule to a point which triumphs the non-radiative decay rate in order to enhance the device efficiency.

Not far from developments made in OLED technology are developments of organic photovoltaic (OPV) devices. The slow-down in economic growth over the past decade combined with recent world events in countries with large fossil fuel reserves has clearly demonstrated the need for the rapid development of a low cost, large scale and ‘green’ energy technology. In that regard, solar energy through photovoltaic energy conversion is the most promising candidate for long term, sustainable energy production. Photovoltaics,

in general, is a solid-state optoelectronic technology that converts sun light into electricity by employing semiconductor films, which dates back to 1954 by Chapin et al. whereby a silicon based p-n junction device with a solar power conversion efficiency of 6% was demonstrated.<sup>33</sup> This work laid the foundation for the 1<sup>st</sup> generation of photovoltaic devices which used crystalline silicon as the solar light absorbing material. Later on, with the never-ending need for higher solar power conversion efficiency, 2<sup>nd</sup> generation photovoltaic devices were developed, which employed thin-film semiconductors with direct band gaps, such as CdS, CdTe, and CuInGaSe<sub>2</sub> (CIGS), which can reach an efficiency of ~22%.<sup>34,35</sup> However, manufacturing costs and energy consumption still remain big obstacles for controlled manufacture, which motivated researchers to develop the 3<sup>rd</sup> generation photovoltaics whereby both costs (\$/w) and power conversion efficiency are optimized.

Tang et al. developed single heterojunction organic photovoltaic cells and reported in 1986 a power conversion efficiency of about 1%.<sup>36</sup> This was a milestone which opened up a new path to low-cost thin-film photovoltaics. Later, the advent in the 1990s of high-purity conjugated polymers allowed for the fabrication of organic photovoltaics with active layer materials processed directly from solution.<sup>37,38</sup> State-of-the-art solution-processed devices generally rely on the bulk heterojunction (BHJ) of polymer electron donors and fullerene electron acceptors, which involves mixing donor-acceptor materials to form the active layer of an OPV device. This structure provides large surface area between the donor-acceptor interface and significantly shortens the lengths, and, hence, the time required for excitons to transport to donor-acceptor interface.<sup>39,40</sup> Fullerene derivatives, such as [6,6]-

phenyl-C<sub>61</sub> butyric acid methyl ester (PC<sub>60</sub>BM) and [6,6]-phenyl-C<sub>71</sub>butyric acid methyl ester (PC<sub>70</sub>BM), have played a leading role as electron acceptor materials; however, they suffer from poor absorption in the visible and near-IR regions.<sup>7</sup> Recently, nonfullerene electron-accepting chromophores, such as perylene diimide, naphthalene diimide, vinazene, fluoranthene-fused imide, benzothiadiazole, rhodamine, and diketopyrrolopyrrole, have been incorporated with success in BHJ molecular and polymeric solar cells.<sup>41-45</sup> Compared with inorganic semiconductor-based photovoltaics, conjugated polymer-based photovoltaics are particularly attractive due to their potential for mechanical flexibility which can lead to light-weight, wearable or portable applications and consumer products with lower installation cost. Furthermore, low-temperature (roll to roll/inject printing) processing can reduce the energy consumption during manufacturing, further reducing the energy payback time which is defined as the time required for a power-generating device to produce the amount of energy invested during early-stage manufacturing, installation and maintenance.<sup>40</sup> In addition, the wide range of materials available and the tunable band gap by chemical doping/functionalization<sup>46</sup> propels more research and drives industrial interest in organic polymer-based photovoltaics.

However, in most cases, OPVs are not as efficient as their inorganic counterparts, and they tend to degrade more rapidly when left in air: conventional, unencapsulated OPVs have a shelf life on the order of several hours to several hundreds of hours. After state-of-the-art encapsulation to minimize the influence of oxygen and moisture, even though the operational lifetime can be greatly extended to ~5,000 hours,<sup>47,48</sup> it is still significantly

shorter than crystalline Si photovoltaics which has a guaranteed shelf life of 200,000 hours. The maximum power conversion efficiencies of contemporary OPVs is around 10% compared to 25% for crystalline Si.<sup>49-51</sup> The limited efficiency is due to a major hindrance toward the development of OPVs which is the fundamental tradeoff between light absorption and collection of photogenerated excitons. Ideally, the organic semiconductor active layer needs to be “physically thin” while “optically thick”. Only when the semiconductor active layers are “optically thick” will the incident solar radiation be fully absorbed. However, if the thickness of the active layer exceeds the carrier diffusion length, the photogenerated carrier will recombine before they are extracted by the electrodes and transform to photocurrent. Therefore, methods to trap or increase the path length of light within thin semiconductor layers have been developed to increase the effective optical density of the material while minimizing recombination.<sup>52,53</sup> With the on-going demand of ultra-thin light-harvesting active layers, broadband light trapping in a sub-wavelength-thick active layer has become an on-going topic of interest over the past few decades.

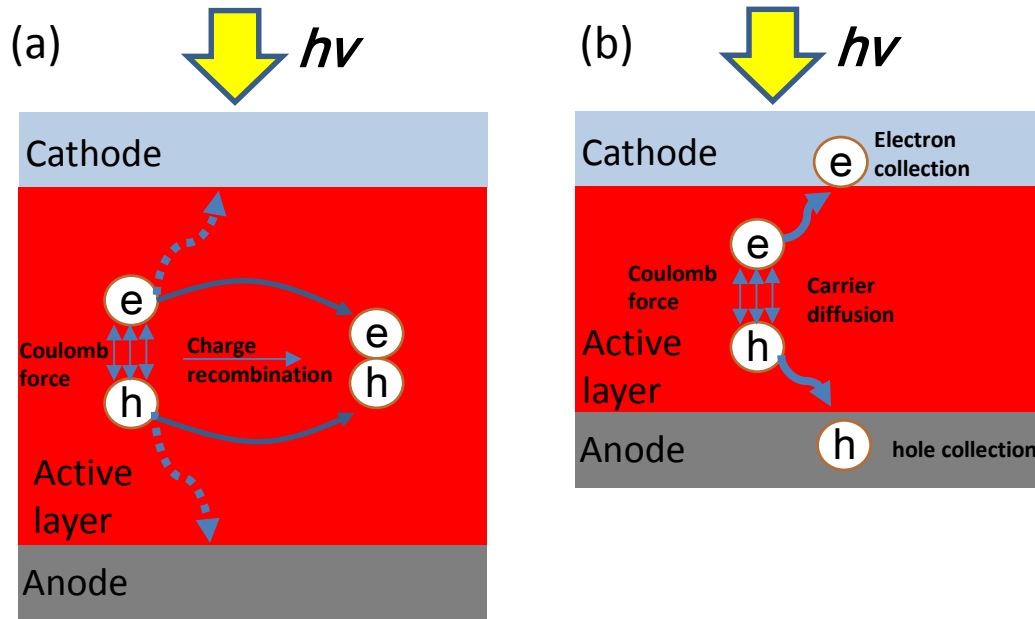


**Figure 1.2.** Charge collection process of a (a) thicker and (b) thinner active layer. In the thicker spacer, collection of charge is not efficient due to competing mechanism of coulomb attraction that prevents charge carriers from transporting to respective electrodes. Instead, charge recombination occurs. For thinner active layer, the distance from donor-acceptor interface is smaller than the carrier diffusion length, which allows charge carriers to transport to respective electrodes and generate photocurrent.

### 1.3 Surface Plasmon Resonances and Applications in OPV

Localized surface plasmons (SP) are collective oscillations of the conduction electrons in metal particles. Movement of the conduction electrons upon excitation with incident light leads to a buildup of polarized charges on the particle surface. This acts as a restoring force, and when coupled with the incident photon, allowing a resonance to occur at a particular wavelength, which is termed the localized surface plasmon resonance (LSPR) wavelength.

The corresponding LSPR wavelengths are strongly dependent on the shape and size of a metallic particle. Meanwhile, incident light that has a wavelength within the range of the LSPR wavelengths of the particles is strongly scattered or absorbed, depending on the size of the particles. The extinction of the particles is defined as the sum of the scattering and absorption. For small particles with no retardation effects, which means the polarized charge distribution would not change significantly over the course of one electromagnetic wavelength period, the particle polarizability can be adequately described using the quasistatic approximation.<sup>54</sup> In this scenario, the scattering and absorption cross sections ( $C_{sca}$  and  $C_{abs}$ , respectively) can be given by applying Mie theory<sup>55</sup>

$$C_{sca} = \frac{1}{6\pi} \left( \frac{2\pi}{\lambda} \right)^4 |\alpha|^2. \quad (1.1)$$

$$C_{abs} = \frac{2\pi}{\lambda} \text{Im}[\alpha] \quad (1.2)$$

$$\alpha = 3V(\varepsilon - 1)/(\varepsilon + 2) \quad (1.3)$$

$$Q_{sca} = C_{sca}/(C_{sca} + C_{abs}) \quad (1.4)$$

Here,  $\alpha$  is the polarizability of the particle, for a small spherical particle in vacuum. the equation for  $\alpha$  is shown in Equation 1.3, where  $V$  is the volume of the particle and  $\varepsilon$  is the relative permittivity of the metal which is dispersive (i.e., its value varies depending on the wavelength or frequency of the incident electromagnetic radiation). The scattering efficiency (or albedo),  $Q_{sca}$ , is given by Equation 1.4. We can see that the scattering intensity is highly dependent on the size of the particles - as the particle size is increased, the efficiency of scattering will dominate over the absorption efficiency. Therefore,



particles with larger size will be desirable to maximize albedo. It is also implied that when the light frequency is such that  $\varepsilon = -2$ , the particle polarizability and the absorption cross section become maximal (resonance) and under this condition a localized surface plasmon resonance (LSPR, i.e., resonant collective oscillations of conduction electrons within a metallic nanostructure) can occur.<sup>56</sup> The LSPR energy depends on the size and shape of the NP, the NP materials and the optical constants of the NP surround medium. It is worth noting that the above theory describes the scattering behavior of particles with size much smaller than the wavelength of light, which is termed Rayleigh scattering. As the size of a nanoparticle approaches approximately half the wavelength of incident light, the charge configuration would change significantly over the course of one radiation period, which means the quasistatic approximation is no longer a suitable approximation. In this scenario, the scattering behavior becomes more complicated and less dependent on the wavelength and particle size, thus, full-field electromagnetic simulations which solves Maxwell equation at every meshed points in space are essential to probe the scattering modes.

Metallic particles that are much smaller than the wavelength of light (5 - 20 nm) tend to absorb more and hence extinction is dominated by absorption in the metal particles. Absorption dissipates heat and this property is utilized in applications like solar glazing, nanoscale lithography, and therapeutic applications.<sup>57,58</sup> However, as the size of the particles increases ( $> 50$  nm),<sup>55</sup> extinction is dominated by scattering and we take advantage of this property for our application of light trapping in semiconductor thin-films. In this case, enhanced absorption in the semiconductor material takes place by an increase

of the optical path length inside the photoactive semiconductor layer, caused by the light being reemitted or scattered in different directions within the device.<sup>59</sup> Beyond certain limits, as discussed earlier, as the size of the nanoparticle approaches the wavelength of light, the quasistatic approximation is no longer appropriate, which leads to increased retardation effects and higher order multipole excitation modes and further decreases the efficiency of the scattering process. In that regard, for our investigation in Chapter 3, one of the reasons we chose 100-nm-diameter AuNPs is to optimize the albedo (ratio of scattering cross-section to extinction cross-section) while concomitantly retardation effects will not be substantial.

Plasmonic nanostructures are widely used in organic photovoltaic devices to promote absorption, thereby increasing the optical thickness of OPV materials for light harvesting.<sup>60,61</sup> When excited, the LSPR of the noble metal nanostructure results in amplified near-field intensities near the particle, and, hence, causes the creation of more excitons in the organic semiconductor. In other words, since optical absorption in the organic semiconductor layers is proportional to the electric field intensities, high local fields will lead to enhanced optical absorption of incident photons within the semiconductor region near each nanoparticle.<sup>61,62</sup> Metallic NPs of various sizes, shapes and configurations have been integrated into OPV cell architectures in order to tune and enhance the optical absorption of respective devices in a wavelength-dependent manner. Well-designed plasmonic nanostructures can greatly improve light harvesting for a range of energy applications that employ very thin layers or small absorber material volumes.

For example, arrays of discrete plasmonic nanoparticles and nanoantennas have been shown to effectively harvest and localize incident light within semiconductor thin-films and, therefore, improve light absorption and electron–hole pair generation rate at the nanoscale.<sup>61</sup>

The incorporation of NPs in OPV devices can be classified into three major categories depending on where the NPs are placed within the device: (1) embedded in the photoactive layer; (2) embedded in the buffer or charge transport layers; and (3) incorporated into or onto the electrodes.<sup>61</sup> For the former two classes, near-field and far-field effects work simultaneously: near-field light localization and trapping using plasmonic nanostructures was found to increase the generation rate of electron–hole pairs, which can lead to increased Power Conversion Efficiency (PCE) in thin-film PV devices. Whereas far-field scattering by such nanostructures placed within thin-film OPV devices has been shown to improve short-circuit current densities by ~20% to 70% through the increased effective path length of incident solar radiation within the semiconductor layer.<sup>59,63-65</sup> For plasmonic nanostructured electrodes, in addition to far-field scattering, near-field localization or trapping of incident light into guided surface plasmon polariton modes at the metal/active layer interface using nanostructured metal electrodes, such as nanotextured or nanopatterned metal thin-films and metasurfaces, can also increase the effective absorption depth of semiconductor thin-films.<sup>64,66-69</sup>

In theory, the near-field enhancement is highly dependent on the distance from the metal surface. The decay of LSPR can be best described by the following equation:<sup>70</sup>

$$R = m\Delta n \times \exp\left(-\frac{2d}{l}\right)\left[1 - \exp\left(-\frac{2d}{l}\right)\right] \quad (1.5)$$

where  $R$  is the wavelength shift or intensity change;  $m$  is the refractive index sensitivity, that is, resonant peak shift or intensity change per refractive index unit change;  $\Delta n$  is the change in refractive index of the surrounding medium, which is usually caused by adsorbents;  $d$  is the thickness of the binding layer, and  $l$  is the effective plasmon decay length. Typically, the decay length of LSPR-induced field is ~5-20 nm, depending on the shape, size and materials of the nanostructure.<sup>70</sup> For the bound surface plasmon polaritons (SPPs), the penetration depth can be treated as the decay length of the evanescent wave in z-direction. By solving the dispersion relation, the penetration depth into the dielectric,  $\delta_d$ , and metal,  $\delta_m$ , are

$$\delta_d = \frac{1}{k_0} \left| \frac{\varepsilon'_m + \varepsilon_d}{\varepsilon_d^2} \right|^{\frac{1}{2}} \quad (1.6)$$

$$\delta_m = \frac{1}{k_0} \left| \frac{\varepsilon'_m + \varepsilon_d}{\varepsilon_m'^2} \right|^{\frac{1}{2}} \quad (1.7)$$

In which  $\varepsilon'_m$  is the real part of the dielectric constant of the metal,  $\varepsilon_d$  is the dielectric constant of the dielectric. We can see both  $\delta_d$  and  $\delta_m$  are inversely proportional to the wavevector of light in free space, and highly dependent on the refractive index of the penetrated medium. In the medium of P3HT, at visible wavelength, the high absorption attenuates the penetrated evanescent wave, which makes the SPP penetration depth of only ~50 nm.<sup>71</sup> Consequently, this makes the application of the enhanced field

induced by LSPR and SPP suitable and crucial for light trapping in the sub-50-nm-thick absorptive layer.

However, one of the hurdles in the aforementioned studies with NPs embedded in the active layer and on top of an electrode of OPV devices is that the incorporation of nanostructures can greatly affect the morphology of the conjugated polymer active layer, which can be essential to the OPV device performance. In some cases, the nanostructures can act as additional recombination centers for excitons generation in the donor-acceptor blend and, hence, negatively affects the device efficiency.<sup>72,73</sup> In contrast, for our studies described in both Chapter 2 and 3, NPs were dispersed directly on the active layer, which minimizes morphology and crystallinity changes in the conjugated polymer induced by the nanostructure and simplifies the system. Additionally, the system of a nanoparticle immobilized on the conjugated polymer active layer (or spacer) constructs a simple “sphere-on-plane” (SOP) configuration.

#### **1.4 “Sphere-on-plane” (SOP) System**

“Sphere-on-plane” (SOP) systems (Figure 1.3) have recently received a significant amount of attention due to the intense electric fields localized in the gap between the NP and the metal film substrate under electromagnetic irradiation.<sup>74-81</sup> Such a SOP system effectively acts as an optical antenna structure and efficiently converts free-propagating light into strongly confined and amplified sub-wavelength resonant modes, which is due to strong coupling between localized surface plasmon resonances supported by the NPs and

the free electron oscillations in the adjacent metal film.<sup>74,75</sup> The significantly enhanced localized electric fields can be used to control light-matter interactions at the nanoscale, and plays an important role in many physical applications involving emission and collection of light, for example, scanning near field optical microscopy (SNOM),<sup>76</sup> surface enhanced raman scattering (SERS),<sup>77</sup> biosensing and chemical sensing,<sup>78-80</sup> optical tweezers.<sup>81</sup> The capability of SOP systems to focus light into a sub-50-nm thick thin film is of vital importance to thin-film based organic photovoltaics since at this length scale, conventional, diffraction-limited light trapping methods are no longer applicable.<sup>82</sup>

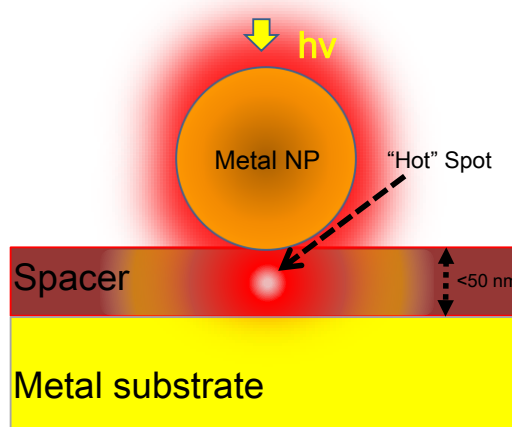


**Figure 1.3.** A typical SOP system with a thin dielectric spacer (<50 nm) sandwiched between a metal nanoparticle and a metal substrate. The strong electromagnetic interactions between the NP and substrate created a hot spot in the spacer area.

The plasmonic interaction in such SOP systems depends strongly on the particle size, the spacer thickness, and the dielectric functions of the metal, spacer and environment. Early theoretical work by Wind *et al*<sup>83</sup> and Ruppin<sup>84</sup> has provided an analytical model to

evaluate the plasmonic resonance shift of a metal nanoparticle (NP) induced by the presence of a metal substrate. Subsequently, Smith and co-workers experimentally distinguished LSPR modes and SPP modes by evanescent sensing<sup>79,85</sup> and, later, numerous studies made by Kik and co-workers<sup>86,87</sup> identified two scattering colors from SOP systems and studied the effect of local defects on the spectral response. More recently, Hutter et al<sup>88</sup> systematically studied the effect of varying the optical constants of the underlying substrate on the plasmonic field in the gap region. In all of these studies a dielectric spacer with constant refractive index in the visible range was used. Since from these prior studies it is apparent that strong electromagnetic mode confinement at tunable wavelengths can be achieved by controlling particle-substrate interactions, this property could be employed to modify absorption strength and bandwidth in a thin-film semiconductor layer sandwiched in between the particle and substrate.

To-date, the effects of different plasmonic modes in SOP systems on the absorptive function of a semiconductor spacer have not been investigated.<sup>74,79,89</sup> 错误!未找到引用源。 Also, factors such as the thickness of the underlying metal substrate, potential physical interplay between NP and spacer, and the role of SPPs supported by the metal film requires further investigation. It is notable that most of the experimental research on “sphere-on-plane” systems investigated a gap of sub-10-nm thickness. While such small thickness maximize gap mode field intensities, they are not necessarily sufficient for generating substantial absorption or emission in a semiconducting layer. Here, we employ single-particle dark-field scattering spectroscopy to observe the plasmonic modes in an absorptive

polythiophene spacer with thickness ranging from 16 nm – 65 nm in between a AuNP and a Au substrate. To elucidate the electromagnetic modes, the thicknesses of the absorptive spacer and of the Au substrate are altered and numerical simulations of representative nanoscale geometries are carried out and compared with the measured spectra. Furthermore, the effect of AuNPs on absorption in the spacer is investigated theoretically as a function of wavelength. It is noteworthy that the SOP system we reported here is the first time it has been utilized to enhance light in-coupling to ultra-thin absorptive layers, and, further, has the potential to increase the working efficiency of organic photovoltaics.



## **Chapter 2. Light-Management in Ultra-Thin Polythiophene Films using Plasmonic Monopole Nanoantennas**

### **2.1 Abstract**

Placement of vertical plasmonic nanorod arrays onto sub-50 nm polythiophene films on Ag substrates is shown to result in significant absorption enhancement ( $>10$  at the polythiophene band edge) and spectral broadening (250 nm increase) relative to polythiophene/Ag films without plasmonic nanorod arrays. Full-field electromagnetic simulations are used to identify the modes of the plasmonic nanorod array/polythiophene/metal film system. Both gap modes and longitudinal monopole antenna modes give rise to highly localized electric fields in the polythiophene film and the former mode type is the primary contributors to polythiophene absorption enhancement. This approach is suitable for large area optoelectronic applications where light management in ultrathin active layers is desired.<sup>90</sup>

### **2.2 Introduction**

The large local density of optical states in the near-field of resonant plasmonic nanoantennas can significantly increase the efficiency of semiconductor absorption and emission processes.<sup>1,91,92</sup> Additionally, the ability of plasmonic nanoantennas to localize light at sub-wavelength dimensions is synergistic with the application of ultra-thin-film semiconductor layers to photodetection, solar energy harvesting and light-emitting devices.<sup>93-96</sup> Monopole nanoantennas, which consist of vertically-oriented quarter-wavelength nanorods placed above a conductive ground plane (e.g., a metal electrode),

represent a suitable nanoantenna-semiconductor configuration because the semiconductor layer would benefit from high local field effects at the base of the nanorod.<sup>97-99</sup> The application of monopole nanoantennas for high-resolution single molecule imaging and sensing has been demonstrated in recent years and further developments may make them suitable for a variety of optoelectronic applications.<sup>1,99-102</sup>

Recently, a number of studies have begun to elucidate the mode structure and local field confinement that occurs between closely-spaced metallic nanoparticle/film monopole nanoantenna systems.<sup>103,104</sup> Both gap and dipole/multipole modes have been identified and the mode properties depend on the distance between the metal nanoparticle and the metal film, and the size of the metal nanoparticle, respectively. Both mode types could be used to modify the properties of molecules or semiconductor “spacer” layers placed between the metal nanoparticle and the metal film. Here, we study how the optical properties of ultra-thin semiconducting conjugated polymer layers are affected by nanoparticle/film monopole nanoantenna systems. Conjugated polymer layers are of interest for many ultra-thin-film optoelectronic applications because they can be readily cast at thicknesses below 50 nm by spin coating from dilute solution.

## **2.3 Methods**

### **2.3.1 Anodic Aluminum Oxide (AAO) Membrane Preparation**

The preparation of through-hole AAO membranes was carried out as follows: Firstly, a 10 x 10 mm aluminum sheet with a 600-nm-thick anodic aluminum oxide (AAO) grown on both sides (with 60 nm pores; purchased from Synkera) was completely coated on one

side with epoxy and allowed to dry. The edges of the other side were then coated with epoxy and allowed to dry leaving a  $\sim 8 \times 8$  mm region of exposed AAO. A  $120 \text{ gL}^{-1}$  solution of NaOH in deionized water (Milli Q) was prepared and a drop of this NaOH solution was deposited onto the sample to etch the exposed AAO region (10 min.). The sample was then rinsed with deionized water. Then a  $200 \text{ gL}^{-1}$  solution of  $\text{FeCl}_3$  in deionized water was prepared and the sample was floated, with the exposed aluminum side down, on the  $\text{FeCl}_3$  solution in a glass petri dish. The exposed aluminum was etched completely by the  $\text{FeCl}_3$  solution after approximately 5 hrs leaving a free-standing AAO membrane with an exposed alumina barrier layer. The sample was then rinsed in water and a solution of 8.5% wt.  $\text{H}_3\text{PO}_4$  was prepared. The sample was immersed in this solution for 43 minutes to etch the alumina barrier layer. The sample were rinsed in water and the epoxy was removed using acetone leaving a free-standing through-hole AAO membrane.

### **2.3.2 Sample Preparation**

The system consists of vertically-oriented gold nanorods (AuNR) placed above a sub-50 nm, semiconducting P3HT film on an Ag layer or “conductive ground plane” (Figure. 1). To fabricate the desired system, Au was thermally evaporated through a 600-nm-thick, through-hole nanoporous AAO membrane mask onto a substrate comprised of P3HT spin-coated from chloroform solution onto an optically-thick thermally-evaporated Ag film on glass. The AAO mask had average pore diameters of 60 nm resulting in AuNRs with comparable diameters (Figure. 2.2a-c) and the P3HT layer thickness was controlled to be equal to or less than 50 nm by altering the concentration of P3HT in chloroform from  $5 \text{ gL}^{-1}$

<sup>1</sup> to 10 gL<sup>-1</sup> The AuNRs were cone rather than cylinder shaped due to shadowing by the pores of the AAO mask during gold evaporation. The mean inter-nanocone distance was determined to be 137 nm consistent with the mean inter-AAO-nanopore distance of 136 nm. From Figure 2.2d,e it is apparent that the AuNR/P3HT/Ag region was almost black in color indicating that it had stronger absorption in comparison to the P3HT/Ag area (which exhibited the characteristic deep red color of P3HT)

### **2.3.3 UV-Visible Spectroscopy**

The extinction spectrum was measured in Caltech. The absorption spectrum was measured using a SI photonics 400 series UV-Visible spectrophotometer with a 4” integrating sphere.

Two absorption spectra of the nanoparticle regions were taken for each sample: one for ten seconds and one for fifteen seconds. The spectrum for the P3HT region of each sample was acquired for ten seconds. A reflective metal disk with a 2 mm aperture was placed over the opening of the integrating sphere while blanking with the a diffuse white reflectance tile spectralon. While measuring the spectra. This disk was attached to the integrating sphere using double sided carbon tape. The absorption was measured between a wavelength of 350 nm and 950 nm, and the crossover wavelength was set at 350 nm. Before each spectrum was taken, the spectrophotometer was blanked using. Samples were held in place over the aperture using black electrical tape. The overhead lights were turned off to eliminate the potential effects of excess light.

### **2.3.4 Electromagnetic Simulations**

Theoretical absorption spectra were computed using 3-dimensional full-field finite-difference-time-domain (3D-FDTD) software (Lumerical Solutions, Inc.). A p-polarized total-field scattered-field (TFSF) plane wave source was used at an incident angle between  $19^\circ$  to  $37^\circ$  off-normal incidence (incident angle varied within this range with excitation wavelength). A frequency-domain power monitor was placed above the tip of the nanoparticles to detect the transmission through the monitor which was used as the simulated back-scattered spectra. Theoretical integrated absorption within P3HT and AuNRs were conducted with a box of electromagnetic power monitors (in total six 2D monitors) which were located within the P3HT spacer or AuNRs. The transmission spectra through the six monitors of the box were collected and summed, which produced the integrated absorption in the box.

## **2.4 Results and Discussion**

### **2.4.1 Comparison Between Nanoantenna and Traditional Antenna**

The working mechanism of a conventional (radio wave) monopole antenna, which is shown in Figure 2.1a, illustrates that a quarter-wavelength rod with a reflection provided by a sufficiently large conductive ground plane is essentially analogous to a half-wave split dipole nanoantenna with only half of the radiated power.<sup>91</sup> Figure 2.1b is the equivalent nanoscale system studied in this work and consists of a vertically-oriented gold nanorod (AuNR) on a semiconducting poly(3-hexylthiophene) (P3HT) thin-film on an Au/Ag layer or “conductive ground plane”. It is necessary for the P3HT film to be sufficiently thin ( $\leq$

50 nm) to fully benefit from high near-field intensities that can occur when the AuNR couples with the underlying metal film.<sup>103-106</sup>

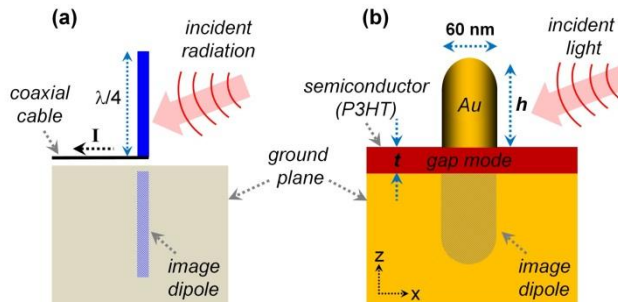


**Figure 2. 1.** (a) A conventional receiving monopole antenna with a vertical rod, a quarter wavelength in length, placed above a conductive ground plane. When radiation is incident on the antenna at the resonant frequency a current,  $I$ , is generated in the underlying coaxial feed cable.<sup>1</sup> (b) The configuration studied in this work which consists of a vertically-oriented gold nanorod placed on an ultrathin ( $t \leq 50$  nm) semiconducting polythiophene layer on an optically-thick metal film.

#### 2.4.2 Sample Preparation

AuNR/P3HT/Ag samples were fabricated by thermal evaporation of Au through a 600-nm-thick, through-hole nanoporous anodic alumina (AAO) mask onto a substrate comprised of P3HT spin-coated from chloroform solution onto an optically-thick thermally-evaporated Ag film on glass. The AAO mask had average pore diameters of 60 nm resulting in AuNR with comparable diameters (Figure 2.2a-c). The P3HT layer thickness ranged from 10 nm to 70 nm (by controlling the concentration of P3HT in chloroform to between 1 g L<sup>-1</sup> and 8 g L<sup>-1</sup>). Tilted SEM images of the as-prepared monopole

nanoantenna arrays showed relatively uniform coverage of the P3HT layer with AuNRs (Figure. 2.2b,c). The AuNRs were cone rather than cylinder shaped due to shadowing by the pores of the AAO mask during gold evaporation. The mean inter-nanocone distance was determined to be 137 nm, consistent with the mean inter-AAO-nanopore distance of 136 nm. From Figure 2.2d,e it is apparent that the AuNR/P3HT/Ag region was almost black in color indicating that it had stronger absorption in comparison to the P3HT/Ag area (which exhibited the characteristic deep red color of P3HT).

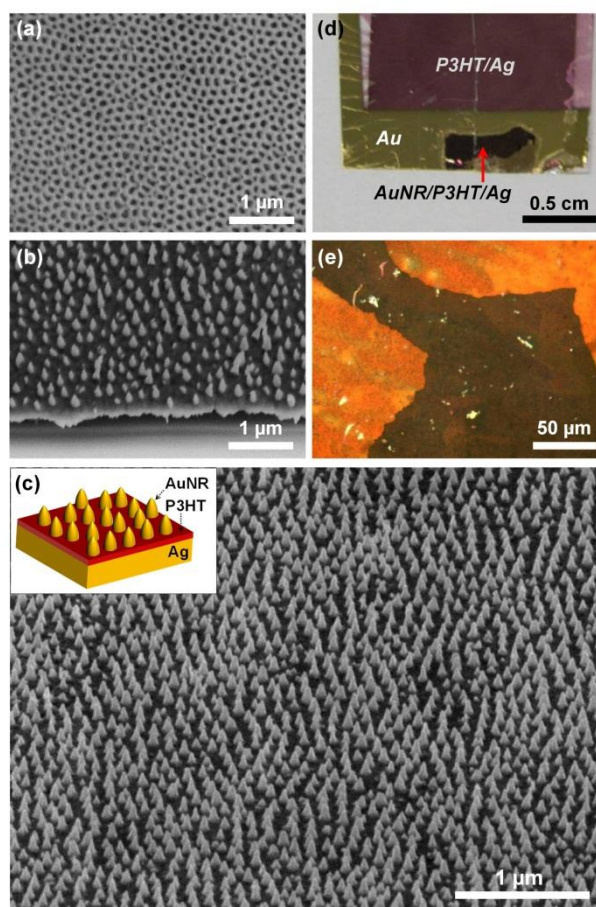


**Figure 2.2.** Fabrication of vertically-oriented AuNRs on P3HT/Ag. (a) SEM image of a 600-nm-thick through-hole AAO membrane. (b) SEM image of an array of cone-shaped AuNRs deposited on a ~ 50 nm

P3HT thin-film on 80 nm of Ag on glass. (c) Main image: larger-area SEM image of an array of AuNRs on a P3HT/Ag film on glass; Inset: Schematic of an AuNR array on P3HT/Ag thin-film. (d) Photograph of a sample showing P3HT/Ag and AuNR/P3HT/Ag regions on a glass cover slip (P3HT concentration was 6 g L<sup>-1</sup> in chloroform, giving a film thickness of ~ 50 nm). (e) Bright-field reflected-light microscope image acquired within the AuNR/P3HT/Ag region shown in (d).

### 2.4.3 Absorption and Extinction Characterization

Figure 2.3a shows extinction spectra (extinction = absorption + scattering  $\approx 1 -$  partial reflection) acquired by bright-field microscope reflection measurements (using a 50x microscope objective and halogen lamp illumination; relative to a planar Ag film) from a neat P3HT/Ag film (6 gL<sup>-1</sup> P3HT in chloroform) and an AuNR/P3HT/Ag film region (which appeared black under bright-field reflected-light microscope imaging; see Figure 2.2e). The P3HT/Ag film exhibited an extinction peak at 548 nm with a full-width-at-half-maximum (FWHM) of 135 nm. The AuNR/P3HT/Ag film region exhibited an extinction peak at ~545 nm. Compared with the known transverse Au nanoparticle surface plasmon resonance band (~520 nm in air with typical FWHM value in the range 50-100 nm),<sup>96,107</sup> the extinction band for the AuNR/P3HT/Ag film studied here was very broad (FWHM > 400 nm) and extended more than 250 nm beyond the extinction edge of the P3HT/Ag film spectrum. This could be attributed to both a degree of P3HT absorption enhancement, and absorption and scattering by the AuNR.<sup>108-110</sup> These results were further validated by absorption spectra (here, absorption = 1 – total reflection) acquired using integrating sphere



reflection measurements (i.e., the full contribution from diffuse reflection or back scattering from the sample is fully accounted for in the reflection measurement) (Figure 2.3b). The peaks resided at 546 nm and ~500 nm were for a P3HT/Ag film region and a AuNR/P3HT/Ag film region, respectively, and the FWHM for the P3HT/Ag film region was 144 nm and significantly broader for the AuNR/P3HT/Ag area (FWHM > 350 nm), values which were consistent with the extinction data. The integrating sphere absorption data suggested that the broadness of the AuNR/P3HT/Ag film spectra was predominantly due to enhanced light absorption in the sample, relative to the case without the AuNRs. Additionally, the majority of the absorption enhancement occurred at or beyond the absorption band edge of P3HT at 660 nm (Figure 2.3b), reaching enhancements greater than a factor of 10 (Figure 2.3b, inset).

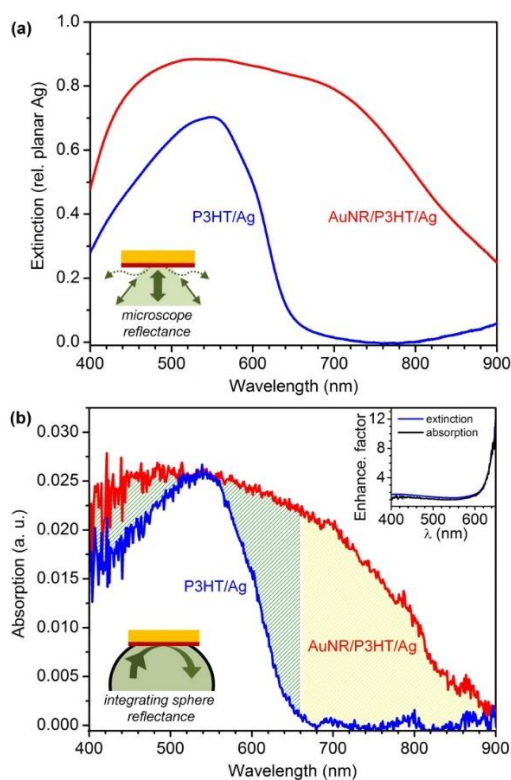


**Figure 2.3.** (a) The extinction spectra (acquired using a reflectance microscope coupled to a spectrometer; see inset – dotted arrows represent scattered light not collected) from a P3HT/Ag film region and an AuNR/P3HT/Ag region of the sample shown in Figure 2.2d. (b) Absorption spectra acquired using integrating sphere reflectance measurements (see inset) acquired from the same sample used in (a). Bottom left insets in (a) and (b): Schematics of experimental setup. Solid arrows indicated the direction of incident and reflected. Dotted arrows indicated the direction of scattered light. Top right inset in (b): Enhancement in extinction/absorption for a AuNR/P3HT/Ag region relative to a P3HT/Ag region. This work was done in collaboration with Sarah Goodman.

#### 2.4.4 Theoretical Simulation and Mechanism Investigation

To investigate the fraction of light absorbed by the AuNRs relative to the P3HT thin-film within a AuNR/P3HT/Au monopole nanoantenna configuration, theoretical full-field electromagnetic simulations of the system were carried out for a fixed P3HT thickness of 20 nm, maximum AuNR diameter of 60 nm and for various AuNR heights,  $h$ . Absorption in the AuNR and P3HT was determined by integrating the Poynting vector over a closed surface surrounding the AuNR and P3HT regions, respectively, and normalizing to that of the background. Broadband (430 - 800 nm), plane-wave illumination was employed at off-normal incidence ( $19^\circ$  -  $37^\circ$ , depending on wavelength) to excite both transverse (x-polarized) and longitudinal (z-polarized) modes of the system (see figure 2.4a, top images). The absorption spectra of AuNRs as a function of increasing  $h$  are shown in Figure 2.4a ( $h$

= 20 nm for the bottom spectrum and  $h = 160$  nm for the top spectrum with 10 nm increments in  $h$  in between). It was apparent that three main absorption bands in the 430 - 800 nm wavelength range occurred in the AuNRs arising from different mode types: one at 530 nm was attributed to the characteristic transverse localized surface plasmon resonance of AuNRs. This mode was fixed in wavelength, as expected for transverse nanorod resonances,<sup>75</sup> but became relatively more pronounced with increasing nanorod height due to the greater amount of metal present. Another mode occurring between 630 and 700 nm in wavelength could be attributed to a gap mode in the P3HT film region under the AuNR.<sup>104</sup> A third mode type occurred above 670 nm and could be attributed to longitudinal monopole nanorod antenna resonances because the mode wavelength red-shifted with increasing nanorod height. Both half-wave and higher-order longitudinal antenna resonances were expected to occur for larger nanorod aspect ratios.

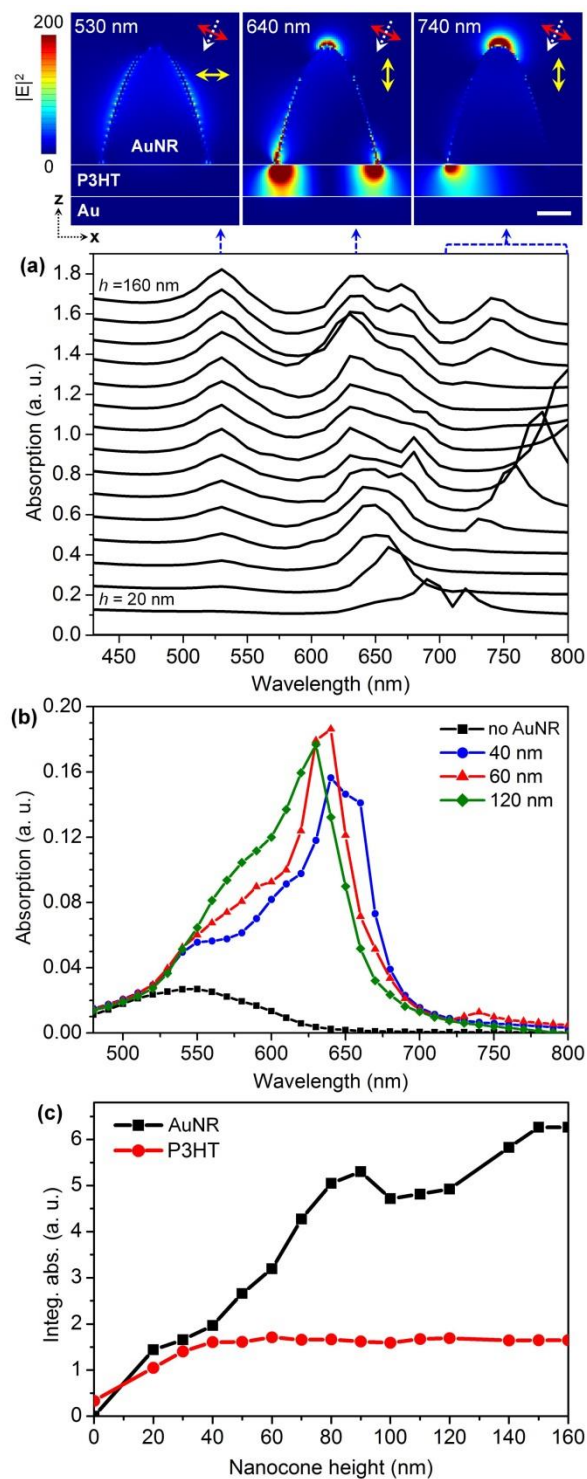


**Figure 2.4.** Top images from left to right: Theoretical electric field intensity cross-sections through an AuNR/P3HT/Au monopole nanoantenna system under off-normal (white dashed arrow) plane wave

illumination polarized in the direction indicated by the red arrow. AuNR height is 70 nm. The leftmost cross-section displays x-polarized electric field intensity at a free-space wavelength of 530 nm; the center and rightmost cross-sections display z-polarized electric field intensity at free-space wavelengths of 640 nm and 740 nm, respectively. Scale bar is 20 nm. (a) Theoretical absorption spectra for AuNRs with varying height,  $h$  (bottom curve is for  $h = 20$  nm and top curve is for  $h = 160$  nm with 10 nm increases in  $h$  in between; AuNR base diameter was 60 nm). (b) Theoretical absorption spectra for the P3HT film region directly under the AuNR, for different  $h$  values. (c) Theoretical integrated absorption in the AuNR (squares) and P3HT (circles) integrated over the wavelength range 430 nm to 800 nm as a function of  $h$ . All theoretical data was acquired using 3-dimensional full-field finite-difference-time-domain simulations with plane-wave excitation at an incident angle between  $19^\circ$  to  $37^\circ$  off-normal incidence (incident angle varied within this range with excitation wavelength).

The electric-field intensity profiles of the different mode types elucidate how the electric fields are localized around the AuNR and in the P3HT thin-film for each mode (top three images of Figure 2.4). For the transverse mode (leftmost image), light was not localized in the P3HT thin-film but at the air-AuNR interface, while for the gap mode (center image), light was predominantly localized in the P3HT region underneath the AuNR (and, to a lesser extent, at the AuNR tip). For the longitudinal mode, light was localized both in the P3HT thin-film and at the tip of the AuNR. For the latter case, the mode wavelength was above the absorption band edge of P3HT and unlikely to contribute significantly to P3HT film absorption enhancement. However, the gap mode, which

occurred at a relatively constant wavelength (due to the fixed P3HT film thickness) near the absorption band edge of P3HT, was likely to give rise to absorption enhancement in the P3HT film. Figure 2.4b is a plot of absorption spectra for a 20-nm-thick P3HT region under an AuNR for three different AuNR heights, and for the case without any AuNR. It was apparent that at the absorption edge of P3HT there was a significant increase in absorption in the P3HT thin-film at 640 nm. Additionally, the peak of P3HT absorption in the presence of the AuNR was relatively constant with  $h$ , which is consistent with gap-mode absorption enhancement in the P3HT film. Figure 2.4c is a plot of integrated absorption in an AuNR and the P3HT region directly underneath the AuNR as a function of AuNR height,  $h$  (absorption was integrated over the wavelength range 430 – 800 nm). The integrated absorption in the AuNR increased notably with increasing  $h$  due to the greater amount of metal present. While for  $h > 40$  nm the P3HT film integrated absorption saturated, suggesting that 40-nm-high AuNRs were sufficient for optimum P3HT absorption enhancement. In addition, slight oscillations in the integrated absorption of the AuNR were observed at  $h$  values of 80 nm and 160 nm indicating the contribution to AuNR absorption from height-dependent, z-polarized, longitudinal dipole/multipole resonant modes. It should be noted that the plane-wave excitation angle in the simulated data was only  $\sim 25^\circ$  off normal incidence on average, so x-polarized (transverse) modes were more strongly excited than z-polarized longitudinal modes and, therefore, contributed to a greater degree to integrated absorption by the AuNR in Figure 2.4c. For z-polarized in-plane

excitation, it is expected that gap and longitudinal modes would dominate over transverse modes as they are both polarized in the z-direction.

## **2.5 Follow-on Collaboration: Time-resolved Spectral Study of Surface-enhanced Fluorescence in a Nanocone Mediated P3HT Thin-Film System (collaboration with Dr. Jianhua Bao)**

Although the coupling between molecular transition dipole and the enhanced electric field generated by surface plasmon oscillations on the metal nanostructure can lead to enhancements of radiative decay rates, little is known about the excited state dynamics of organic molecules and polymers in close proximity to nanostructure metal surfaces and metal nanoparticle arrays. When the separation between the molecule and the structured metal surfaces is less than 10 nm, the desired enhancement competes with rapid quenching due to electron exchange and energy transfer at the interface. Experiments capable of ultrafast time resolution and sensitivity down to single molecule level are necessary in order to fully characterize such dynamics. To investigate the influence of nanorod array on the efficiency of radiative decay, time-resolved, surface-enhanced fluorescence measurements of ultrathin P3HT films in the nanorod array-mediated structure were carried out in collaboration with Dr. Jianhua Bao and Prof. Piotrowiak. Samples were prepared using the same method mentioned in section 2.3.2 with different active layer thickness (10 nm, 30 nm, 50 nm). A wide-field Kerr-gated fluorescence microscope which is capable of collecting time-resolved images and photoluminescence spectra of thin-films at the

resolution of 100 fs was used to measure the decay dynamics. The decay dynamics of P3HT can be fit into a second order exponential decay with the fast decay time constants ( $\tau_1$ ) ranging from 270 ps to 430 fs and the slow decay time ( $\tau_2$ ) at ~5 ps (Figure A1a-d and Table A1). With the presence of AuNR array, the excited states of the chromophore decayed faster in both 30-nm-thick and 50-nm-thick P3HT. In particular, in the 50-nm-thick P3HT case, the fast component was increased in amplitude for 16.47% with the aid of AuNR array. Furthermore, the PL decay was dominated by the fast component when the thickness of the P3HT film was decreased to 10 nm (Figure A1e). Based on the decay trace, we were able to conclude that the fast decay was resulted from the fluorescence quenching and direct electron-hole recombination, which was enhanced by the intense interaction between the transition dipole moment of P3HT and the metal plasmon of AuNR. The interaction also increased the fluorescence intensity of P3HT which can be seen in Figure A1f. The slow component in all decay traces corresponds to the relaxed exciton. With thinner P3HT film, the surface enhancement became stronger such that the radiative decay was significantly enhanced and few excitons can experience the relaxation to lower energy states.

The existence of two different decay components was also confirmed by the integrated fluorescence intensity profile for the AuNR/30-nm-thick P3HT/Ag film sample (Figure A2). The decay dynamics based on fluorescence spectra exhibit two different slopes for each specific area, which correspond to the fast and slow components. The time-resolved emission spectra also confirmed the wavelength dependence of fluorescence enhancement



with the presence of AuNR. At 640-690 nm, the decay was faster than the other two ranges, which is consistent with the enhanced absorption results (Figure 2.3).

## 2.6 Conclusion

In conclusion, we have studied the absorption changes and plasmonic modes arising from the placement of vertically-oriented gold nanorod arrays on sub-50-nm thick polythiophene films on silver substrates using experimental and theoretical methods. An analogy was made between the configuration under study and monopole antennas whereby vertical rods are employed to localize energy in an underlying structure. Vertical gold nanorod arrays were deposited on ultrathin polythiophene films using a large-area, lithography-free fabrication method. Both extinction and absorption characterization showed notable enhancement and broadening of the sample absorption spectra relative to undercoated polythiophene films on Ag substrates. Different modes of the system affected sample absorption to different degrees: transverse modes of the gold nanorods did not contribute significantly to absorption of light in the polythiophene layer because electric fields were localized at the sides of the nanorods. In contrast, the gap mode between the nanorod and the ground plane, and longitudinal monopole nanoantenna modes of the gold nanorod resulted in intense localized fields in the polythiophene layer directly underneath the nanorod. For the system under study, gap mode wavelengths were within the absorption band range of polythiophene and contributed most to absorption enhancement. Low aspect ratio nanorods were found to minimize absorption by the metal nanorod antennas. Follow

on, the time-resolved measurements confirmed that the fluorescence of P3HT has been enhanced with the AuNR presence and has the same wavelength dependence as absorption/extinction enhancement. This work has identified conditions for light-management in ultra-thin semiconductor films embedded in a monopole nanoantenna system. Such systems are applicable to ultra-thin optoelectronic devices where control of light interactions and mode coupling in the active layer are critical to device performance.

## **Chapter 3. Mode-specific Study of Nanoparticle-mediated Optical Interactions in an Absorber/metal Thin-Film System**

### **3.1 Abstract**

The investigation of the nanoantenna array-mediated ultrathin polymer film structure presented in Chapter 2 demonstrated that gap modes were the major contributor to absorption enhancement. However, gap modes entail various electromagnetic interactions in a sub-wavelength gap. And their intensity and energy vary depending on numerous factors such as distance between particle and metal film and the type of spacer material.

To further investigate gap modes in sphere-on-plane systems, in this chapter, we present an experimental and theoretical study of the electromagnetic interactions between a single gold nanoparticle and a thin gold substrate separated by a sub-50-nm-thick absorptive polythiophene layer, which comprises a typical sphere-on-plane (SOP) system. Single-particle dark-field scattering spectra show distinct resonance features assigned to four different modes: a horizontal image dipole coupling mode, a vertical image dipole coupling mode and horizontal and vertical coupling modes between a localized surface plasmon resonance (LSPR) and a surface plasmon polariton (SPP). Relatively broadband spectral tuning of the modes can be achieved by modification of the thickness of either the absorptive spacer or the underlying metal film. Dark-field images also reveal the existence of “red” particles for which the signal of the horizontal image dipole coupling mode is quenched. This is attributed to partial-embedding of gold nanoparticles into the

polythiophene spacer and leads to higher scattered light intensities at longer wavelengths. Full-field electromagnetic simulations show good agreement with the experimental results for the various sample conditions. Strong field confinement at longer wavelengths in the polythiophene spacer region, due to the vertical image dipole coupling mode and a LSPR-SPP coupling mode, is also observed in simulations and contributed to simulated absorption enhancement spectra. Furthermore, we find absorption enhancement in the polythiophene spacer increases with decreasing thickness, indicating the increased light trapping ability of the gold nanoparticles for ultra-thin active layers. The need for ever-thinner active layers in optoelectronic devices requires effective light trapping at deeply-sub-wavelength scales. This work demonstrates that light trapping in sub-50-nm-thick semiconductor layers is possible using a “sphere-on-plane” system and offers insight into how coupling modes can be manipulated in this system.

### **3.2 Introduction**

Conjugated polymers have been intensively studied due to their remarkable electronic and optical properties which include strong excitonic absorption, photoluminescence and electroluminescence.<sup>7,8,17,111</sup> Together with their synthetically tunable molecular structure, excellent film forming properties and solution processability, conjugated polymers have been recognized as a potential active material in next-generation optoelectronic devices.<sup>9-12,112,113</sup> However, in a polymer-based organic photovoltaic device, due to the low charge carrier mobility of these materials the polymer active layer should be much thinner than traditional inorganic semiconductor counterparts to prevent charge carriers from

recombining before they are extracted.<sup>114</sup> The restricted thickness and relatively narrow spectral absorption bandwidths compared to inorganic semiconductors have restrained the applications of conjugated polymers in photodetection and photovoltaic devices, which makes improving light-harvesting and photocarrier generation in ultra-thin conjugated polymer active layers an ongoing topic of interest in the optoelectronic community.<sup>112</sup>

”Sphere-on-plane” (SOP) systems have recently received a significant amount of attention due to the intense electric fields localized in the gap between the NP and the metal film substrate under electromagnetic irradiation.<sup>74-81</sup> Such an SOP system effectively acts as an optical antenna structure and efficiently converts free-propagating light into strongly confined and amplified sub-wavelength resonant modes, which is due to strong coupling between localized surface plasmon resonances supported by the NPs and the free electron oscillations in the adjacent metal film.<sup>74,75</sup> The significantly enhanced localized electric fields can be used to control light-matter interactions at the nanoscale, and plays an important role in many physical applications involving emission and collection of light, for example, scanning near field optical microscopy (SNOM),<sup>76</sup> surface enhanced Raman scattering (SERS),<sup>77</sup> biosensing and chemical sensing,<sup>78-80</sup> optical tweezers.<sup>81</sup>

The plasmonic interaction in such SOP systems depends strongly on the particle size, the spacer thickness, and the dielectric functions of the metal, spacer and environment. Early theoretical work by Wind *et al*<sup>83</sup> and Ruppin<sup>84</sup> has provided an analytical model to evaluate the plasmonic resonance shift of a metal nanoparticle (NP) induced by the presence of a metal substrate. Subsequently, Smith and co-workers experimentally

distinguished LSPR modes and SPP modes by evanescent sensing<sup>79,85</sup> and, later, numerous studies made by Kik and co-workers<sup>86,87</sup> identified two scattering colors from SOP systems and studied the effect of local defects on the spectral response. More recently, Hutter et al<sup>88</sup> systematically studied the effect of varying the optical constants of the underlying substrate on the plasmonic field in the gap region. In all of these studies a dielectric spacer with constant refractive index in the visible range was used. Since from these prior studies it is apparent that strong electromagnetic mode confinement at tunable wavelengths can be achieved by controlling particle-substrate interactions, this property could be employed to modify absorption strength and bandwidth in a thin-film semiconductor layer sandwiched in between the particle and substrate. To-date, the effects of different plasmonic modes on the absorptive function of a semiconductor spacer have not been widely investigated.<sup>74,79,89</sup> Also, factors such as the thickness of the underlying metal substrate, potential physical interplay between NP and spacer, the role of SPPs supported by the metal film required further investigation. It is notable that most of the experimental research on “sphere-on-plane” systems investigated a gap of sub-10-nm thickness. While such small thickness maximize gap mode field intensities, they are not necessarily sufficient for generating substantial absorption or emission in a semiconducting layer. Here, we employ single-particle dark-field scattering spectroscopy to observe the plasmonic modes in an absorptive polythiophene spacer with thickness ranging from 16 nm – 65 nm in between a AuNP and a Au substrate. At these wavelengths, gap modes are not expected to be present,<sup>86</sup> however, image-dipole modes and hybrid NP-film modes are

expected to occur.<sup>85</sup> To elucidate the electromagnetic modes, the thicknesses of the absorptive spacer and of the Au substrate were altered and numerical simulations of representative nanoscale geometries were carried out and compared with the measured spectra. Furthermore, the effect of AuNPs on absorption in the spacer was investigated theoretically as a function of wavelength.

### **3.3 Methods**

#### **3.3.1 Sample Fabrication:**

To fabricate the desired system, a thin layer of Au was deposited onto a pre-cleaned Si substrate by thermal evaporation. The Au layer was typically 35-nm or 100-nm thick and both thickness and evaporation rate were measured with a quartz crystal monitor. The resulting thickness was also confirmed using atomic force microscopy (AFM). Subsequently, a P3HT (American Dye Source.) in chloroform solution was heated to 60 °C, stirred for 15 min, sonicated for another 20 min, filtered (using a 0.2 µm filter) and then spin-coated onto the Au film. The concentration of the P3HT solution was varied to control the thickness of P3HT spacer to between 16 nm and 65 nm, as measured by AFM. After drying the samples in a desiccator for 20 min., Au nanoparticles with diameter of 100 nm (NanoComposix) were first sonicated for 20 min, then deposited onto the P3HT spacer by spin-coating at a spin rate of 2000 rpm. The Au nanoparticles had a polyvinyl pyrrolidone (PVP) coating of 1-2 nm thickness and were dispersed in isopropanol (IPA). After drying for 2 h in ambient conditions, the sample was ready for characterization.

### 3.3.2 Dark-field (DF) Scattered Light Spectroscopy:

Single-particle dark-field spectroscopy of representative geometries was performed using a Nikon Optiphot 66 optical microscope. A 75 W Xenon bulb was used as the illumination source. Scattering spectra were collected using a  $100\times$  dark field objective (N.A.= 1.25) and sent to either a color camera or the attached spectrometer (Andor SR-303i). For single-particle spectroscopy, to limit the collection area, an entrance slit width of 250  $\mu\text{m}$  was selected and vertical binning was employed. Background spectra were collected by blocking the light path directing to the spectrometer and using the same exposure time and accumulations as for the sample. Spectra of the sample were normalized to the lamp intensity by acquiring DF spectra of a diffuse reflector made of spectralon. Single-particle scattering spectra intensity ( $I$ ) were calculated using the following equation:

$$I = \frac{I_s - I_{bg}}{I_d - I_{bg}} \quad (3.1)$$

Where  $I_s$  was the scattering intensity of the selected region (i.e. AuNP on substrate),  $I_{bg}$  was the scattering intensity of the background (i.e. substrate),  $I_d$  was the scattering intensity of spectralon.

### 3.3.3 Finite-difference-time-domain (FDTD) Simulations

The back-scattering of representative geometries was simulated using commercially available FDTD software (Lumerical FDTD solutions). A p-polarized total-field scattered-



field (TFSF) plane wave source was used at  $15^\circ$  incidence angle from the surface normal to better replicate experimental conditions. Due to its broadband nature and the fixed  $k$ -vector in simulations, the angle actually varied from  $15^\circ$  to  $25^\circ$  over the wavelength range from 420 nm ~ 750 nm. A frequency-domain power monitor was placed 500 nm above the tip of the nanoparticles to detect the transmission through the monitor which was used as the simulated back-scattered spectra. A mesh override region was added to cover the TFSF source completely to ensure a constant mesh step size of 2 nm and at the interface between NP and spacer, another mesh override region with step size of 1 nm and height of 10 nm was added to ensure better accuracy. Simulations of the absorption enhancement in P3HT layer were conducted with a box of electromagnetic power monitors (in total six 2D monitors) which were located within the P3HT spacer and directly beneath the AuNP with the dimension of  $200 \text{ nm} \times 200 \text{ nm} \times t_s$  (Figure 3.7a, inset). The transmission spectra through the six monitors of the box were collected and summed, which produced the integrated absorption in the box. The dielectric functions of gold and silicon were taken from.<sup>115</sup> The dielectric function for P3HT was taken from reference.<sup>116</sup>

### 3.4 Results and Discussion

The structure of the sample is illustrated in Figure 3.1a. The relevant components of the sample were Au nanoparticles (AuNPs) with a mean diameter of  $100 \pm 7 \text{ nm}$  and a PVP coating of  $\sim 1 \text{ nm}$  on a spin-coated polymer film of either poly(3-hexylthiophene) (P3HT) or poly(methyl methacrylate) (PMMA) on a metal film with thickness ( $t_m$ ) of 35 nm or 100

nm. The polymer film had a controllable thickness ( $t_s$ ) ranging from 16 nm to 65 nm. The polymer film acted as a spacer between the metal film and the NPs, establishing a “gap” with variable thickness that could mediate the interaction between localized surface plasmon resonances (LSPRs) of the nanoparticle and image dipoles or surface plasmon polariton (SPP) modes supported by the metal film. Figure 3.1b shows a true-color dark-field microscopy image of 100-nm-diameter AuNPs deposited by spin coating from a colloidal solution onto a P3HT spacer, with 16 nm thickness, coated on a 100-nm-thick thermally evaporated Au film (Experimental). The image shows individual AuNPs that are well separated and with a density of  $10^{-2} \mu\text{m}^{-2}$ , which not only prevented inter-particle electromagnetic coupling, but also facilitated single particle spectroscopy. The AuNPs exhibited similar brightness, but had distinct scattering color variations; examples are shown in the inset as “red” and “green” particles. This color variation suggested differences in the local environment for individual particles,<sup>86</sup> which was further confirmed by the corresponding scattering spectra described below. The region of the image without AuNPs appeared dark which indicated a low scattering background from the polymer/metal films. Figure 3.1c shows scanning electron microscopy (SEM) images of AuNPs for the same sample type. Close inspection of the SEM image indicated slight roughness of the underlying film (root mean square (r.m.s) roughness of Au film was  $<0.8$  nm, r.m.s roughness of P3HT/Au film was  $<1$  nm), as shown in the inset, which could introduce variations in particle-substrate interaction.

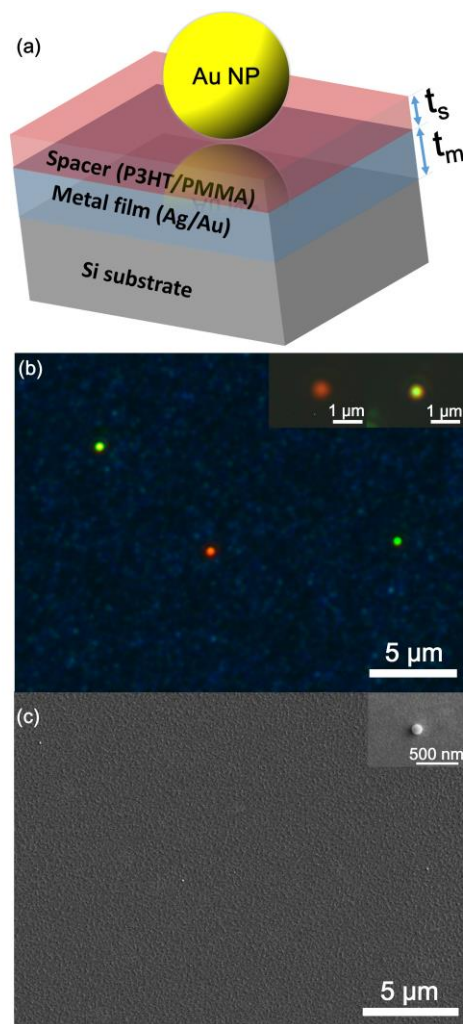


**Figure 3.1.** (a) Schematic of the AuNP/spacer/metal film sample structure. Spacer and metal film types and thicknesses ( $t_s$ ,  $t_m$ ) were varied. (b) Dark-field microscopy images of 100-nm-diameter AuNPs on a P3HT spacer on a gold film. Inset in (b): true color dark-field images of “red” and “green” particles. (c) SEM image of the same nanoparticles shown in (b). Inset in (c): higher-resolution SEM image of the middle particle in the main panel of (c).

Theoretical and experimental studies have shown that for a SOP system, the LSPR of metal nanoparticles is influenced by a polarizable substrate and results in a significant

wavelength shift of the LSPR peak.<sup>85-89,117-120</sup> One of the well-acknowledged effects is image dipole coupling which is corroborated by the work of Kik and co-workers.<sup>86,87</sup> Assuming the NP scatters as a polarizable dipole, if a horizontally oriented (i.e., parallel to the plane of the substrate) collective electron oscillation (LSPR) in the metal NP is excited, the corresponding mode is defined as a horizontal image dipole mode, as shown in Figure 3.2 as  $L_1$ . Similarly, a vertically-oriented (i.e., out-of-plane) LSPR is defined as a vertical dipole mode ( $L_2$ ). Accordingly, an LSPR of the metal NP can induce a surface charge distribution on the underlying film. In the quasistatic limit, this charge distribution can be viewed as the image dipole in response to a dipolar LSPR of a AuNP, which, in turn, affects the LSPR characteristics. The resultant coupling between the LSPR and the image dipole is termed horizontal/vertical image dipole coupling. However, another theory which is proposed by Smith *et al.* involves SPP modes.<sup>79,86,121</sup> When the substrate material has a negative real part of the dielectric constant, typically a metal film, propagating SPP modes can be supported. Under dark-field illumination, the SPPs cannot be directly excited without nanoparticles due to the inherent mismatch between the in-plane wavevectors of SPPs and those of light propagating in air.<sup>86</sup> However, the scattered light from a NP, the intense vertically polarized electric fields around a NP at off-normal incidence excitation, and the slight nanoscale roughness of thermally-evaporated metal films can enable the NP to couple a fraction of the incoming light to SPPs confined at the surface of the Au film.<sup>89</sup> These factors can also allow SPPs to be out-coupled to free space where they can be detected. Thus, propagating SPP modes can be indirectly excited and detected via a NP.<sup>118</sup>

In SOP systems both the horizontal and vertical LSPRs supported by a NP can facilitate SPP excitation depending on excitation polarization and incident angle. Horizontal LSPR-SPP and vertical LSPR-SPP coupled modes are shown in Figure 3.2 as  $L_3$  and  $L_4$ , respectively, and becomes prominent when a dielectric spacer layer is inserted between the NP and metal film. A dielectric spacer also helps to overcome the wavevector mismatch which enables direct excitation of SPP modes by off-normal incidence, and, thus, facilitates the excitation of SPPs.

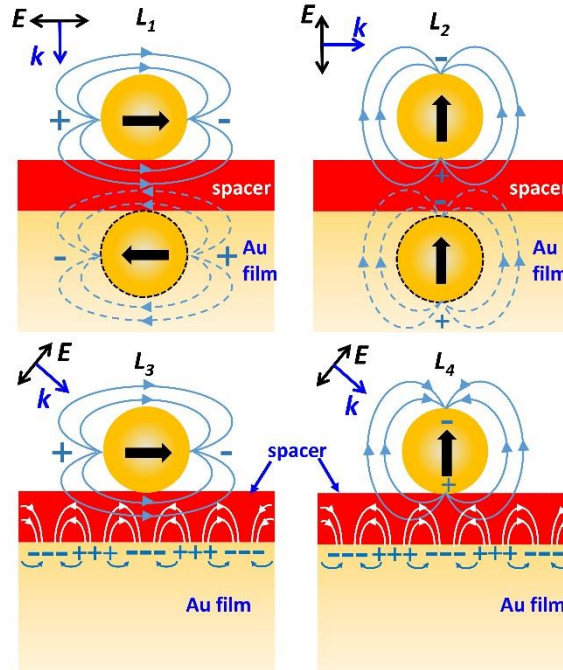


**Figure 3.2.** Schematics of three coupling modes existing in “sphere-on-plane” systems, with a spacer in between.  $L_1$  represents horizontal image dipole coupling;  $L_2$  represents vertical image dipole coupling;  $L_3$  is horizontal LSPR and SPP coupling;  $L_4$  is vertical LSPR and SPP coupling.

To investigate coupling between LSPR modes and image dipole or SPP modes, first, we deposited AuNPs on Au substrates with varying thickness ( $t_m$ ), and compared the corresponding dark-field spectra to those from AuNPs directly on dielectric substrates and to the extinction spectrum of an aqueous AuNP dispersion, see Figure 3.3a. In the experimental dark-field illumination configuration employed here for single NP spectroscopy, the incident angle was  $52^\circ$  and the incident light from the Xenon lamp was unpolarized, which could enable excitation of both horizontally-polarized and vertically-polarized LSPRs on the AuNPs. The spectra were baselined at a wavelength of 750 nm and then normalized to their peak intensity. In the colloidal dispersion in  $H_2O$ , the AuNPs exhibited a dipolar LSPR peak at 570 nm, which agrees well with the literature value of 565 nm.<sup>122</sup> The slight red-shift might be attributed to dipole retardation effects due to the relatively large NP size compared to the skin depth of Au, which reduces the resonance frequency. The LSPR peak of a single AuNP on Si occurred at a wavelength of 540 nm and was slightly red shifted compared to the case with a glass substrate (537 nm). This agrees with trends shown in the literature:<sup>88</sup> the LSPR red-shifts with substrates having higher refractive index. Also, the LSPR peak for AuNPs on Si or glass substrates was blue-shifted relative to the NPs dispersed in  $H_2O$ , probably due to the lower effective refractive index, the NP touches the dielectric substrate but also has a large air/AuNP surface area fraction.<sup>123</sup> Additionally, the full-width-half-maximum (FWHM) of the LSPR peak on Si was smaller than that on glass, which indicated better local field confinement.<sup>89</sup>

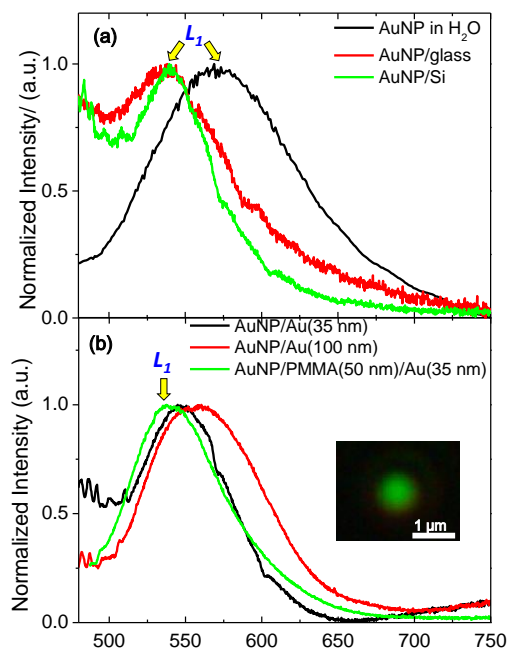


**Figure 3.3.** Dark-field scattered light spectra from single AuNPs (a) in dispersion in H<sub>2</sub>O and single AuNPs on dielectric or Si substrates. (b) on a Au film (thickness of 35 nm or 100 nm) and on a PMMA spacer on a 35-nm-thick Au film. Inset in (b): true-color dark-field image of a single 100-nm-diameter AuNP on a 100-nm-thick Au film.

Compared to the scattering properties of 100-nm-diameter AuNPs on a uniform dielectric or semiconductor film, the LSPR, and, hence, the scattering spectrum of a AuNP was altered when the AuNP was immobilized directly on a metal film, as is shown in Figure 3.3b. Here, all of the particles exhibited a green color in the true-color dark-field image (Figure 3.3b, inset). The green color and the solid circular shape indicated a horizontally polarized LSPR on the particle.<sup>124</sup> It was worth noticing that even though almost all of the

particles in this case appeared green, some of them still showed a very weak red halo surrounding the NP in the true-color dark-field images (see inset), indicative of a weak vertical image dipole which was not efficiently collected by the spectroscopy system. The spectra exhibited a broad peak at 545 nm for the 35-nm-thick Au film and this peak red shifted to 560 nm and further broadened for the 100-nm-thick Au film. For the thicker metal film, a stronger induced image dipole could occur, which increased the coupling between the horizontal LSPR and the image dipole and therefore lowered the energy of the mode. The broadening of the spectrum may have arisen from reduced electric field localization and/or contributions from the vertical LSPR mode. A spectral red shift with increasing metal thickness was also observed with a thin spacer between the AuNP and Au film and with different plasmonic metal substrates (Figure 3.4a,b). This indicates that fine-tuning of plasmonic modes can be achieved in our system by modifying the thickness or material type of the underlying metal film. When a 16-nm-thick PMMA spacer was employed a clear peak attributed to vertical image dipole coupling ( $L_2$ ) was apparent at ~630 nm in addition to the peak associated with  $L_1$  at 535 nm (Figure 3.4c). The image dipole coupling is near-field in nature, which means the coupling effect decreases exponentially as the spacer thickness is increased.<sup>123</sup> Therefore, when a 50-nm-thick PMMA spacer was employed, the vertical image dipole coupling peak was no longer apparent, indicating the lack of interaction between the NP and the metal substrate. However, if the spacer thickness was further increased to be comparable to the wavelength of incident light, both LSPR and SPP modes could couple with the cavity formed between



the NP and the film and resulted in a strong resonance peak (Figure 3.4d). The reason why  $L_2$  was not readily apparent in the dark-field spectra for AuNP on 35-nm-thick Au was attributed to strong forward scattering into the high refractive index silicon substrate.<sup>104,125</sup>

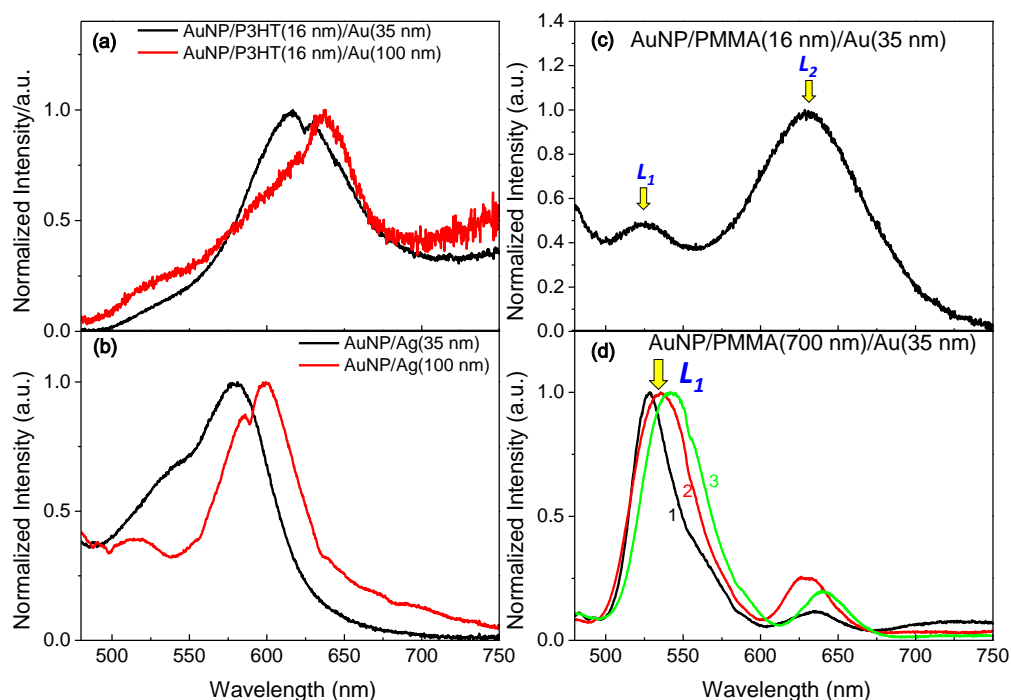


Figure 3.4, Single-particle dark-field spectroscopy of AuNP on (a) a thin P3HT spacer with underlying Au film of different thickness; (b) Ag film of different thickness. In both cases with the increase of thickness of underlying plasmonic metal substrate, the predominant peak at ~600 nm red shifts, which indicates a stronger interaction between vertically polarized LSPR and the image dipole. (c) Measured dark-field scattering spectra for a single AuNP on a 16-nm-thick PMMA spacer on a 35-nm-thick Au film. The peak at ~535 nm and ~630 nm were attributed to  $L_1$  and  $L_2$ , respectively. (d). Measured scattering spectra for a single AuNP on a PMMA film with 700 nm thickness on a 35-nm-thick Au substrate. The spectra still consisted of two major peaks. The peak at 535 nm was attributed to

the LSPR peak of the AuNP ( $L_1$ ). In this case, the polarizability of the PMMA still contributed a small shift relative to the value in aqueous solution. Also, since  $t_s$  here was comparable to the wavelength of incident light, we had to consider the possible effect of Fabry-Perot resonances. This may be the reason why the particle LSPR peak was so intense—the cavity created by NP-film system was tuned to the resonance wavelength. The peak at around 630 nm was attributed to just the out-coupling of SPP modes in Au film since hardly any interaction will happen between LSPR and SPP at this distance.

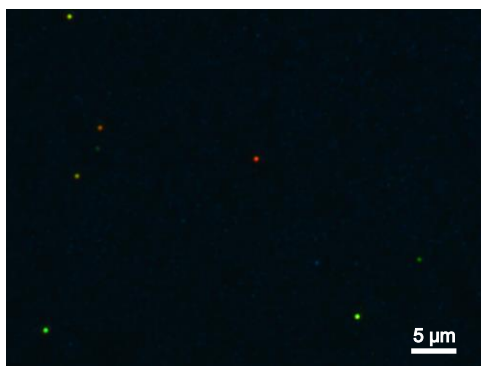
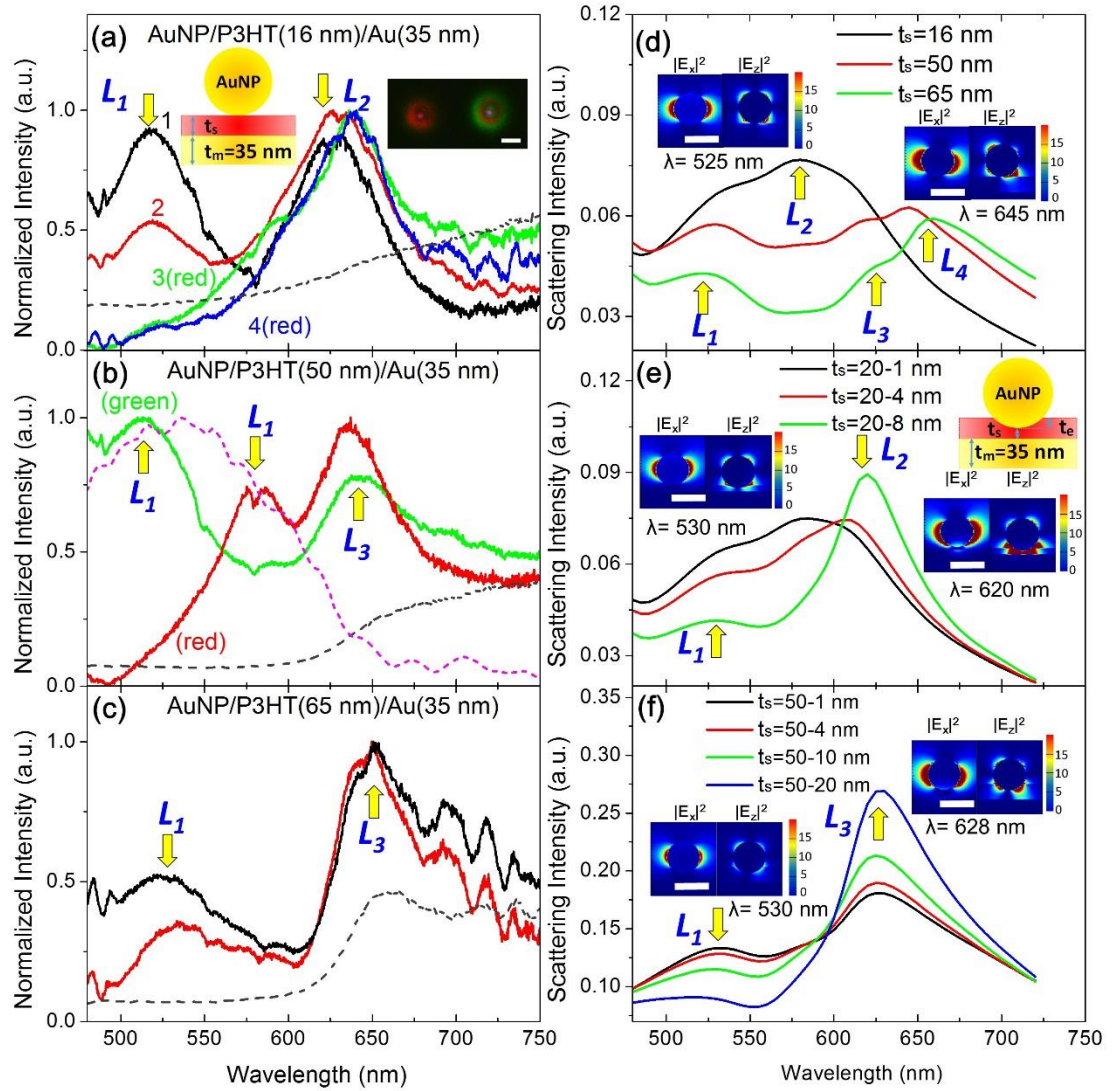


Figure 3.5. A representative dark-field image of AuNP/PMMA(16 nm)/Au film(35 nm). Evenly distributed “green” and “red” particles can be observed. The formation of “red” particles might be attributed to the strong vertical image dipole coupling ( $L_2$ ) which can exist at sub-20-nm spacer thickness.

Previous studies have shown that the thickness and material of the spacer have a great impact on the scattering properties of nanoparticles, especially in the sub-10-nm spacer thickness range.<sup>87,121,104</sup> However, in this work, since we ultimately want to investigate this structure for light trapping in thin-film optoelectronic device applications, an extremely thin active layer would compromise the absorptive function of the device. So here, we

chose sub-50-nm-thick semiconducting P3HT films as a starting point to probe the influence of the SOP system on plasmonic modes in the presence of an absorptive spacer (Fig 3.6a, left inset). Through the control of concentration and spin rate, the thickness of the spin-coated P3HT spacer ( $t_s$ ) was varied. The scattering spectra shown in Figure 3.6a were collected from 4 different AuNPs spin coated onto 16-nm-thick P3HT on top of a 35-nm-thick Au film. The spectral response varied for different AuNPs due to small variations in local environment such as film roughness, thickness and NP size and shape. The slight dip at 580 nm occurred in all spectra and was attributed to an artifact in the normalization spectrum of the Xenon lamp illumination. The particles on P3HT/Au could be divided into two groups (Table 3.1). One group of particles was relatively green in color in the true-color dark-field image, and showed two distinct scattering peaks located at wavelengths of approximately 520 nm and 630 nm. The shorter wavelength peak was attributed to horizontal image dipole coupling ( $L_1$ ). The longer wavelength peak usually had a splitting of around 10 nm and a shoulder at  $\sim 600$  nm can be observed in some cases. This was attributed primarily to vertical image dipole coupling ( $L_2$ ) and contributions from LSPR-SPP coupled modes ( $L_3$  or  $L_4$ ). The other kind of particles had a dark red appearance, and for this group, there was one predominant peak located at  $\sim 640$  nm, which was red-shifted by  $\sim 10$  nm compared with the long-wavelength peak in the spectra of green particles. Similar “red” and “green” particles were observed when P3HT was replaced by PMMA with similar thickness (Figure 3.5). Since the scattered light from both horizontal and vertical dipoles was focused into a single Airy disk on the focal plane of the dark-field

microscope objective, an aberration is needed in the imaging system to resolve each dipole and study their respective contributions.<sup>126,127</sup> The right inset in Figure 3.6a shows defocused dark-field images of “green” and “red” particles. Due to the spherical shape of nanoparticle, defocused images in both cases are symmetrically spread and show a ring-shaped pattern with a colored center, which indicates the contributions from both vertical and horizontal dipoles. However, a very strong green halo was only observed in “green” particles, whereas the “red” particles showed only a broad red halo. This proves the presence of the horizontal dipole for “green” particles and its absence in “red” particles. Therefore, by introducing a thin absorbing polymer spacer, first, the peaks were separated instead of resulting in a broad convoluted peak at 545 nm as was the case for the AuNPs directly on a metal film. Second, horizontal NP LSPRs were not observed for many particles, and, as a result, the NPs appeared red in the dark-field microscopy images. These red particles accounted for almost 68% of all of the particles for AuNP/P3HT(16 nm)/Au film(35 nm) samples. The simulated results in Figure 3.6d showed a peak at 580 nm (attributed to  $L_2$ ) and a shoulder at 535 nm (attributed to  $L_1$ ). The discrepancy between theory and experiment and the trends mentioned above were attributed to varying degrees of partial embedding of AuNPs into the polymer film which will be discussed in detail later.



**Figure 3.6.** Measured dark-field scattering spectra for a single AuNP on a P3HT thin-film with (a) 16 nm (b) 50 nm and (c) 65 nm thickness on a 35-nm-thick Au substrate. Left inset in (a) is a schematic of the system under investigation; rightmost insets in (a) show defocused dark-field images of “red” (left) and “green” (right) particles. Scale bar in rightmost insets of (a) is 2  $\mu\text{m}$ . For 16-nm- and 50-nm-thick P3HT, spectra representing AuNPs with different color under dark-field microscopy were shown (in (a) spectra 1 and 2 are from green AuNPs; spectra 3 and 4 are from red AuNPs). The grey dashed lines are the

corresponding spectra from a bare P3HT/Au film region. The pink dashed line in (b) is the normalized absorption spectrum obtained from 50-nm-thick P3HT on glass. (d) Simulated scattering spectra of AuNPs on P3HT, with P3HT thicknesses ( $t_s$ ) the same as those in (a)-(c). (e) and (f): Simulated scattering spectra for a single AuNP on a (e) 20 nm and (f) 50 nm P3HT thin-film with different depth of AuNP embedding ( $t_e$ ) in the P3HT film. Insets show representative electric field intensity profiles in x-polarized ( $|E_x|^2$ ) and z-polarized ( $|E_z|^2$ ) directions and a schematic for the embedded system is shown in the top right inset in (e). Scale bars in the insets are 100 nm. The left and right sets of electric field intensity profiles are at the wavelengths corresponding to (d) the  $L_1$  and  $L_4$  modes for 50-nm-thick P3HT; (e) the  $L_1$  and  $L_2$  modes for the 8 nm embedded case; (f) the  $L_1$  and  $L_3$  modes for the 20 nm embedded case, respectively.

	Green	Red
AuNP/glass	100.00%	0.00%
AuNP/Si	100.00%	0.00%
AuNP/Au film(35 nm)	90.90%	9.10%
AuNP/Au film(100 nm)	92.10%	7.90%
AuNP/PMMA(16 nm)/Au film(35 nm)	50.00%	50.00%
AuNP/PMMA(50 nm)/Au film(35 nm)	95.00%	5.00%

AuNP/P3HT(16 nm)/Au film(35 nm)	32.00%	68.00%
AuNP/P3HT(50 nm)/Au film(35 nm)	29.60%	70.40%
AuNP/P3HT(65 nm)/Au film(35 nm)	30.80%	69.20%

Table 3.1. The proportion of “red” and “green” particles in different sample sets. Data were taken over several random areas and, in total, over 50 NPs from each sample type were analyzed. To categorize the dominant scattering color of a NP, analysis was carried out and if the percentage of red color was over 50%, the particle was categorized as “red” regardless of the percentage of green and blue.

When the thickness of P3HT was increased to 50 nm, the proportion of red particles increased slightly to 70% (Supporting Information, Table 3.1). For green particles, the peak at ~520 nm was apparent which was again ascribed to horizontal image dipole coupling ( $L_1$ ). For red particles, this peak was quenched. The grey dashed line is the scattering spectrum taken from a region with only the P3HT/Au film, and shows a broadband feature above 600 nm. Compared with the extinction spectra of P3HT/glass (Figure 3.6b, pink dashed line), the extinction of P3HT was very weak above 660 nm which suggested that the populated SPP modes played a role in the scattering spectra above 600 nm. Since vertical image dipole coupling ( $L_2$ ) should be very weak at a spacer thickness of 50 nm, and SPP modes not only can propagate relatively easily on Au at this wavelength, but also exponentially decay over a distance higher than 100 nm in the

vertical direction.<sup>128</sup> So the peak at 643 nm was not attributed to image dipole coupling but likely stemmed from coupled LSPR-SPP modes of the Au film ( $L_3$  or  $L_4$ ).<sup>85</sup> Otherwise the long wavelength scattering peak should blue shift due to the weaker contribution from the vertical image dipole. The SPP continuum of the Au film is broadband in nature, and can overlap with the wavelength of this peak. Due to the sub-wavelength nature of the AuNP, a broad range of wavevectors is generated. Then it can be expected that the AuNP interacts with the whole continuum of SPP modes which can be supported by the Au film. However, at wavelengths below 550 nm, the strong interband transitions from low-lying bands to empty conduction bands in Au make the imaginary part of dielectric function of Au increase strongly. This significantly shortens the SPP propagation length of Au at these wavelengths. Using the surface plasmon dispersion equation<sup>128</sup> for a single metal-dielectric interface, the SPP propagation length is only 1.1  $\mu\text{m}$  at a wavelength of 540 nm. This value increases to over 6  $\mu\text{m}$  at 643 nm (dielectric constant obtained from Ref<sup>116</sup>). The long SPP propagation length leads to strong SPP coupling to the far field via the NP which facilitates the out-coupling of SPPs at 643 nm. The simulated scattering spectrum shown in Figure 3.6d agreed reasonably well with the experimental spectra - three peaks at 525 nm, 620 nm and 645 nm were apparent. Based on the electric field profiles shown in the insets of Figure 3.6d-f, the intensity of the z-component of the long-wavelength peaks was much stronger and better localized in the spacer than that of the peak at the shorter wavelength, which corroborates our peak assignment. The peak at 620 nm was assigned to horizontal LSPR-SPP coupling and the peak at 645 was assigned to vertical



LSPR-SPP coupling because the latter peak was only visible under p-polarized excitation while the former peak was apparent under both s- and p-polarized excitation (Figure 3.7).

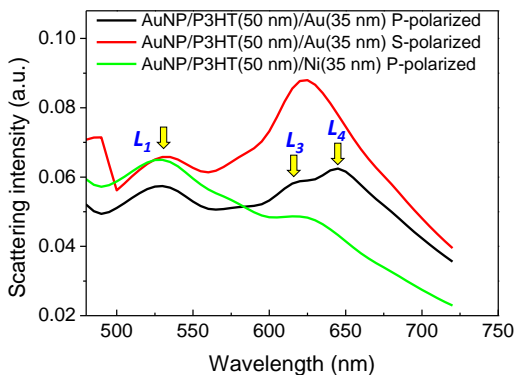


**Figure 3.7.** Simulated dark-field scattering spectra from an AuNP on P3HT (50 nm thick) on either a plasmonic (Au) or non-plasmonic (Ni) metal film under p- or s-polarized excitation.

For a 50-nm-thick P3HT spacer, the electric field intensity in the P3HT was mostly enhanced at the interface between AuNP and P3HT - reaching up to a factor of 40. Then the field decayed quickly further into the P3HT spacer and at the interface between P3HT and the Au substrate, the field intensity enhancement was only  $\sim 4$ . It is worth noting that compared with other work which studied similar “sphere-on-plane” systems, a commensurate level of field enhancement was not reached in our structure. This is due to the fact that unlike traditional gap mode studies<sup>120,129,123</sup> in which a sub-5-nm-thick gap was investigated, here we focus on a “gap” size between 15 nm and 65 nm, which is at the expense of extreme field localization. Also, due to the absorptive polymer we used, the high imaginary permittivity leads to dampened electric fields in the polymer region. Both

the decreased scattering cross-section and the dip from 550 nm to 630 nm were due to the larger optical density of the P3HT spacer as  $t_s$  increased. For the red particles, another peak occurred at  $\sim 580$  nm with  $t_s = 50$  nm. This peak was possibly due to the red shifted horizontal LSPR peak due to changes in effective refractive index of the surrounding medium. If the NP was partially embedded in the P3HT, a portion of the NP would interact with a medium with a high dielectric constant (P3HT), whereas the remaining portion would interact with air. Hence, the effective dielectric constant of the surrounding medium for a partially-embedded AuNP was expected to be higher than that of a NP that was not partially embedded. In fact, for 16-nm-thick P3HT, for the red particles there was also a small shoulder at similar wavelengths in certain cases (Figure 3.6a, spectra 3 and 4). The weak scattering intensity was probably due to both re-absorption by P3HT at that wavelength and a weaker scattering cross-section, which can be seen by comparing the absolute scattering peak intensity of a partially-embedded NP for a 20-nm-thick and 50-nm-thick P3HT spacer which are shown in Figure 3.6e and f, respectively. Compared with the scattering spectra of the 50-nm-thick PMMA spacer counterparts for which no peak was observed beyond 600 nm (Figure 3.3c), observation of the long wavelength peaks for the P3HT cases was probably due to both the fact that P3HT has a higher refractive index than PMMA at longer wavelengths (which improves wavevector matching to SPPs, resulting in a better LSPR-SPP coupling) and the physical interactions between AuNPs and P3HT. First, the AuNP used in our study had a mean diameter of 100 nm, which is relatively large in size and could be too heavy for a thin layer of polymer film to support.

The Young's modulus of P3HT thin-films is  $\sim 0.7$  GPa and this is relatively small compared with that of PMMA which ranges from 1.8 to 3.1 GPa.<sup>130</sup> This might allow the AuNP to partially sink into the P3HT spacer more so than for the PMMA case, which also explains why more "green" NPs were observed under dark-field when thicker P3HT spacers were replaced by PMMA. Second, the strong affinity between Au and thiophene groups could have induced a monolayer of P3HT surrounding the NP, thus the surface morphology of the P3HT film may have been altered to accommodate the curvature of AuNP, which could have further resulted in the partial embedding of NPs.<sup>131</sup> Since Au does not have a strong affinity for PMMA, this prevented AuNPs from sinking into the PMMA spacer. In addition, PVP-coated AuNPs have a negative Zeta potential on the surface (Nanocomposix, 100 nm PVP NanoXact Gold nanoparticles has Zeta potential of -30.7 mV), which would lead to positive charge accumulation when being deposited on P3HT and induces electrostatic interaction, whereas a similar phenomenon would not occur for a PMMA spacer due to its limited charge mobility. To prove similar spectral response would be achieved if the PMMA spacer could lead to partial embedding, simulations were conducted with a AuNP for various degrees of partial embedding in a 50-nm-thick PMMA spacer. The simulations showed that if the AuNP was partially embedded into PMMA, a decreased horizontal LSPR and red-shifted LSPR-SPP coupled modes would also occur (not shown).

After  $t_s$  was further increased to 65 nm, the majority of particles were green in color, which accounted for 68% of NPs. We could not successfully acquire spectra for the "red"

particles since most of them appeared very dark and the spectra suffered from significant noise. For the “green” particles, spectra are shown in Figure 3.6c. There was not a significant difference from the former situation with the P3HT spacer of 50 nm. The main difference was that the longer wavelength peak was slightly red shifted, due to weakened interaction between LSPR and SPPs arising from the larger distance between the AuNP and Au film, which is in agreement with previously reported studies.<sup>83</sup>

To further study the scattering properties of red particles, simulations were carried out for NPs partially embedded in P3HT with different thickness (Figure 3.6e,f). The simulated spectra had a strong resemblance to the experimental spectra shown in Figure 3.6a, b. With increasing extent of embedding: the LSPR peak, which was located at  $\sim 530$  nm, gradually decreased in intensity. This suppression of the  $L_1$  mode could be due to several reasons. First, as is stated before, the increased effective refractive index of the environment surrounding nanoparticles following partial embedding in P3HT (due to the greater interaction area) is expected to cause a red shift of  $L_1$ . In that case,  $L_1$  is either apparent as a red-shifted peak or it is convoluted with the  $L_2$  and/or  $L_3$  peak. Second, embedding will reduce the distance between the nanoparticle and metal film, therefore, for thinner spacers, image dipole coupling will increase. For  $L_1$ , in particular, stronger image dipole coupling is expected to cause a suppression of the mode due to the antiparallel image in the metal film (see Figure 3.2, top left). Furthermore, due to the greater contact area between P3HT and the nanoparticle and since the P3HT absorption spectrally overlaps with  $L_1$ , a greater

degree of  $L_1$  electric fields could be absorbed by P3HT. Similar to the experimental spectra from “red” NPs, the simulated spectra also showed only one peak above 600 nm, the FWHM of this peak was narrower with more embedding, indicating better field confinement. The increasing embedding depth resulted in decreased effective spacer thickness, which can be viewed as the distance between the bottom of the NP and the top of the metal film. Since the peak wavelength was red-shifted with increasing extent of embedding, this peak could be attributed mainly to the vertical dipole coupling mode ( $L_2$ ). The wavelength of  $L_2$  was red shifted by  $\sim 40$  nm compared with the  $L_2$  in Figure 3.6d, which was also likely due to the effective refractive index increase of the surrounding medium with NPs partially embedded in P3HT. This is consistent with the observed trend in the long wavelength peak in Figure 3.6a on going from green to red NPs. Also, the simulation showed that with greater extent of embedding, the intensity of the  $L_2$  mode was increased by over 50%. This indicated stronger field intensity confined in the polymer film when the NP was partially embedded. It should be noted even though  $L_2$  was the dominant mode with a spacer thickness below 20 nm, at the wavelength of  $\sim 620$  nm, LSPR-SPP coupled modes can also exist, which might contribute to the enhanced peak intensity. When the spacer thickness was increased to 50 nm, the electric field intensity of the z-component was much weaker compared to the 20-nm-spacer-thickness case (Figure 3.6e, insets), which was anticipated due to decreased interaction between the NP and metal film. Compared with the simulated spectra with a thin spacer, first, the extent of the red-shift of the long-wavelength peak with increased embedding was negligible for a 50-nm-thick

spacer. This further indicated that for a 50-nm-thick spacer, the long wavelength peak was attributed to a LSPR-SPP coupled mode, whereas for a thin spacer, LSPR-SPP modes were convoluted with the vertical LSPR. Second, the peak at 620 nm was also enhanced with increasing depth of embedding, which was due to better LSPR-SPP coupling. Since SPP fields exponentially decay in intensity away from the surface of the metal, with greater embedding and reduced distance between the NP and the metal film, the LSPR-SPP coupling is effectively improved. SPP fields can evanescently decay over a distance  $>100$  nm which makes it possible to couple. For the 50-nm-thick spacer the long wavelength peak was attributed to  $L_3$  based on its wavelength of 620 nm (Figure 3.6d), and with more of the NP embedded in the P3HT spacer, the vertical LSPR was expected to couple to the in-plane SPP mode better which would result in poor radiation into the far field.

To confirm the peak assignments, simulations were conducted to study the excitation of SPP modes in our system, as is shown in Figure 3.5. Besides the wavevector matching which has been overcome by introducing a thin polymer spacer on top of the metal film, the excitation of SPP modes still requires two conditions: a plasmonic metal such, as Ag or Au, and either p-polarized off-normal incidence excitation due to SPPs' out-of-plane polarized nature or near-field excitation *via* a nanoparticle. The simulations showed the  $L_1$  LSPR mode and the horizontal LSPR-SPP coupling mode ( $L_3$ ) in all conditions with a 50-nm-thick spacer, whereas only one spectrum had a peak at around 645 nm. This peak was not found in simulations using s-polarized excitation nor using a non-plasmonic metal film

(Ni), which supported the theory that this peak was related to excitation of a vertical LSPR-SPP coupling mode ( $L_4$ ).

To investigate the absorption enhancement in the spacer layer underneath the AuNP, simulations of the absorption within the P3HT spacer were conducted (Figure 3.8a, inset). Compared with the simulated results in the absence of AuNP, the integrated absorption inside reached enhancements greater than a factor over 4 (Figure 3.8a). However, as is indicated in Figure 3.8b, the enhancement factor dropped to 1.2 when  $t_s$  was increased to 50 nm. This was due to the exponentially decayed local NP electric fields with increasing spacer thickness. In other words, with thicker P3HT, the interaction volume of electric fields of the NP with P3HT would be less relative to the overall volume of P3HT. Therefore, this NP/absorber/metal film system is more effective for very thin absorbers. Additionally, for a thicker spacer ( $t_s = 50$  nm), the majority of the absorption enhancement occurred at the wavelength where  $L_4$  was prominent (Figure 3.8c), which suggested strong local field confinement caused by vertical LSPR-SPP coupling. Whereas for the thinner spacer ( $t_s = 20$  nm), the absorption enhancement reached maximum at 580 nm, which aligns well with the scattering spectrum shown in Figure 3.6d. This further proved that when the spacer was thin enough,  $L_2$  became the dominant mode at longer wavelengths and the stronger dipole-dipole interaction led to a substantial field enhancement in the spacer that dominated over the contribution from the LSPR-SPP interaction. However, in both cases, the contribution to absorption enhancement from  $L_1$

was limited, which agrees with the lack of significant spatial overlap between  $L_I$  electric fields and the spacer (Figure 3.6d, left insets).

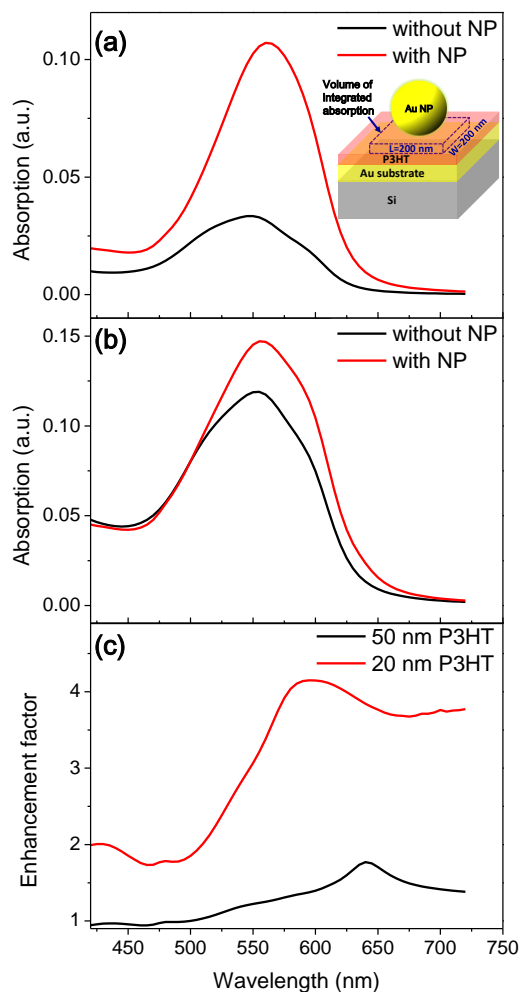


**Figure 3.8.** Theoretical absorption in the P3HT region from P3HT/Au film and AuNP/P3HT/Au film structures: (a) AuNP/P3HT (20 nm)/Au film (35 nm)/Si; (b) AuNP/P3HT (50 nm)/Au film (35 nm)/Si. Inset in (a) shows the configuration of the simulated structure: the box over which integrated absorption was calculated in the P3HT spacer was 200 nm in width, 200 nm in length and 20 nm in height. (c) Comparison of enhancement in absorption by P3HT for AuNP/P3HT/Au film structures relative to the P3HT/Au film case for a 20-nm-thick and a 50-nm-thick P3HT spacer.



### 3.5 Conclusion

We have studied the effect of underlying substrate and the thickness of an absorptive spacer layer on the spectral response of Au nanoparticles. Peaks in the measured single nanoparticle scattering spectra were attributed to four mode types: horizontal image dipole coupling at  $\sim 530$  nm, and, at longer wavelengths ranging from 580 - 650 nm, a vertical image dipole coupling mode and both horizontal and vertical LSPR-SPP coupling modes. By varying the thickness of either the absorptive spacer or the underlying metal film, the scattering peak at longer wavelength was tuned over a relatively wide range of wavelengths. Furthermore, the origin of the long wavelength peak stemmed primarily from vertical image dipole coupling for thinner spacers and was attributed to horizontal LSPR-SPP coupling for thicker spacers. Also, it was proposed that partial-embedding of the gold nanoparticle into the polythiophene spacer led to the appearance of most “red” particles for which the horizontal image dipole coupling mode was quenched and the longer wavelength peak was red-shifted. The spectral variations observed experimentally were reproduced in numerical electromagnetic simulations and corroborated the mode assignments. Strong field confinement at longer wavelengths in the absorptive polythiophene spacer was also detected in simulations due to the collective effect of vertical image dipole coupling mode and horizontal and vertical LSPR-SPP coupling mode. Simulations also showed that for the gold nanoparticle/polythiophene/gold film system absorption enhancement was greater for thinner spacers, with an absorption enhancement of greater than 4 in a 20-nm-thick

polythiophene spacer compared to the corresponding case without the nanoparticle. This demonstrated the promise of this system for enhancing the efficiency of ultra-thin, absorber-based optoelectronic devices. In summary, the work reported here is the first to identify and manipulate modes existing in a sub-50-nm thick absorptive conjugated polymer spacer sandwiched between plasmonic metal nanoparticles and a metal substrate. The results are a foundation for studies and applications of plasmonic structures for light management in optoelectronic devices with active layer thicknesses well below that used in more conventional devices.

## **Chapter 4. Detailed Optical and Physical Analysis of the Sphere-on-Plane System**

### **4.1 Introduction**

In Chapter 3, we comprehensively reviewed the effect of a thin absorptive spacer layer and underlying substrate material on the far-field spectral response of a single AuNP in a SOP system. The results show that there is strong electromagnetic coupling between the AuNP and underlying metal substrate when there is an ultra-thin absorptive spacer in between, which causes strong field enhancement, and, hence, absorption enhancement in the absorptive spacer layer. However, it still remains unknown whether the same coupling can lead to fluorescence enhancement from the spacer layer material, or if it is possible to selectively excite the different coupling modes and visually observe them at different wavelength scales. Furthermore, the effect of AuNP embedding on the spectral response of the SOP system could be confirmed by selective excitation of coupling modes and additional correlated optical and nanostructural characterization of the system.

This chapter consists of three separate sections: grazing-incidence defocused imaging, embedding investigations and single-particle DF/PL measurements of AuNP/polymer/Au SOP systems. The majority of the work in this chapter was carried out during a visit to the laboratory of Prof. Martin Vacha's at Tokyo Institute of Technology under the International Collaboration of Chemistry (ICC) program.

## **4.2 Methods**

### **4.2.1 Single Nanoparticle Defocused Dark-field Imaging**

Defocused dark-field images were recorded using an inverted microscope (Olympus, IX71) equipped with a high numerical aperture (N. A.) oil immersion objective (Olympus, x100, N.A. = 1.3). A white-light supercontinuum laser (Fianium model 0008) was used for excitation. A half-wave plate was introduced in the excitation path to rotate the polarization of the laser excitation. The incident angle of the laser on the sample was set to  $88^\circ$  with respect to the surface normal direction to create near grazing-incidence excitation for dark-field imaging and so that the polarization of incident light that excites the NP can be controlled (see Figure. 4.4a). The defocused dark-field images were acquired by moving the sample stage  $\sim 1 \mu\text{m}$  towards the objective (i.e., along the Z-axis direction) after a clear and sharp focused diffraction-limited dark-field scattering image was obtained. The scattering signal from the sample was collected by the same objective and detected using a single photon sensitive, electron-multiplying charge-coupled device (EMCCD) camera (Andor Technology, iXon).

#### **4.2.2 DF/PL Simultaneous Measurement**

Both DF and PL spectra were recorded using the same inverted microscope (Olympus, IX71) mentioned above with a high N. A. oil immersion objective (Olympus, x100, N.A. = 1.3), equipped with a single photon sensitive electron multiplying charge-coupled device (EMCCD) camera (Andor Technology, iXon) and a monochromator (Bunkou Keiki, CLP-50, 0.5 nm resolution). In this case, DF images and spectra were obtained in transmission mode and whereby a 100 W Halogen lamp, paired with a dark-field condenser was used

for excitation. For PL images and spectra, a 532 nm solid-state laser (TPG 532-500 Beamtech Optronics, Co. Ltd) was used for illumination at an epi-fluorescence configuration, in which the excitation laser were fed and the fluorescence signal were collected at the same side of the sample. The power output was usually less than 10 mW. In a typical run, SOP samples were coated with a layer of PVA (2 wt%, evenly drop-casted on top of the sample) and placed on the sample stage upside down, (i.e., with the AuNP side facing down). DF images and spectra were recorded first to locate single nanoparticles, then the halogen lamp was turned off and the solid-state laser was turned on, Subsequently, PL images and spectra were recorded for the same particle.

## 4.3 Results and Discussions

### 4.3.1 Grazing-incidence Defocused Imaging

To investigate the dipole moments of the scattering modes of the AuNP/spacer/Au film with controlled excitation polarization, grazing-incidence, broadband defocused dark-field imaging was conducted. A supercontinuum laser with coherent illumination spanning wavelengths of 300 nm to 800 nm was used for excitation (see Section 4.2.1). The incident angle was set to  $88^\circ$  in order to create near-grazing incidence, polarized illumination (Figure 4.1a). Figure 4.1 shows histogram of the out-of-plane angle,  $\psi$ , for single AuNPs in SOP systems with various polymer spacer materials and thicknesses under p-polarization. The angle of  $\psi$  was determined by comparison between the single particle

defocused images (shown beside the columns) and defocused PL images of single molecules reported in the literature (see Figure A3),<sup>132</sup> with  $90^\circ$  corresponding to a completely vertical orientation (i.e., parallel to the Z-axis) and  $0^\circ$  corresponding to a horizontal orientation (i.e., in the X-Y plane). The images were analyzed using radial line profiles and compared with the literature value.<sup>127</sup> Nanoparticles with scattering modes polarized vertically showed a ring-shaped defocused dark-field pattern, while nanoparticles with more in-plane (i.e., horizontally) polarized scattering exhibited more anisotropic or distorted defocused dark-field pattern. In general, when the thin PFO or MEHPPV was used as the spacer layer, most of the NPs exhibited a vertical dipole under p-polarized excitation (Figure 4.1b,e). However, more horizontal components were observed with a thicker spacer (Figure 4.1f). This was probably due to the fact that, with a thinner spacer, the coupling between the particle dipole and the image dipole in the underlying metal film was stronger in the out-of-plane direction (Z-direction). In contrast, the horizontal particle dipole excited using s-polarized light and the image dipole were expected to be antiparallel, resulting in a weaker net dipole moment. Accordingly, this led to a much stronger vertical dipole which was easily excited under p-polarized illumination. With a thicker spacer, the coupling between the particle dipole and its image dipole was weakened, which facilitated a stronger horizontal dipole and a weaker vertical dipole. As a result, the p-polarized component of the scattering dropped compared with that for the thinner spacer case. With regard to P3HT, at a thickness of 20 nm, the orientation of the scattering dipole was still primarily vertical which was similar to PFO. However, when the P3HT spacer thickness

was increased to 50 nm, not only did vertical component decrease, but also the horizontal component became dominant, which was not observed in the 50 nm-thick PFO case. This behavior was possibly due to the partial embedding of AuNPs into the P3HT spacer, which resulted in improved in-plane coupling to surface plasmon modes and greater absorption of the vertical dipole mode by the P3HT film.<sup>131</sup> Preliminary results indicate that for a 50 nm-thick spacer, LSPR-SPP coupling dominated compared with image dipole coupling and, with more of the NP embedded in the P3HT spacer, the vertical LSPR is expected to couple to the p-polarized SPP mode better which would result in poor radiation into the far field. Besides, with embedding, the dipole moment of the polymer could interfere with the particle dipole which would result in a more complex outcome.

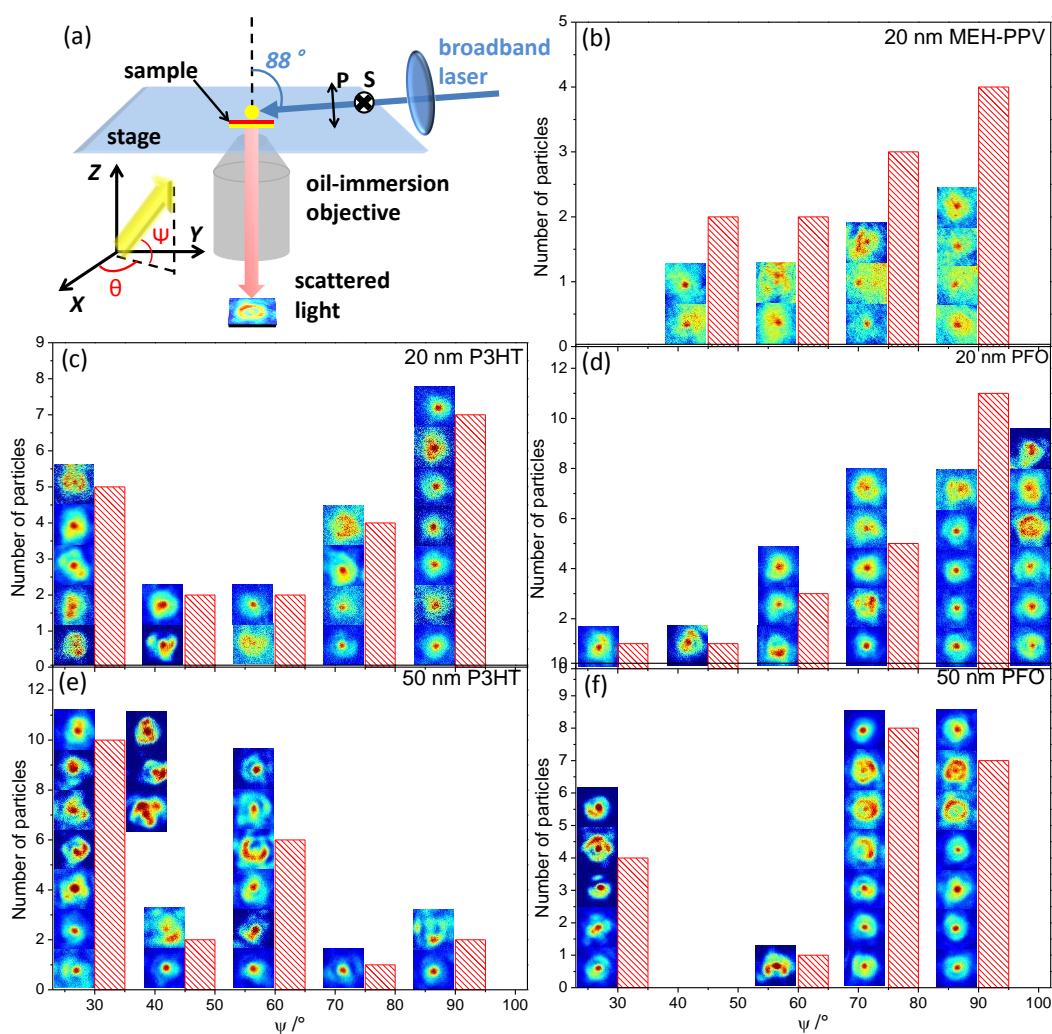


**Figure 4.1.** (a) Schematic diagram of the broadband defocused imaging setup. P-polarized illumination was employed to excite the vertical modes primarily.  $\Psi$  and  $\theta$  indicate out-of-plane and in-plane angles, respectively. Distribution of  $\Psi$  for AuNP/polymer spacer/Au film sphere on plane systems with various polymer spacers: (b) 20 nm-thick P3HT, (c) 20 nm-thick PFO, (d) 50 nm-thick P3HT, (e) 50 nm-thick PFO, (f) 20 nm-thick MEH-PPV. The spacers were all sandwiched between AuNPs of 100 nm diameter and a 35 nm-thick Au film. Representative defocused images are shown beside each column.



### 4.3.2 AuNP Embedding Investigation

In Chapter 3, it was proposed and theoretically confirmed that partial embedding of AuNPs into the P3HT thin-film spacer was the major contributor to the scattering peak at longer wavelengths for “red” particles. Furthermore, in Section 4.3.1 it was proposed that the dominant horizontal components in the defocused images of 50-nm-thick P3HT samples was also a result of partial nanoparticle embedding. To physically confirm the embedding of AuNPs, AFM measurements of the heights of AuNPs were conducted for a range of polymer spacer layers and, control measurements were conducted for AuNPs on glass substrates.

To relocate the individual AuNP and to correlate AFM height data with nanoparticle scattering color, regions of different samples were first labeled in DF images and the same regions of the sample were then scanned using AFM. Figure 4.2a-e shows the corresponding AFM topography scans and DF images of AuNPs on P3HT and PFO films (with thickness of 20 nm and 50 nm, in both cases) on 35-nm-thick Au films and of AuNPs directly on a glass substrate. Histograms of AuNP heights are shown in Figure 4.2f and the heights were extracted from AFM scans taken over several random areas. In total, over 80 AuNPs from each sample type were analyzed. The DF images reveal that a certain number of AuNPs were red/orange on both 20-nm and 50-nm-thick P3HT. In the histogram, it can be seen that compared to AuNPs/glass, the heights of NPs were decreased in both P3HT and PFO cases, The difference between P3HT and PFO lies in the distribution of the heights. In PFO cases, most NPs have the similar heights, whereas in P3HT cases, a portion of

AuNPs exhibited heights less than 80 nm which were significantly smaller than the peak value of the height distribution. This suggested that some AuNPs were partially embedded into the P3HT film to a relatively significant extent. Interestingly, most of these embedded NPs appeared red in the DF images, which proved the hypothesis of a direct correlation between NP color and the extent of embedding.

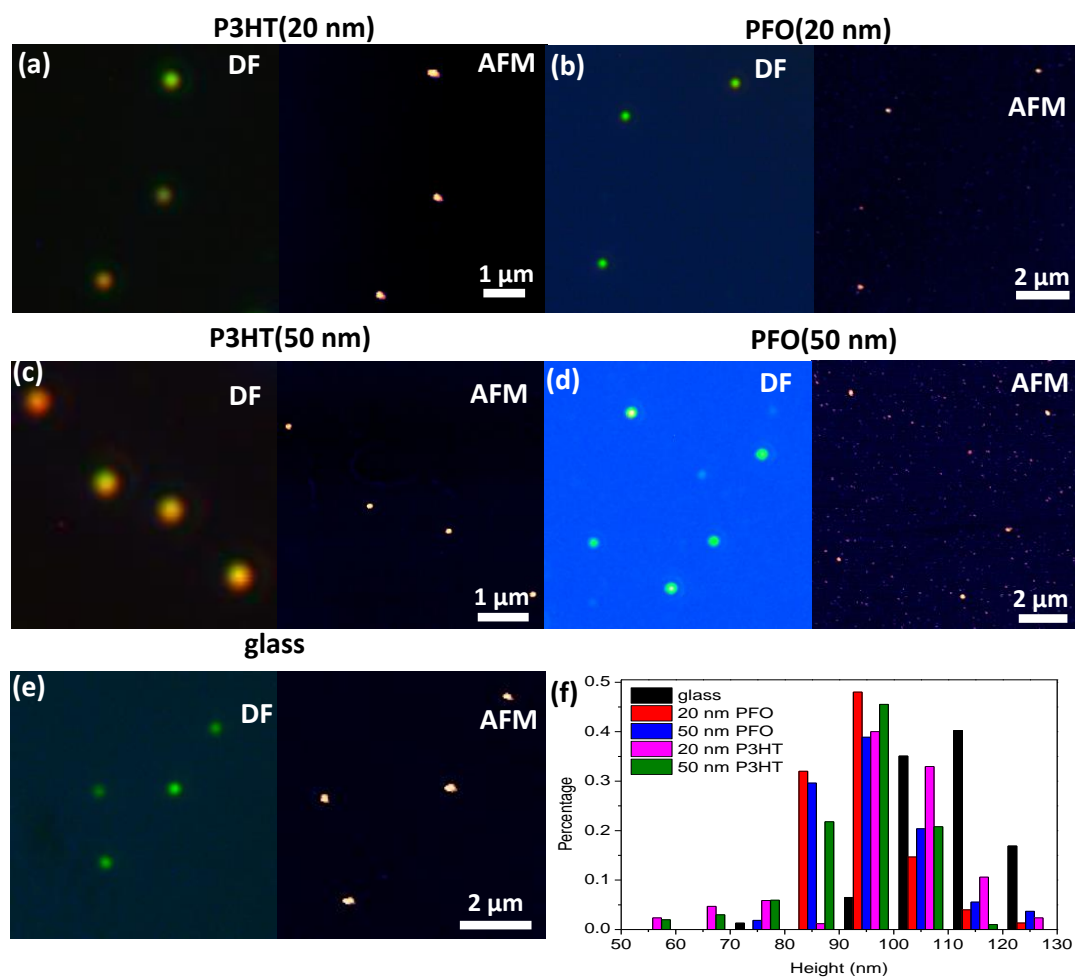


**Figure 4.2.** Dark-field images and AFM scans of the corresponding areas with 100 nm AuNP on: (a) 20 nm P3HT, (b) 20 nm PFO, (c) 50 nm P3HT, (d) 50 nm PFO on a 35-nm-thick Au film and (e) directly on glass. (f) represents the histogram of AuNP heights of different sample sets.

### 4.3.3 DF/PL Measurements

To investigate how the coupling modes at different wavelengths affect the fluorescence of different polymer spacers, three conjugated polymers were investigated: PFO, P3HT, MEHPPV. These three polymers have distinct emission spectra at different wavelength ranges, which is of interest for probing specific SOP coupling modes at different wavelengths. Results in Figure 4.3 show that for both P3HT and PFO, the AuNPs were not observed to have an effect on PL intensity in the PL images. This was due to the fact that for an AuNP to satisfy the spectral conditions for nanoplasmonic emission enhancement, the surface plasmon resonance band of the AuNPs need to overlap with the emission band of the fluorophore.<sup>133</sup> For MEHPPV, the  $S1 \rightarrow S0$  0-0 singlet exciton transition peaks at a wavelength of 585 nm which spectrally overlaps well with the surface plasmon resonance of a 100-nm-diameter AuNP which occurs at  $\sim 575$  nm. However, for either PFO or P3HT, the emission peaks (420-450 nm and 620-700 nm, respectively) have only minimal overlap with the expected surface plasmon resonance peak, which is expected to lead to poor fluorescence enhancement.

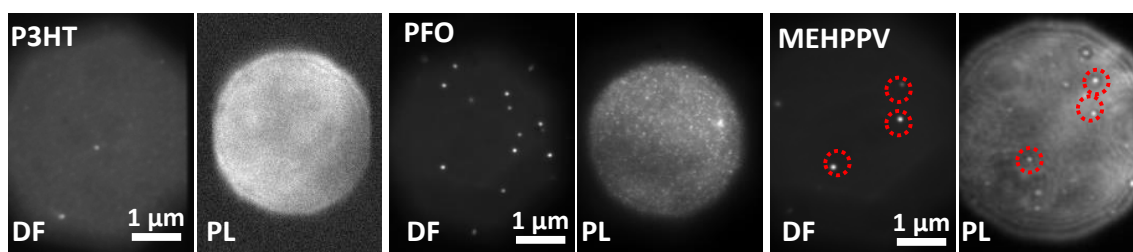


**Figure 4.3.** Comparison of DF and PL images of the same area for three different polymers: P3HT, PFO, MEHPPV in an SOP system. SOP samples are prepared using the same method described in Chapter 3,

section 3.3.1 and were constructed as follows: 100 nm AuNP/20-nm-thick polymer spacer/35 nm Au film/glass.

During the measurements, it was also observed that the enhanced fluorescence signal has strong directional dependence. In Figure 4.4, it is clear when the samples were normally placed (i.e., AuNP side facing up), the AuNPs which were observed in DF images were indistinguishable in the PL images. However, when the samples were placed upside down (i.e., AuNP side facing down), not only a good correspondence between DF and PL images were achieved, but also the PL signals were much stronger than that of a normally placed sample. This indicates that the excited surface plasmon resonance modes preferentially coupled to the molecular transition dipole in the backward direction. This directional-dependent behavior was probably due to either the re-absorption of P3HT fluorescence by the underlying Au film or the destructive coupling of SPP which diminished the signal.

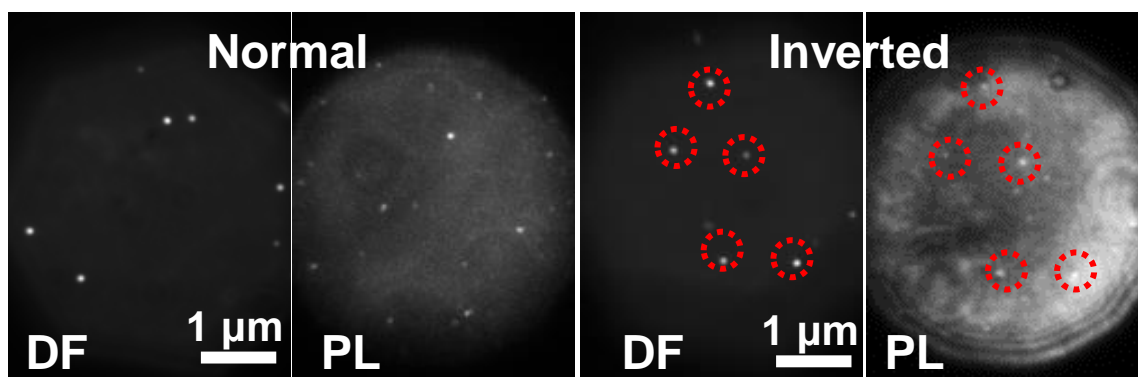


**Figure 4.4.** Comparison of DF and PL images for a normally-placed and an inverted 100 nm AuNP/20 nm MEHPPV/35 nm Au film sample.

Figure 4.5a shows an example of the difference of PL signals acquired from AuNP/MEHPPV spacer/Au film and MEHPPV spacer/Au film areas. We were able to observe stronger PL signals from regions of the sample where AuNPs were present (see figure 4.5, inset), which is an indication that the PL quenching induced by polymer directly contacting metal structure was overcome. As is shown in Figure 4.5b, the AuNP under study has a characteristic strong horizontal surface plasmon resonance peak at  $\sim 570$  nm and a weak vertical surface plasmon resonance peak at  $\sim 680$  nm. This result was in line with the time-resolved pump-probe measurements for the templated nanorod array samples with ultra-thin P3HT spacer in chapter 2, section 2.5, which also showed fluorescence enhancement under the influence of nanorod.

To investigate whether the PL enhancement was determined by the electromagnetic coupling modes in the SOP system, multiple statistical studies were conducted. Figure 4.6a shows the dependence of PL enhancement on the scattering enhancement at the AuNP area and Figure 4.6b shows the PL enhancement at the wavelengths of individual coupling modes. In both cases, the PL enhancement is sporadically located and not dependent on either the field enhancement factor or the wavelengths which have the strongest field. This indicates that the PL enhancement of MEHPPV was not directly correlated to the electromagnetic coupling modes between AuNP and underlying Au film in the SOP system.

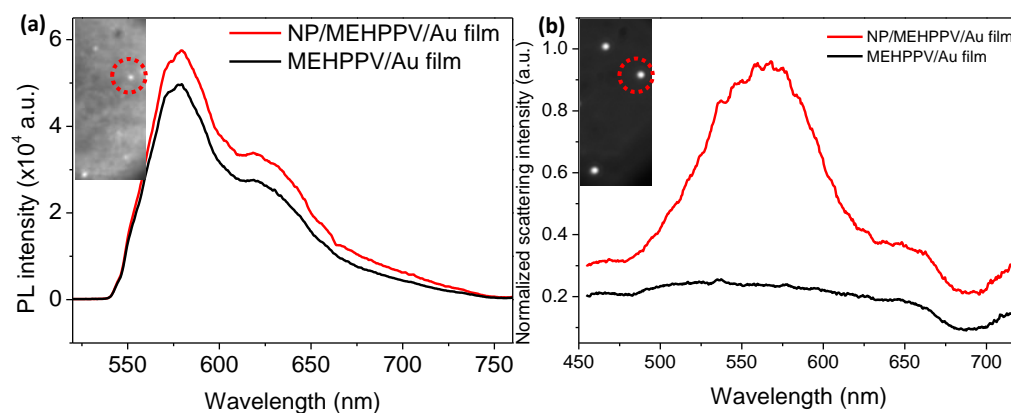


**Figure 4.5.** PL difference (a) and dark-field spectra (b) of the same AuNP. Left insets in both (a) and (b)

show the corresponding DF/PL images. Right inset in (a) shows the raw PL data from the AuNP/MEHPPV/Au film area (red) and the MEHPPV/Au film area (black). The PL difference was obtained by subtracting the PL signal taken from the no NP area from that taken from the NP area.

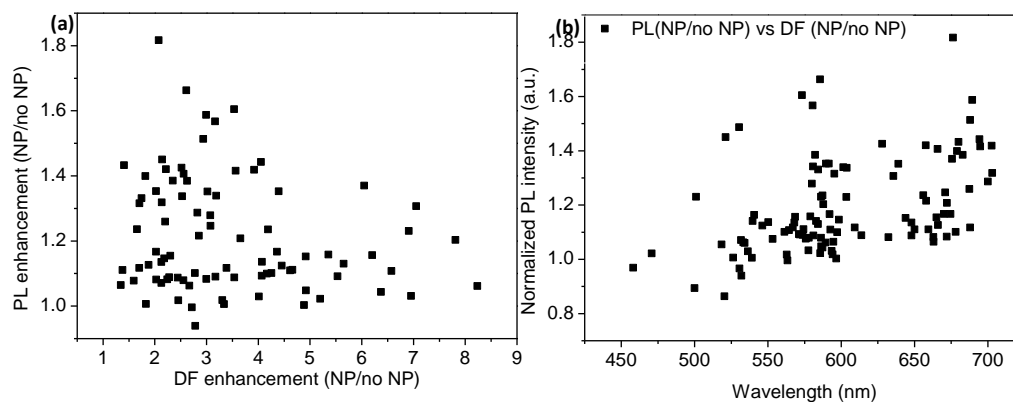


**Figure 4.6.** (a) PL enhancement (NP area divided by no-NP area) plotted against the DF enhancement

at the surface plasmon resonance peaks of DF spectra. (b) Normalized PL enhancement plotted against the surface plasmon resonance peak wavelengths.

#### **4.4 Conclusion.**

In conclusion, to further study the mode-specific physical and optical properties of the SOP system, grazing-incidence broadband defocused imaging, AFM study of NP heights and PL/DF simultaneous measurements were conducted. The AFM heights analysis proved that AuNPs were partially embedded in both PFO and P3HT cases. However, in P3HT there are particles that were deeply embedded which resulted in the red particles mentioned in Chapter 3 and the dominant horizontal component in the defocused imaging study. The further targeted single particle DF/PL study showed that the 100-nm-diameter AuNPs can only induce enhancement from MEHPPV thin-film as a result of the spectral overlap between the localized surface plasmon resonance band of the NPs and the emission band of the spacer. The results also revealed the highly directional characteristic of the fluorescence signal which was due to the preferential coupling between AuNP and underlying metal film. Future research includes the solvent vapor annealing (SVA) to investigate the influence of morphological and topological change of the polymer spacer on the embedding of AuNPs

## **Chapter 5. Effects of Nanoscale Morphology on the Optical Properties of Organic Semiconductor Thin-Film Ternary Blends**

### **5.1 Abstract**

Here, we investigate the efficiency of energy and charge transfer in blends of organic semiconductors with cascading bandgap energies. Unary, binary, and ternary solutions of the following organic semiconductors: poly(9,9-dioctylfluorenyl-2,7-diyl) (PFO), poly(3-hexylthiophene) (P3HT), and 2,3,9,10,16,17,23,24-octakis(octyloxy)-29H,31H-phthalocyanine (OctPc), were used to prepare sub-55 nm unary-phase and blended thin-films. Spectroscopic analysis shows absorption band full-width-at-half-maximum (FWHM) values increase from between 60 and 160 nm for the individual materials to greater than 450 nm for the composite thin-film ternary blend. Additionally, photoluminescence measurements show significant quenching of excitations on the wider band-gap semiconductors (donors) in the presence of a narrower band-gap semiconductor (acceptor). Resonant energy or charge transfer is observed with efficiencies between 90% and 100% for the various blends. Grazing incidence wide angle X-ray scattering data indicate that P3HT and OctPc exhibit the poorest blending. This correlates with the lowest donor photoluminescence quenching efficiency due to the extended separation of the P3HT chains from OctPc molecules, which is confirmed by pump-probe transient absorption spectra. However, all other blends, including the ternary blend, exhibit improved blending of the constituent materials which correlates to closer donor/acceptor molecular distances, and, thus energy/charge transfer efficiency approaching 100%. In that regard, it is notable



that addition of a relatively small fraction of PFO disrupts OctPc crystallinity and enables improved energy/charge transfer between P3HT and OctPc. This work was done in collaboration with Gary Cheung, Mengdi Liu, Zheng Gong, and Prof. Piotr Piotrowiak. In this chapter, the primary focus will be the transient absorption study along with selected steady-state spectra as that is the aspect of this project that I was primarily involved with.

## 5.2 Introduction

Bulk-heterojunction organic photovoltaics (BHJ-OPV) has been an area of active research because of the possibility for simplistic fabrication of flexible energy sources with low-toxicity constituents<sup>134</sup>. The active layer of a typical BHJ-OPV is comprised of a binary blend of an absorbing p-type electron donor and an n-type electron acceptor in an interconnecting matrix. Limited spectral overlap by typical organic molecular and polymer absorbers with the solar spectrum (absorption spectral bandwidth in the range 100-200 nm at visible wavelengths<sup>134-141</sup> has led to synthesis of new absorber materials<sup>142-146</sup> and to development of device architectures such as tandem<sup>146,147</sup> and ternary blend OPVs.<sup>134-137</sup> In a ternary system, either an additional electron donor or acceptor can be added into the binary blend<sup>135</sup>. Since poly(3-hexylthiophene-2,5-diyl) (P3HT) : (6,6)-phenyl-C61-butyric acid methyl ester (PCBM) is the most widely-studied, thin-film, binary-blend system, the majority of studies of ternary blends to date have incorporated a third material into this system.<sup>135</sup> Cascading lowest-unoccupied molecular orbital (LUMO) level energies in the blended active materials leads to a transfer of excitation energy typically from the higher bandgap material to the lower bandgap material *via* energy or electron transfer. In that way,

the spectral absorption band of blended organic thin-films is effectively broadened compared to single-phase (i.e., unary-phase) organic thin-films and can yield improved light harvesting across the solar spectrum.

Alternative p-type conjugated polymers to P3HT with non-overlapping bandgap energies have been studied in binary polymer:PCBM systems to increase solar spectrum overlap.<sup>138-140</sup> Application of such polymers in a ternary system leads to a broader overall absorption band and better atmospheric stability.<sup>135</sup> Poly(9,9-dioctylfluorene-co-benzothiadiazole) (F8BT) and poly(2,6-(4,4-bis-(2-ethylhexyl)-4H-cyclopenta(2,1-b;3,4-b')dithiophene)-alt-4,7(2,1,3-benzothiadiazole)) (PCPDTBT) are two p-type organic polymers that have shown potential as the third active material in ternary systems.<sup>138-140</sup> For example, it has been shown that the P3HT:PCBM:F8BT system with a weight ratio of 1.0:0.6:1.4 exhibited improved light-harvesting ability compared to a blend of P3HT:PCBM with a weight ratio of 1:2 and, as a result, power conversion efficiency (PCE) was increased from 1.38% to 1.94 %.<sup>138</sup> However, in that study the P3HT:PCBM:F8BT system still underperformed compared to a well-optimized P3HT:PCBM device (with weight ratio of 1:1, PCE was 3.16%). The P3HT:PCPDTBT:PCBM system, with weight ratio of 0.8:0.2:1, was reported to outperform the P3HT:PCBM 1:1 system in BHJ-OPV devices after a thermal annealing step (PCE of 2.8% and 2.5%, respectively).<sup>140</sup> The proposed mechanism for the performance improvement was a two-step charge transfer process: following excitation, electrons transferred from PCPDTBT to PCBM and,

subsequently, the remaining hole carriers on PCPDTBT transferred to P3HT prior to collection at the respective electrode.

Many conjugated small molecule absorbers have great potential as sensitizers in OPVs as many have absorption bands that occur in the UV and near-infrared range.<sup>141-150</sup> When incorporated into a ternary system, this allows for a broader absorption band compared to what can typically be achieved with conjugated polymer-based absorber blends. The main drawback is the solubility of many of these conjugated small molecules in organic solvents. Work by Sharma *et al.* and Choi *et al.* demonstrated that P3HT:PCBM devices incorporating solution processable molecules such as diketopyrrolopyrrole with a cyanovinylene-4-nitrophenyl unit (DPP-CN) or 9,18-(di-2-hexyldecyl)-2,11-dimethoxy-9,18-dihydrobenzo(5,6)-s-indaceno(1,2-b)indeno(2,1-h)carbazol-6,15-dione (HMBI) show improved PCE.<sup>141,142</sup> The P3HT:DPP-CN:PCBM ternary blend extended the absorption edge from 630 nm to 750 nm when compared to the binary blend and yielded an increased PCE from 3.23% to 4.70%.<sup>141</sup> Due to the cascading relative offsets of the highest-occupied molecular orbital (HOMO) and LUMO energy levels, charge transfer was the primary mechanism of electronic interaction proposed between the three materials in the P3HT:DPP-CN:PCBM system, similar to that of the aforementioned polymer blend cases. The HMBI:P3HT:PCBM system extended the blue edge of the absorption band of the binary blend from a wavelength of ~400 nm to below a wavelength of 350 nm and yielded an increase in PCE from 2.6% to 2.9%.<sup>142</sup> The HMBI:P3HT:PCBM system

exhibited a long-range, Förster resonance energy transfer (FRET) process from HMBI to P3HT and then a charge transfer process from P3HT to PCBM.

Other ternary blend systems employing small organic molecules have incorporated one or more phthalocyanine derivatives<sup>148-150</sup> to broaden the OPV active layer spectral absorption band and improve overall PCE compared to a binary blend active layer. Various energy or charge transfer mechanisms have been identified in these systems, such as exciton migration, short- and long-range excitonic energy transfer (i.e., Dexter and Förster transfer, respectively) and short-range electron and/or hole transfer.<sup>151</sup> The presence (or absence) of a particular mechanism typically depends on relative HOMO and LUMO energies, the relative ratios of the materials and whether the materials are p- or n-type. Changes in crystallinity and morphology of ternary-blend organic thin-films compared to binary-blend thin-films have also been reported and can impact the device favorably or unfavorably depending on the relative ratio, crystallinity and molecular organization of the constituent materials.<sup>152,153</sup>

While studies on ternary blend active layers containing fullerene derivatives have proven that they are capable of enhancing photovoltaic device performance due to increased solar light harvesting,<sup>135</sup> the potential increase could be extended further by more broadband harvesting of the solar spectrum. Here, a thin-film ternary blend system comprised of three complementary conjugated organic absorber materials is employed to generate a substantially broadened absorption spectrum, spanning more than 450 nm, and the extent and efficiency of both energy transfer (Förster and Dexter) and charge transfer

mechanisms in this blend are investigated. This study also investigates morphological properties of the organic semiconductor ternary blend thin-films compared to binary blends and the unary phase films.

### **5.3 Methods**

#### **5.3.1 Time-resolved Pump-probe Measurements**

Time-resolved measurements were acquired in the laboratory of Prof. Piotrowiak at Rutgers-Newark. The following describes the time-resolved pump-probe setup used there. The pulses of a commercial Ti:Sapphire oscillator (Spectra Physics, Tsunami) were amplified in a multi-pass, home-built Ti:Sapphire amplifier, which resulted in 0.4 mJ, 70 fs pulses at a wavelength of 790 nm with a repetition rate 1.25 kHz. The laser beam from the amplifier was split into probe and pump beams using a beam splitter. The pump beam (~25 fs, 3.5 mW, 370 nm) was produced by a non-collinear optical parametric amplifier (NOPA, Topas White plus Top SHG). The probe beam was delayed with the help of a computer-controlled motion controller and focused into a 2 mm sapphire plate to generate a white light continuum. The white light was spatially overlapped with the pump beam in the plane of the thin-film sample. In order to reduce sample heating effects, the thin-film was placed in a quartz cuvette filled with water. To measure the absorbance change, the signal was collected by a detector (Thorlabs, DET110) and monochromators (Driel MS257 with 1200 lines grating). The typical power of the pump beam was 200  $\mu$ W at the thin-film sample. The polarization of the pump beam was set at the magic angle (54.7°) relative to that of the probe beam to minimize polarization effects.

## 5.4 Results and Discussion

This work was done in collaboration with an undergraduate research assistant, Gary Cheung, who was responsible for the sample preparation and characterization such as AFM, Grazing-incident wide angle X-ray Scattering (GIWAX), steady-state photoluminescence and absorption spectroscopy. Selected data obtained by Gary Cheung is included here as it is necessary for interpretation of the transient absorption results. My contribution involved the acquisition of the ultrafast transient absorption spectra in the lab of our collaborator Prof. Piotrowiak and analysis and interpretation of the resulting data.

### 5.4.1 Structure and Energy Diagram of Organic Semiconductors

The chemical structures of the three organic semiconductors employed in this study and an electronic energy level diagram are displayed in Figure 5.1a-d.<sup>154,155</sup> All of the materials were soluble in chloroform and were cast into unary, binary or ternary blend thin-films with thicknesses ranging from ~5 – 55 nm. The concentrations of the organic semiconductors in solutions containing one or more of the semiconductors were fixed at 2 g L<sup>-1</sup>, 5 g L<sup>-1</sup> and 10 g L<sup>-1</sup> for PFO, P3HT and OctPc, respectively. As a result, the binary and ternary thin-films that were cast from blended solutions exhibited thicknesses that corresponded well to the summation of the unary phase thin-film thicknesses of the corresponding materials. For example, film thicknesses of 4.9 nm, 14.5 nm, and 32.0 nm

were measured for the single phase PFO, P3HT and OctPc films, respectively, and the ternary blend film was found to have a film thickness value of 54.1 nm which corresponded well with to the sum of the respective unary-phase films.

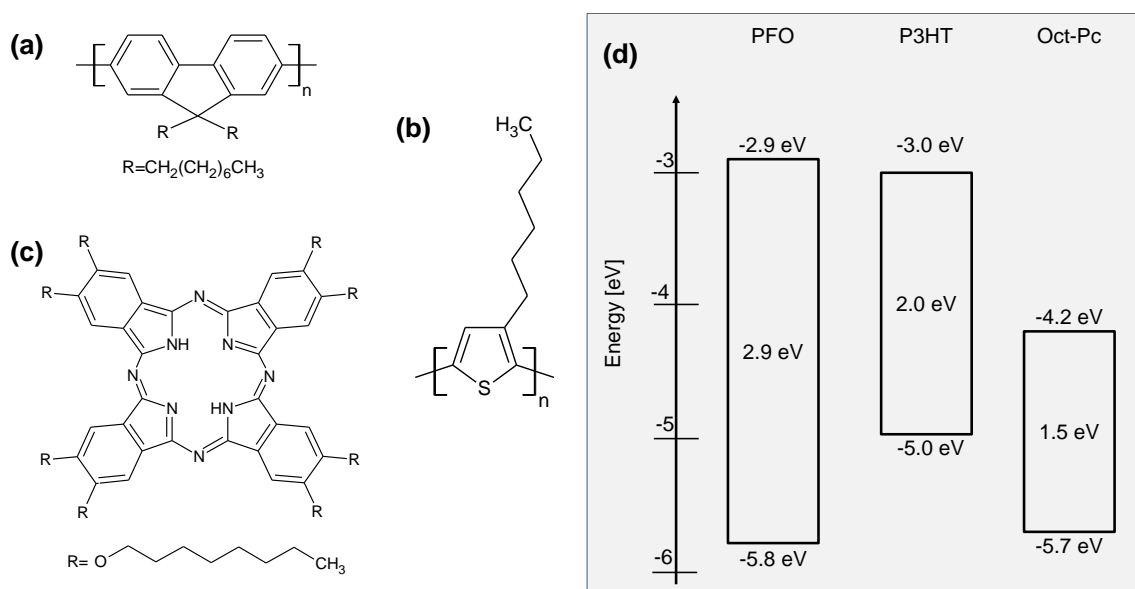
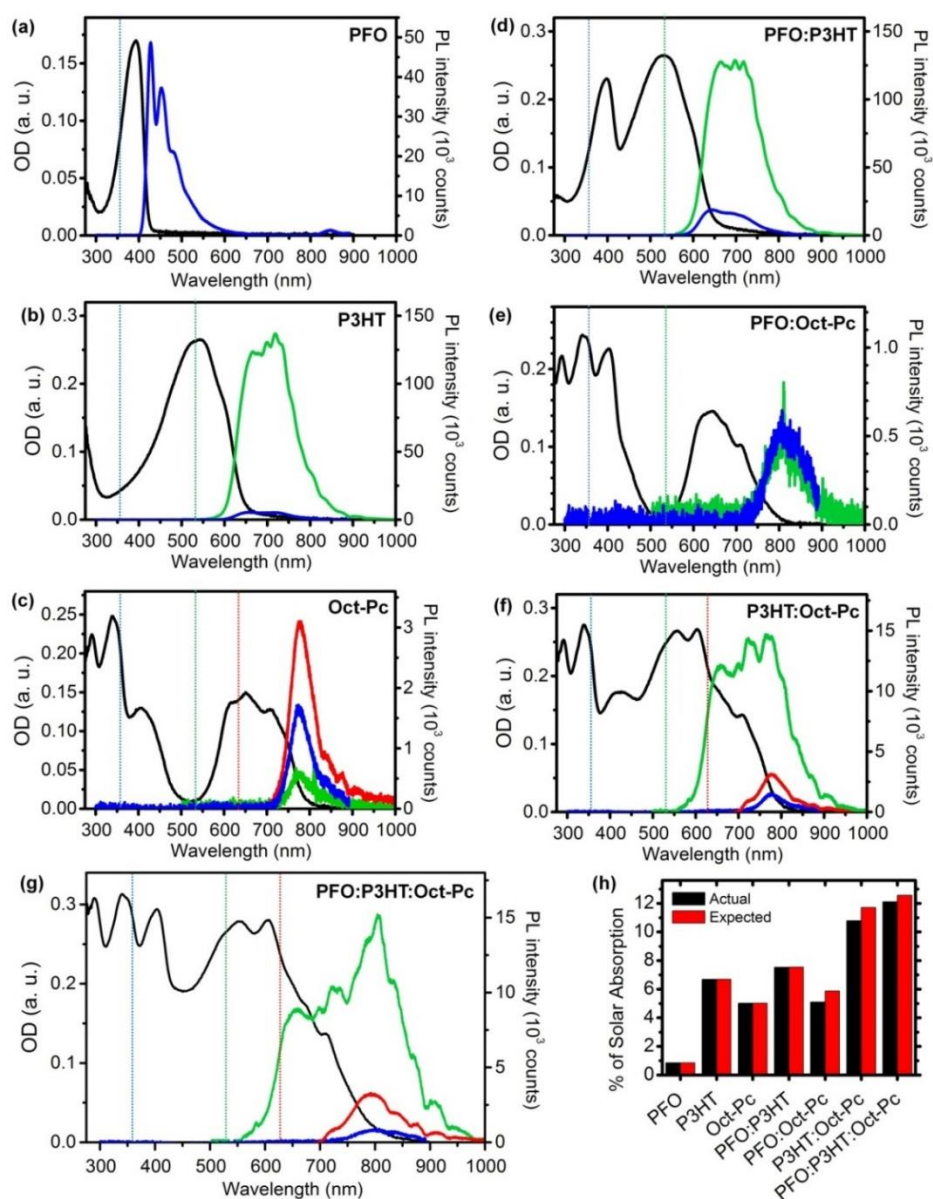


Figure 5.1 Chemical structures of (a) PFO, (b) P3HT, and (c) OctPc.(d) Energy level diagram of the three organic semiconductors shown in (a)-(c) with approximate HOMO, LUMO and band-gap energies shown.<sup>141-153</sup>

### 5.4.2 Steady-state Optical Properties

Figure 5.2a-g show the absorption and PL spectra of the unary, binary and ternary thin-films. The absorption maxima of the unary phase materials occurred at wavelengths of 393 nm and 544 nm for PFO and P3HT, respectively. OctPc exhibited two strong absorption bands centered at 340 nm and 651 nm. Additionally, there was minimal spectral overlap of the dominant absorption peaks of each material. The full-width-at-half-maximum (FWHM)

values of the lowest energy band of the absorption spectra for the single phase films were 55 nm, 162 nm and 167 nm for PFO, P3HT and OctPc, respectively. The binary and ternary blend absorption spectra were almost direct summations of the individual absorption spectra of the constituent materials. This led to strong absorption spanning the near-UV and visible wavelength range, particularly for the ternary blend which exhibited a FWHM of more than 450 nm (Figure. 5.2g).





**Figure 5.2.** Optical density, OD, (i.e., absorbance) and PL spectra of: (a-c) single-component; (d-f) binary blend; and (g) ternary blend thin-films with concentration of 2, 5 and 10 mg/mL for PFO, P3HT and OctPc, respectively. Dotted lines represent the laser excitation wavelength, solid black lines represent extinction spectra and solid colored lines represent PL spectra. (h) Bar chart of percentage solar absorption (relative to the AM1.5 solar spectrum) for the single component, binary blend and ternary blend thin-films. Both actual (black; determined from extinction spectra of all film types) and expected (red; determined from a summation of the individual single-phase extinction spectra) solar absorption percentages are shown. Steady-state spectra were acquired by Gary Cheung.

The PL spectra (acquired following excitation of the primary absorption transition of each material) of the single phase thin-films exhibited  $S_1-S_0$  0-0 singlet exciton transitions at 430 nm, 666 nm and 776 nm for PFO, P3HT and OctPc and characteristic vibronic structure at longer wavelengths (Figure. 5.2a-c). The binary blends should exhibit emission from the lower bandgap acceptor material and notable quenching of emission from the donor material if significant charge/energy transfer occurs.

This was apparent for the PFO:P3HT and PFO:OctPc binary blends (Figure 5.2,e) when an excitation wavelength of 355 nm was employed. For both of these binary blends, PFO's characteristic emission spectrum was completely quenched and only emission from P3HT or OctPc was observed. This was expected for the PFO:P3HT blend due to the significant spectral overlap of the PFO emission and the P3HT absorption band. For the PFO:OctPc blend, the significant PFO emission quenching suggested that the OctPc

molecules and the PFO chains were in very close proximity to each other since the two materials have little spectral overlap between absorption and emission spectra. In this work, donor-acceptor distances less than  $\sim 1$  nm are possible since the acceptors are present in higher concentrations than the donor molecules and the blends are in the solid state which favors intermolecular interactions. Additionally, due to the large conjugation lengths of PFO and P3HT, their excitons are relatively delocalized and can undergo rapid exciton migration or transfer to neighboring molecules.<sup>156,157</sup> Therefore, in the blended systems studied here short-range Dexter energy transfer and charge transfer can contribute to fluorescence quenching in addition to long-range Förster resonance energy transfer.

In contrast to the PFO:P3HT and PFO:OctPc binary blends, the PL spectrum from the P3HT:OctPc binary blend exhibited residual P3HT emission in addition to emission from OctPc when the donor (i.e., P3HT) was directly excited at a wavelength of 532 nm (Figure. 5.3f). This incomplete quenching of P3HT's emission indicated that not all of the excitons generated in P3HT were transferred to OctPc. The donor fluorescence quenching efficiency,  $E_T$ , in each blend due to either energy or electron transfer was estimated from the fluorescence intensity of the donor as follows:<sup>158</sup>

$$E_T = 1 - \frac{F_{DA}}{F_D} \quad (5.1)$$

where  $F_{DA}$  is the fluorescence intensity of the donor in the presence of an acceptor and  $F_D$  is the fluorescence intensity of the donor in the absence of an acceptor.  $E_T$  for the blends studied in this work are shown in Table 5.1 along with the likely quenching mechanism(s).

Thin-Film Material Composition	$E_T$ (%)	Proposed Mechanism
PFO:P3HT	99.9	ET
P3HT:OctPc	90.8	ET/CT
PFO:OctPc	99.9	CT
PFO:P3HT:OctPc	99.9	ET/CT

Table 5.1. Donor fluorescence quenching efficiency values generated for each binary and ternary thin-film blend system calculated using Equation 5.1, along with proposed energy/charge transfer mechanism.

Highly efficient fluorescence quenching ( $E_T = 99.9\%$ ; indicating rapid energy/electron transfer) was apparent for all blends with the exception of the P3HT:OctPc binary blend ( $E_T = 90.8\%$ ). However, a relatively small fraction of PFO added to the P3HT:OctPc blend improved the energy transfer efficiency between P3HT to OctPc. Compared to the P3HT:OctPc binary blend, when P3HT was directly excited in the ternary blend, substantially weaker emission from P3HT was observed in the ternary blend PL spectrum (Figure. 5.3f and 5.3g). This may be due to the disruption of the OctPc crystallinity caused by PFO chains which in turn allows P3HT molecules to infiltrate OctPc molecules. Therefore, even though PFO does not significantly broaden the absorption band of the ternary blend, it appears to play an important role in minimizing phase separation in the ternary blend and ensures more effective energy/electron transfer to the OctPc.

### 5.4.3 Transient Absorption Measurements

Time-resolved pump-probe experiments were performed in order to directly examine the excited state dynamics in the composite films and more specifically to ascertain whether the different energy transfer yields in the P3HT:OctPc binary (~90%) and PFO:P3HT:OctPc ternary (>99.9%) blends determined on the basis of the steady-state fluorescence quenching measurements corresponded to homogeneous (which indicates all the molecules in all the domains decay through the same mechanism) or inhomogeneous (which indicates molecules from different domains undergo different decay pathways) energy transfer processes. We were able to conclude that the relatively large residual P3HT fluorescence observed in the case of the binary blend was the result of a pronounced inhomogeneity of the transfer process between P3HT and OctPc rather than a slower homogeneous rate. Most informative in this regard were the kinetic traces collected for pump and probe wavelengths of 530 nm and 700 nm, respectively (Figure 5.3a). At the probe wavelength the excited state of P3HT gave rise to strong absorption because the extinction coefficient of the excited state of P3HT\* was higher than that of the ground state, while OctPc gave a characteristic bleach (a negative  $\Delta OD$  signal) because the extinction coefficient of OctPc\* was lower than that of the ground state. In the OctPc sample the bleach at 700 nm associated with the formation of OctPc\* appears instantaneously within the time resolution of the measurement (~100 fs). This is the expected behavior since in these samples OctPc is the only ground state species capable of absorbing the excitation light at 530 nm. In the P3HT:OctPc and ternary blend films, the dominant light absorbing material is P3HT. As a result, in these samples the initial absorption signal at  $t = 0$  is

dominated by the excited state of P3HT and positive; however, it rapidly evolves into a bleach, consistent with a fast  $\text{P3HT}^* + \text{OctPc} \rightarrow \text{P3HT} + \text{OctPC}^*$  electronic energy transfer process (Figure 5.3b).

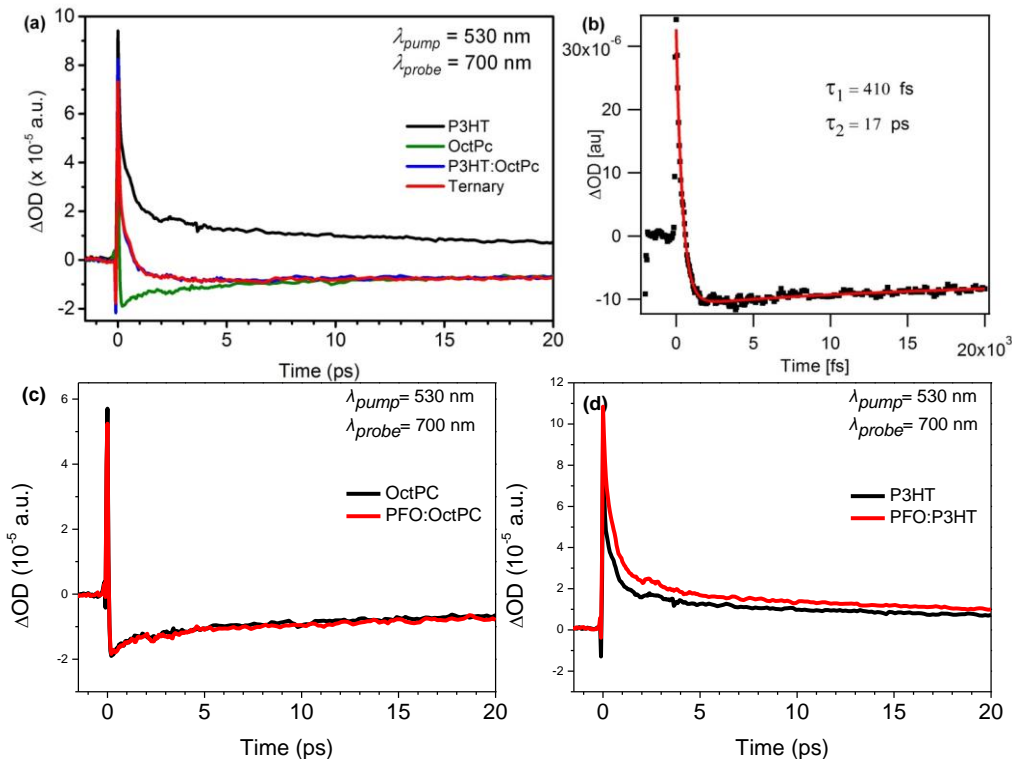


**Figure 5.3.** (a) Transient absorption curves for selected single phase blends, the three binary blends and the ternary blend for a pump wavelength ( $\lambda_{pump}$ ) of 530 nm and a probe wavelength ( $\lambda_{probe}$ ) of 700 nm. (b) Transient absorption profile (black symbols) with a double exponential fit (solid red line) recorded for the ternary blend at 700 nm. The rapidly evolving bleach,  $\tau_1 = 410$  fs, is the signature of the  $\text{P3HT} \rightarrow \text{OctPc}$  energy transfer. The much slower,  $\tau_2 = 17$  ps component corresponds to subsequent relaxation and recombination processes. A pump wavelength of 530 nm was employed for all transient absorption curves. (c) and (d) Transient absorption curves for OctPC and PFO:OctPC, P3HT and PFO:P3HT binary blend for a pump wavelength ( $\lambda_{pump}$ ) of 530 nm and a probe wavelength ( $\lambda_{probe}$ ) of 700 nm, respectively.

2<sup>nd</sup> order decay equation:  $y = y_0 + A_1 \times \exp\left(-\frac{x-x_0}{\tau_1}\right) + A_2 \times \exp\left(-\frac{x-x_0}{\tau_2}\right)$

	A <sub>1</sub>	$\tau_1$ (fs)	A <sub>2</sub>	$\tau_2$ (fs)	R-Square
P3HT	5.38032E-5	473.46822	1.28509E-5	6743.06133	0.99241
P3HT:OctPc	1.44394E-5	477.88924	4.00922E-10	36.86279	0.98556
Ternary	1.90389E-5	466.55116	1.90389E-5	466.55064	0.98571

Table 5.2. The second order exponential decay fitting equation of P3HT, P3HT:OctPc binary and ternary blend films.  $\tau_1$  represents the fast component and  $\tau_2$  represents the slow component.  $A_1$  and  $A_2$  correspond to the amplitude of fast/slow component, respectively. R-square value is the coefficient of determination which indicates how close the data are to the fitted regression line.

For comparison with the steady-state fluorescence results,  $E_T$  was estimated from the energy/charge transfer rates as follows:

$$E_T = \frac{k_{DA}}{k_D + k_{DA}} \quad (5.2)$$

where  $k_{DA}$  is the rate of energy or charge transfer between the donor and acceptor molecules and  $k_D$  is the donor exciton decay rate. The apparent energy transfer rates extracted from fitting are very similar for the binary and ternary blends, with the characteristic time constants,  $\tau_1$ , of 410 fs and 490 fs, (see Table 5.2 respectively ( $\pm 5\%$  error)). Assuming  $k_{DA} = 1/\tau_1$ , the  $2.4 \times 10^{12} \text{ s}^{-1}$  energy transfer rate in the ternary blend

combined with the  $\sim 400$  ps exciton lifetime<sup>159,160</sup> reported for neat P3HT agrees remarkably well with the  $\sim 99.9\%$  quenching efficiency determined from the steady-state fluorescence measurements for these films, thus strongly suggesting that in the ternary blend the energy transfer process is largely homogeneous. On the other hand, the  $2.4 \times 10^{12} \text{ s}^{-1}$  energy transfer rate measured for the binary P3HT:OctPc film should also lead to  $>99\%$  quenching and is not consistent with the residual  $\sim 10\%$  photoluminescence observed in the steady-state fluorescence measurements (i.e.,  $E_T$  from steady-state PL measurements was  $90.8\%$ ; see Table 5.2), which, using Equation 5.2, would be expected to correspond to a much slower  $\sim 2.47 \times 10^{10} \text{ s}^{-1}$  homogeneous transfer rate. The evident discrepancy between the time-resolved and steady-state measurements leads to the conclusion that electronic energy transfer in the binary P3HT:OctPc blend is highly inhomogeneous and indicative of underlying structural heterogeneity. The majority of the P3HT\* population in the binary blend transfers energy to OctPc very efficiently and nearly as rapidly as in the ternary system. This fraction dominates the observed pump-probe transients and gives rise to the 490 fs time constant. It is inferred that a smaller population of P3HT\* ( $\sim 10\%$ ) undergoes much slower energy transfer, with rates which span a broad range from a few picoseconds to hundreds of picoseconds. This weakly quenched population is likely responsible for the residual photoluminescence of the binary P3HT:OctPc films. From the structural point of view this strongly suggests that the P3HT:OctPc blend contains isolated pockets of pure P3HT which does not electronically couple with the OctPc acceptor sites sufficiently well to ensure complete energy transfer. This is consistent with the morphological results done

by Gary Cheung for the P3HT:OctPc blend which indicated the presence of distinct OctPc crystalline domains in the binary blend. Slow energy transfer components are not detected in the femtosecond pump-probe experiments, because they are obscured by the intrinsic decay dynamics of P3HT\* and OctPC\* which occurs at the same time scale. As expected, the decay mechanism of PFO:OctPC blend is exactly the same as the neat OctPC (Figure 5.3c) since there is no direct energy transfer between PFO and OctPC due to the significant difference in energy level. In PFO:OctPC blend, the neat P3HT undergoes a slightly different excited state decay process, however, a new decay mechanism was not observed. This is another proof that the addition of PFO modifies the crystalline domain of P3HT (Figure 5.3d).

To screen the influence from ground state bleaching from OctPC, time-resolved measurements were probed at 750 nm with the same excitation wavelength of 530 nm, the results of which is shown in Figure 5.4a. Compared with the decay dynamics obtained at 700 nm, P3HT still maintains a characteristic 2<sup>nd</sup> order decay while the decay mechanism was greatly changed for both the binary and ternary blends. The negative  $\Delta OD$  observed in the dynamics probed at 700 nm which was ascribed to ground state bleaching was not present here. The fact that the P3HT:OctPC binary blend decays faster than P3HT indicates that the energy/electron transfer between P3HT and OctPC can still be observed at 750 nm, and the transient absorption spectra shown in Figure 5.4b proves that the energy/electron transfer happened between 0.1 ps to 2 ps. It is noteworthy that the ternary blend has a long lived species compared with P3HT:OctPC binary blend, which is possibly due to the bound



exciton in OctPc. As is indicated in Section 5.4.1, PFO improves the molecular blending between P3HT and OctPc, meanwhile, disrupt the crystal structure of OctPc. The amorphous OctPc has less intermolecular interactions and, thus, more localized exciton was present.

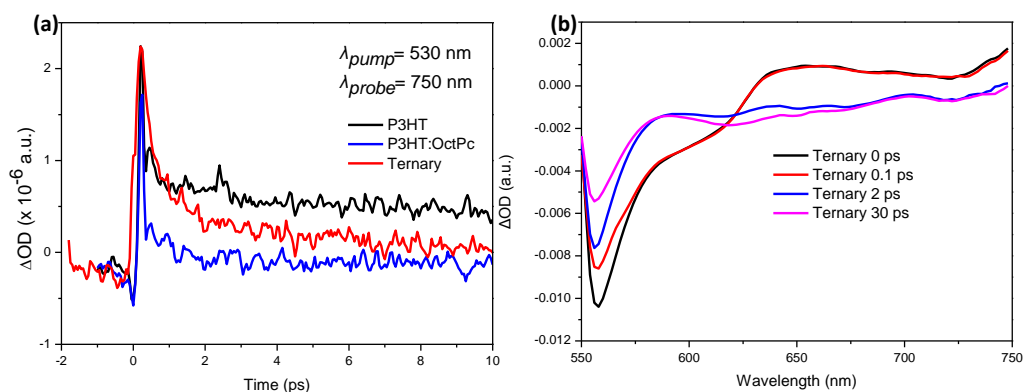


**Figure 5.4.** (a) Transient absorption curves for P3HT unary, P3HT:OctPc binary and the ternary blend for a pump wavelength ( $\lambda_{pump}$ ) of 530 nm and a probe wavelength ( $\lambda_{probe}$ ) of 750 nm. (b) Transient decay spectra for ternary blend at various time scale.

## 5.5 Conclusions

The ternary blend system reported here has the potential to enable an alternative to the stacked tandem organic photovoltaic device configuration with respect to overcoming the inherently narrow absorption bands of organic photovoltaic absorber materials. The thin-film ternary blend exhibited broadband absorption ( $> 450$  nm) and  $>90\%$  efficient energy/charge transfer between the components within the blend. While polythiophene and the phthalocyanine derivative exhibited strongly overlapping emission and absorption

bands, respectively, they exhibited relatively poor mixing. This resulted in inhomogeneous energy transfer between the two materials in the blended films with a rapid direct energy transfer in  $\sim 410$  fs and in addition to a much slower decay time of 17 ps. However, introduction of a relatively small fraction ( $\sim 10\%$  by volume) of polyfluorene improved mixing of the materials in the ternary blend and resulted in an increase in the efficiency of charge/electron transfer between polythiophene and the phthalocyanine derivative.

## **Chapter 6. Conclusions and Future Directions**

In Chapter 2, an experimental and theoretical study of the absorption changes and plasmonic modes arising from the placement of vertically-oriented gold nanorod arrays on sub-50-nm thick polythiophene films on silver substrates were presented. Vertical gold nanorod (AuNR) arrays were deposited on ultrathin polythiophene films using a large-area, lithography-free fabrication method. Both extinction and absorption characterization showed notable enhancement and broadening of the sample absorption spectra relative to undercoated polythiophene films on Ag substrates. 3D numerical simulations indicated different modes of the system affected sample absorption to different degrees whereas only gap mode wavelengths were both within the absorption band range of polythiophene and resulted in intense localized fields in the polythiophene layer directly underneath the nanorod, which made it the major contributor to the absorption enhancement in the active layer. In a follow-on study, time-resolved measurements confirmed that the fluorescence of P3HT had been enhanced with the presence of the AuNR array and had the same wavelength dependence as absorption/extinction enhancement. This work identified conditions for light-management in ultra-thin semiconductor films embedded in a monopole nanoantenna system. Such systems are applicable to ultra-thin optoelectronic devices where control of light interactions and mode coupling in the active layer are critical to device performance.

To gain an in-depth knowledge of the gap modes, in Chapter 3, we studied the effect of underlying substrate and the thickness of an absorptive spacer layer on the spectral

response in a sphere-on-plane (SOP) system. Four electromagnetic modes were detected in single nanoparticle scattering spectra and theoretically verified in 3D numerical simulations: horizontal image dipole coupling at  $\sim 530$  nm, and, at longer wavelengths ranging from 580 - 650 nm, a vertical image dipole coupling mode and both horizontal and vertical LSPR-SPP coupling modes. By varying the thickness of either the absorptive spacer or the underlying metal film, the scattering peak at longer wavelength was tuned over a relatively wide range of wavelengths. Strong field confinement at longer wavelengths in the absorptive polythiophene spacer was also detected in simulations due to the collective effect of vertical image dipole coupling mode and horizontal and vertical LSPR-SPP coupling mode. Simulations also showed that for the gold nanoparticle/polythiophene/gold film system absorption enhancement was greater for thinner spacers, with an absorption enhancement of greater than 4 in a 20-nm-thick polythiophene spacer compared to the corresponding case without the nanoparticle. The work reported here is the first to identify and manipulate modes existing in a sub-50-nm thick absorptive conjugated polymer spacer sandwiched between plasmonic metal nanoparticles and a metal substrate. The results are a foundation for studies and applications of plasmonic structures for light management in optoelectronic devices with active layer thicknesses well below that used in more conventional devices.

To investigate the effect of AuNP-induced coupling modes on the light out-coupling properties of the conjugated polymer thin-film, PL/DF simultaneous measurements were

conducted. The targeted single particle DF/PL study showed that the 100-nm-diameter AuNPs can only induce enhancement from MEHPPV thin-films as a result of the spectral overlap between the localized surface plasmon resonance band of the NPs and the emission band of the spacer. The results also revealed the highly directional characteristic of the fluorescence signal which was due to the preferential coupling between AuNP and underlying metal film.

Also, in the former studies, it was proposed that partial-embedding of the gold nanoparticle into the polythiophene spacer led to the appearance of most “red” particles for which the horizontal image dipole coupling mode was quenched and the longer wavelength peak was red-shifted. To fully understand this, an AFM height analysis proved that AuNPs were partially embedded in both PFO and P3HT cases. However, in P3HT there were particles that were more deeply embedded and which had plasmonic modes that were likely more strongly absorbed by the P3HT, which resulted in the red particles mentioned in Chapter 3. This is also consistent with the grazing-incidence broadband defocused imaging study. By comparing the defocused pattern of the different SOP systems with defocused patterns reported in the literature, it is concluded that for a thin active layer, most NPs demonstrate out-of-plane dipoles whereas for thicker spacers more horizontal components are observed. Particularly for P3HT, at 50-nm-thickness, most AuNPs exhibited in-plane dipoles.<sup>161</sup>

However, due to the broadband nature of the supercontinuum laser, we were not able to distinguish the mode origin of the defocused pattern. In other words, the same defocused pattern could be generated from different coupling modes. To investigate the defocused pattern and the wavelength dependence of the coupling modes, monochromatic excitation using different laser source could be conducted and is planned in future work. Specifically, we will use a similar experimental set-up described in Section 4.3.1 while exciting the modes only at specific wavelengths matching the individual DF scattering peaks and probe the defocused pattern. The results will be compared with the defocused patterns obtained by broadband excitation to see the difference.

Since the ultimate goal of our investigations is to use the patterned nanostructure or the SOP system to enhance the efficiency of thin-film organic photovoltaics, an aspect which has not been accomplished in the thesis is device building and electrical measurements to study the effects of gap modes on the power conversion efficiency of solar cells. Specifically, a SOP-based organic solar cell should be fabricated with proper electrodes and buffer layers. Then different gap modes can be excited separately at particular wavelengths and the resulting power conversion efficiencies can be recorded and compared.

Beyond these studies, an additional consideration for future experimental validation of the partial embedding of nanoparticles in conjugated polymer films, is solvent vapor annealing (SVA) treatment of the conjugated polymer film. SVA has been largely used to manipulate the morphology of polymer-fullerene bulk heterojunction thin-films to

improve the efficiency of photovoltaics.<sup>162,163</sup> Upon immersing the conjugated polymer thin-film in the solvent vapor, not only will the crystalline domains and morphology of the film will be re-organized, but also the film will become swollen, which should either promote embedding of AuNPs or increase the separation distance between the AuNPs and the underlying metal film. This may shed further insights into the mechanism of the partial embedding of AuNPs. Before and after the SVA treatment, targeted DF and AFM studies of the SOP samples will be conducted to compare the scattering color and heights of AuNPs.

The ternary blend system reported in Chapter 5 has the potential to enable an alternative to the stacked tandem organic photovoltaic device configuration with respect to overcoming the inherently narrow absorption bands of organic photovoltaic absorber materials. The thin-film ternary blend exhibited broadband absorption ( $> 450$  nm) and  $>90\%$  efficient energy/charge transfer between the components within the blend. While polythiophene and the phthalocyanine derivative exhibited strongly overlapping emission and absorption bands, respectively, they exhibited relatively poor mixing. This resulted in inhomogeneous energy transfer between the two materials in the blended films with a rapid direct energy transfer in  $\sim 410$  fs and in addition to a much slower decay time of 17 ps. However, introduction of a relatively small fraction ( $\sim 10\%$  by volume) of polyfluorene improved mixing of the materials in the ternary blend and resulted in an increase in the efficiency of charge/electron transfer between polythiophene and the phthalocyanine derivative.

One key aspect that this body of work did not account for is the definitive separation of energy transfer (ET) and charge transfer (CT) processes in the ternary blend system. To accomplish this, more time-resolved pump-probe measurements are required. Species like the free polaron, charge transfer exciton and bound exciton all have characteristic decay times and wavelengths which could provide us with a practical way to study the ET/CT mechanisms. Additionally, in the ternary system, the absorption band of PFO has poor overlap with that of P3HT, which results in a non-continuum collective absorption bands of the ternary blend. In that regard, alternative polymers need to be considered to establish a more efficiently absorbing ternary blend. For example, the absorption band of F8BT ranges from 400 nm to 520 nm, which connects well with the absorption band of P3HT, which would allow for improved total absorption spectrum of the ternary blend. Additionally, the emission band of F8BT has better overlap with the absorption of P3HT, which should be a better substitute to study. Eventually, the ternary blend will be applied in a photovoltaic device and EQE measurements will be conducted to confirm and utilize the FRET transfer amongst the blends.



## Bibilography

- 1 Q.H.Park. Optical antennas and plasmonics. *Contemporary Physics* **50**, 407-423 (2009).
- 2 Willner, A. E. *et al.* Optics and Photonics: Key Enabling Technologies. *Proceedings of the IEEE* **100**, 1604-1643 (2012).
- 3 Einstein, A. Über einen die Erzeugung und Verwandlung des Lichtes betreffenden heuristischen Gesichtspunkt. *Annalen der Physik* **322**, 132-148 (1905).
- 4 Maxwell, J. C. A Dynamical Theory of the Electromagnetic Field. *Proceedings of the Royal Society of London* **13**, 531-536 (1863).
- 5 Ranger, M., Rondeau, D. & Leclerc, M. New well-defined poly (2, 7-fluorene) derivatives: photoluminescence and base doping. *Macromolecules* **30**, 7686-7691 (1997).
- 6 Shirakawa, H., Louis, E. J., MacDiarmid, A. G., Chiang, C. K. & Heeger, A. J. Synthesis of electrically conducting organic polymers: halogen derivatives of polyacetylene,(CH) x. *Journal of the Chemical Society, Chemical Communications*, 578-580 (1977).
- 7 Sirringhaus, H., Tessler, N. & Friend, R. H. Integrated optoelectronic devices based on conjugated polymers. *Science* **280**, 1741-1744 (1998).
- 8 Carpi, F. & De Rossi, D. Colours from electroactive polymers: Electrochromic, electroluminescent and laser devices based on organic materials. *Optics & Laser Technology* **38**, 292-305 (2006).
- 9 Na, S.-I. *et al.* Fully spray-coated ITO-free organic solar cells for low-cost power generation. *Solar Energy Materials and Solar Cells* **94**, 1333-1337 (2010).
- 10 Müller, C. D. *et al.* Multi-colour organic light-emitting displays by solution processing. *nature* **421**, 829-833 (2003).
- 11 Tekin, E., Holder, E., Kozodaev, D. & Schubert, U. S. Controlled Pattern Formation of Poly [2 - methoxy - 5 - (2 ' - ethylhexyloxy) - 1, 4 - phenylenevinylene](MEH - PPV) by Ink - Jet Printing. *Advanced Functional Materials* **17**, 277-284 (2007).
- 12 Jørgensen, M. *et al.* Stability of polymer solar cells. *Advanced materials* **24**, 580-612 (2012).
- 13 Scholes, G. D. & Rumbles, G. Excitons in nanoscale systems. *Nature materials* **5**, 683-696 (2006).
- 14 Moore, E., Gherman, B. & Yaron, D. Coulomb screening and exciton binding energies in conjugated polymers. *The Journal of chemical physics* **106**, 4216-4227 (1997).
- 15 Campoy - Quiles, M. *et al.* Ellipsometric characterization of the optical constants of polyfluorene gain media. *Advanced Functional Materials* **15**, 925-933 (2005).

- 16 Brédas, J. L. & Silbey, R. *Conjugated polymers: the novel science and technology of highly conducting and nonlinear optically active materials*. (Springer Science & Business Media, 2012).
- 17 Ariu, M. *et al.* The effect of morphology on the temperature-dependent photoluminescence quantum efficiency of the conjugated polymer poly (9, 9-dioctylfluorene). *Journal of Physics: Condensed Matter* **14**, 9975 (2002).
- 18 Asada, K., Kobayashi, T. & Naito, H. Control of effective conjugation length in polyfluorene thin films. *Japanese journal of applied physics* **45**, L247 (2006).
- 19 Piris, J. *et al.* Photogeneration and ultrafast dynamics of excitons and charges in P3HT/PCBM blends. *The Journal of Physical Chemistry C* **113**, 14500-14506 (2009).
- 20 Tirapattur, S. *et al.* Spectroscopic study of intermolecular interactions in various oligofluorenes: Precursors of light-emitting polymers. *The Journal of Physical Chemistry B* **106**, 8959-8966 (2002).
- 21 Redecker, M., Bradley, D., Inbasekaran, M. & Woo, E. Mobility enhancement through homogeneous nematic alignment of a liquid-crystalline polyfluorene. *Applied physics letters* **74**, 1400 (1999).
- 22 Grell, M., Bradley, D., Ungar, G., Hill, J. & Whitehead, K. Interplay of physical structure and photophysics for a liquid crystalline polyfluorene. *Macromolecules* **32**, 5810-5817 (1999).
- 23 Grell, M. *et al.* Chain geometry, solution aggregation and enhanced dichroism in the liquidcrystalline conjugated polymer poly (9, 9 - dioctylfluorene). *Acta Polymerica* **49**, 439-444 (1998).
- 24 Chen, S., Chou, H., Su, A. & Chen, S. Molecular Packing in Crystalline Poly (9, 9-di-n-octyl-2, 7-fluorene). *Macromolecules* **37**, 6833-6838 (2004).
- 25 Chen, S.-H., Su, A.-C. & Chen, S.-A. Axialitic Morphology of Poly (9, 9-di-n-octyl-2, 7-fluorene). *Macromolecules* **39**, 9143-9149 (2006).
- 26 Chen, S., Su, A., Su, C. & Chen, S. Crystalline forms and emission behavior of poly (9, 9-di-n-octyl-2, 7-fluorene). *Macromolecules* **38**, 379-385 (2005).
- 27 Korovyanko, O. & Vardeny, Z. Film morphology and ultrafast photoexcitation dynamics in polyfluorene. *Chemical physics letters* **356**, 361-367 (2002).
- 28 Huang, Y.-S., Gierschner, J., Schmidtke, J. P., Friend, R. H. & Beljonne, D. Tuning interchain and intrachain interactions in polyfluorene copolymers. *Physical Review B* **84**, 205311 (2011).
- 29 Polman, A. Plasmonics applied. *Science* **322**, 868-869 (2008).
- 30 Forrest, S. R. & Thompson, M. E. Introduction: organic electronics and optoelectronics. *Chemical Reviews* **107**, 923-925 (2007).
- 31 Tang, C. W. & VanSlyke, S. A. Organic electroluminescent diodes. *Applied physics letters* **51**, 913-915 (1987).
- 32 Burroughes, J. *et al.* Light-emitting diodes based on conjugated polymers. *nature* **347**, 539-541 (1990).

- 33 Chapin, D. M., Fuller, C. & Pearson, G. A new silicon p - n junction photocell for converting solar radiation into electrical power. *Journal of Applied Physics* **25**, 676-677 (1954).
- 34 Hegedus, S. Thin film solar modules: the low cost, high throughput and versatile alternative to Si wafers. *Progress in Photovoltaics: Research and Applications* **14**, 393-411 (2006).
- 35 Slaoui, A. & Collins, R. T. Advanced inorganic materials for photovoltaics. *MRS bulletin* **32**, 211-218 (2007).
- 36 Tang, C. W. Two - layer organic photovoltaic cell. *Applied physics letters* **48**, 183-185 (1986).
- 37 Yu, G., Gao, J., Hummelen, J. C., Wudl, F. & Heeger, A. J. Polymer photovoltaic cells: Enhanced efficiencies via a network of internal donor-acceptor heterojunctions. *Science* **270**, 1789 (1995).
- 38 Halls, J. *et al.* Efficient photodiodes from interpenetrating polymer networks. (1995).
- 39 Scharber, M. & Sariciftci, N. Efficiency of bulk-heterojunction organic solar cells. *Progress in polymer science* **38**, 1929-1940 (2013).
- 40 Li, G., Zhu, R. & Yang, Y. Polymer solar cells. *Nature Photonics* **6**, 153-161 (2012).
- 41 Rajaram, S., Armstrong, P. B., Kim, B. J. & Fréchet, J. M. Effect of addition of a diblock copolymer on blend morphology and performance of poly (3-hexylthiophene): perylene diimide solar cells. *Chemistry of materials* **21**, 1775-1777 (2009).
- 42 Woo, C. H., Holcombe, T. W., Unruh, D. A., Sellinger, A. & Fréchet, J. M. Phenyl vs alkyl polythiophene: a solar cell comparison using a vinazene derivative as acceptor. *Chemistry of materials* **22**, 1673-1679 (2010).
- 43 Zhou, Y. *et al.* A Non - Fullerene Small Molecule as Efficient Electron Acceptor in Organic Bulk Heterojunction Solar Cells. *Advanced materials* **24**, 957-961 (2012).
- 44 McNeill, C. R. *et al.* Efficient polythiophene/polyfluorene copolymer bulk heterojunction photovoltaic devices: device physics and annealing effects. *Advanced Functional Materials* **18**, 2309-2321 (2008).
- 45 Schwenn, P. E. *et al.* A Small Molecule Non - fullerene Electron Acceptor for Organic Solar Cells. *Advanced Energy Materials* **1**, 73-81 (2011).
- 46 Pfeiffer, M. *et al.* Doped organic semiconductors: Physics and application in light emitting diodes. *Organic Electronics* **4**, 89-103 (2003).
- 47 Peters, C. H. *et al.* High efficiency polymer solar cells with long operating lifetimes. *Advanced Energy Materials* **1**, 491-494 (2011).
- 48 Mateker, W. R., Sachs-Quintana, I., Burkhard, G. F., Cheacharoen, R. & McGehee, M. D. Minimal long-term intrinsic degradation observed in a polymer solar cell illuminated in an oxygen-free environment. *Chemistry of materials* **27**, 404-407 (2015).

- 49 Zhang, F. *et al.* Recent development of the inverted configuration organic solar cells. *Solar Energy Materials and Solar Cells* **95**, 1785-1799 (2011).
- 50 Green, M. A., Emery, K., Hishikawa, Y., Warta, W. & Dunlop, E. D. Solar cell efficiency tables (Version 45). *Progress in Photovoltaics: Research and Applications* **23**, 1-9 (2015).
- 51 O'Carroll, D. M. *et al.* Conjugated polymer-based photonic nanostructures. *Polymer Chemistry* **4**, 5181-5196 (2013).
- 52 Campbell, P. & Green, M. A. Light trapping properties of pyramidally textured surfaces. *Journal of Applied Physics* **62**, 243-249 (1987).
- 53 Yu, Z., Raman, A. & Fan, S. Fundamental limit of nanophotonic light trapping in solar cells. *Proceedings of the National Academy of Sciences* **107**, 17491-17496 (2010).
- 54 Fan, X., Zheng, W. & Singh, D. J. Light scattering and surface plasmons on small spherical particles. *Light: Science & Applications* **3**, e179 (2014).
- 55 Bohren, C. F. & Huffman, D. R. *Absorption and scattering of light by small particles*. (John Wiley & Sons, 2008).
- 56 Bohren, C. F. How can a particle absorb more than the light incident on it? *American Journal of Physics* **51**, 323-327 (1983).
- 57 Cortie, M. B., Xu, X., Chowdhury, H., Zareie, H. & Smith, G. in *Smart Materials, Nano-, and Micro-Smart Systems*. 565-573 (International Society for Optics and Photonics).
- 58 Pissuwan, D., Valenzuela, S. M. & Cortie, M. B. Therapeutic possibilities of plasmonically heated gold nanoparticles. *TRENDS in Biotechnology* **24**, 62-67 (2006).
- 59 Pillai, S., Catchpole, K., Trupke, T. & Green, M. Surface plasmon enhanced silicon solar cells. *Journal of Applied Physics* **101**, 093105 (2007).
- 60 Yu, E. & Van De Lagemaat, J. Photon management for photovoltaics. *MRS bulletin* **36**, 424-428 (2011).
- 61 Atwater, H. A. & Polman, A. Plasmonics for improved photovoltaic devices. *Nature materials* **9**, 205-213 (2010).
- 62 Ferry, V. E., Munday, J. N. & Atwater, H. A. Design considerations for plasmonic photovoltaics. *Advanced materials* **22**, 4794-4808 (2010).
- 63 Schaadt, D., Feng, B. & Yu, E. Enhanced semiconductor optical absorption via surface plasmon excitation in metal nanoparticles. *Applied physics letters* **86**, 063106 (2005).
- 64 Ferry, V. E., Sweatlock, L. A., Pacifici, D. & Atwater, H. A. Plasmonic nanostructure design for efficient light coupling into solar cells. *Nano letters* **8**, 4391-4397 (2008).
- 65 Akimov, Y. A., Koh, W. S. & Ostrikov, K. Enhancement of optical absorption in thin-film solar cells through the excitation of higher-order nanoparticle plasmon modes. *Optics express* **17**, 10195-10205 (2009).

- 66 Gaynor, W., Lee, J.-Y. & Peumans, P. Fully solution-processed inverted polymer solar cells with laminated nanowire electrodes. *ACS nano* **4**, 30-34 (2009).
- 67 Li, X. *et al.* Polarization-independent efficiency enhancement of organic solar cells by using 3-dimensional plasmonic electrode. *Applied physics letters* **102**, 153304 (2013).
- 68 Bai, W. *et al.* Broadband short-range surface plasmon structures for absorption enhancement in organic photovoltaics. *Optics express* **18**, A620-A630 (2010).
- 69 Bai, W. *et al.* Double plasmonic structure design for broadband absorption enhancement in molecular organic solar cells. *Journal of Photonics for Energy* **1**, 011121-011121-011112 (2011).
- 70 Haes, A. J., Zou, S., Schatz, G. C. & Van Duyne, R. P. A nanoscale optical biosensor: the long range distance dependence of the localized surface plasmon resonance of noble metal nanoparticles. *The Journal of Physical Chemistry B* **108**, 109-116 (2004).
- 71 Barnes, W. L. Surface plasmon–polariton length scales: a route to sub-wavelength optics. *Journal of optics A: pure and applied optics* **8**, S87 (2006).
- 72 Cooling, N. *et al.* A study of the factors influencing the performance of ternary MEH-PPV: Porphyrin: PCBM heterojunction devices: A steric approach to controlling charge recombination. *Solar Energy Materials and Solar Cells* **95**, 1767-1774 (2011).
- 73 Belcher, W., Wagner, K. & Dastoor, P. The effect of porphyrin inclusion on the spectral response of ternary P3HT: porphyrin: PCBM bulk heterojunction solar cells. *Solar Energy Materials and Solar Cells* **91**, 447-452 (2007).
- 74 Yu, B., Goodman, S., Abdelaziz, A. & O'Carroll, D. M. Light-management in ultra-thin polythiophene films using plasmonic monopole nanoantennas. *Applied Physics Letters* **101**, 151106 (2012).
- 75 Mubeen, S. *et al.* Plasmonic properties of gold nanoparticles separated from a gold mirror by an ultrathin oxide. *Nano letters* **12**, 2088-2094 (2012).
- 76 Fischer, U. C. & Pohl, D. W. Observation of Single-Particle Plasmons by Near-Field Optical Microscopy. *Physical review letters* **62**, 458-461 (1989).
- 77 Abe, H., Manzel, K., Schulze, W., Moskovits, M. & DiLella, D. Surface - enhanced Raman spectroscopy of CO adsorbed on colloidal silver particles. *The Journal of Chemical Physics* **74**, 792-797 (1981).
- 78 Hutter, E. *et al.* Role of substrate metal in gold nanoparticle enhanced surface plasmon resonance imaging. *The Journal of Physical Chemistry B* **105**, 8-12 (2001).
- 79 Mock, J. J., Hill, R. T., Tsai, Y.-J., Chilkoti, A. & Smith, D. R. Probing dynamically tunable localized surface plasmon resonances of film-coupled nanoparticles by evanescent wave excitation. *Nano letters* **12**, 1757-1764 (2012).
- 80 Tsuboi, K., Fukuba, S., Naraoka, R., Fujita, K. & Kajikawa, K. Multichannel biosensing platform of surface-immobilized gold nanospheres for linear and nonlinear optical imaging. *Applied optics* **46**, 4486-4490 (2007).

- 81 Xu, H. *et al.* Unified treatment of fluorescence and Raman scattering processes near metal surfaces. *Physical review letters* **93**, 243002 (2004).
- 82 Jean, J., Brown, P. R., Jaffe, R. L., Buonassisi, T. & Bulović, V. Pathways for solar photovoltaics. *Energy & Environmental Science* **8**, 1200-1219 (2015).
- 83 Wind, M., Vlieger, J. & Bedeaux, D. The polarizability of a truncated sphere on a substrate I. *Physica A: Statistical Mechanics and its Applications* **141**, 33-57 (1987).
- 84 Ruppin, R. Optical absorption by a small sphere above a substrate with inclusion of nonlocal effects. *Physical Review B* **45**, 11209 (1992).
- 85 Mock, J. J. *et al.* Distance-dependent plasmon resonant coupling between a gold nanoparticle and gold film. *Nano letters* **8**, 2245-2252 (2008).
- 86 Hu, M., Ghoshal, A., Marquez, M. & Kik, P. G. Single Particle Spectroscopy Study of Metal-Film-Induced Tuning of Silver Nanoparticle Plasmon Resonances†. *The Journal of Physical Chemistry C* **114**, 7509-7514 (2010).
- 87 Lumdee, C., Toroghi, S. & Kik, P. G. Post-fabrication voltage controlled resonance tuning of nanoscale plasmonic antennas. *Acs Nano* **6**, 6301-6307 (2012).
- 88 Hutter, T., Elliott, S. R. & Mahajan, S. Interaction of metallic nanoparticles with dielectric substrates: effect of optical constants. *Nanotechnology* **24**, 035201 (2012).
- 89 Frederiksen, M., Bochenkov, V. E., Ogaki, R. & Sutherland, D. S. Onset of bonding plasmon hybridization preceded by gap modes in dielectric splitting of metal disks. *Nano letters* **13**, 6033-6039 (2013).
- 90 Yu, B., Goodman, S., Abdelaziz, A., apos & Carroll, D. M. Light-management in ultra-thin polythiophene films using plasmonic monopole nanoantennas. *Applied physics letters* **101**, 151106, doi:doi:<http://dx.doi.org/10.1063/1.4754665> (2012).
- 91 Bharadwaj, P., Deutsch, B. & Novotny, L. Optical Antennas. *Adv. Opt. Photon.* **1**, 438-483, doi:10.1364/aop.1.000438 (2009).
- 92 Novotny, L. & van Hulst, N. Antennas for light. *Nat Photon* **5**, 83-90 (2011).
- 93 Coakley, K. M. *et al.* Enhanced Hole Mobility in Regioregular Polythiophene Infiltrated in Straight Nanopores. *Advanced Functional Materials* **15**, 1927-1932, doi:10.1002/adfm.200500364 (2005).
- 94 Greenham, N. C. *et al.* Measurement of absolute photoluminescence quantum efficiencies in conjugated polymers. *Chemical Physics Letters* **241**, 89-96, doi:[http://dx.doi.org/10.1016/0009-2614\(95\)00584-Q](http://dx.doi.org/10.1016/0009-2614(95)00584-Q) (1995).
- 95 Piris, J. *et al.* Photogeneration and Ultrafast Dynamics of Excitons and Charges in P3HT/PCBM Blends. *The Journal of Physical Chemistry C* **113**, 14500-14506, doi:10.1021/jp904229q (2009).
- 96 Mohammadi, A., Sandoghdar, V. & Agio, M. Gold nanorods and nanospheroids for enhancing spontaneous emission. *New Journal of Physics* **10**, 105015 (2008).
- 97 Pellegrini, G., Mattei, G. & Mazzoldi, P. Tunable, directional and wavelength selective plasmonic nanoantenna arrays. *Nanotechnology* **20**, 065201 (2009).
- 98 Dorfmueller, J. *et al.* Plasmonic nanowire antennas: experiment, simulation, and theory. *Nano letters* **10**, 3596-3603 (2010).

- 99 Taminiau, T. H., Segerink, F. B., Moerland, R. J., Kuipers, L. K. & van Hulst, N. F. Near-field driving of an optical monopole antenna. *Journal of Optics A: Pure and Applied Optics* **9**, S315 (2007).
- 100 Bharadwaj, P., Beams, R. & Novotny, L. Nanoscale spectroscopy with optical antennas. *Chemical Science* **2**, 136-140 (2011).
- 101 Taminiau, T. H., Moerland, R. J., Segerink, F. B., Kuipers, L. & van Hulst, N. F.  $\lambda/4$  resonance of an optical monopole antenna probed by single molecule fluorescence. *Nano letters* **7**, 28-33 (2007).
- 102 Ahmed, A. & Gordon, R. Directivity enhanced Raman spectroscopy using nanoantennas. *Nano letters* **11**, 1800-1803 (2011).
- 103 Bonod, N., Tayeb, G., Maystre, D., Enoch, S. & Popov, E. Total absorption of light by lamellar metallic gratings. *Optics express* **16**, 15431-15438 (2008).
- 104 Yamamoto, N., Ohtani, S. & García de Abajo, F. J. Gap and Mie plasmons in individual silver nanospheres near a silver surface. *Nano letters* **11**, 91-95 (2010).
- 105 Russell, K. J. & Hu, E. L. Gap-mode plasmonic nanocavity. *Applied Physics Letters* **97**, 163115 (2010).
- 106 O'Carroll, D. M., Hofmann, C. E. & Atwater, H. A. Conjugated polymer/metal nanowire heterostructure plasmonic antennas. *Advanced Materials* **22**, 1223-1227 (2010).
- 107 Jain, P. K. & El-Sayed, M. A. Plasmonic coupling in noble metal nanostructures. *Chemical Physics Letters* **487**, 153-164 (2010).
- 108 Schuck, P., Fromm, D., Sundaramurthy, A., Kino, G. & Moerner, W. Improving the mismatch between light and nanoscale objects with gold bowtie nanoantennas. *Physical review letters* **94**, 017402 (2005).
- 109 Halas, N. J., Lal, S., Chang, W.-S., Link, S. & Nordlander, P. Plasmons in strongly coupled metallic nanostructures. *Chemical reviews* **111**, 3913-3961 (2011).
- 110 Taminiau, T., Stefani, F., Segerink, F. & Van Hulst, N. Optical antennas direct single-molecule emission. *Nature Photonics* **2**, 234-237 (2008).
- 111 Kim, Y. *et al.* A strong regioregularity effect in self-organizing conjugated polymer films and high-efficiency polythiophene: fullerene solar cells. *nature materials* **5**, 197-203 (2006).
- 112 Günes, S., Neugebauer, H. & Sariciftci, N. S. Conjugated polymer-based organic solar cells. *Chemical reviews* **107**, 1324-1338 (2007).
- 113 Köhler, A., Wilson, J. S. & Friend, R. H. Fluorescence and Phosphorescence in Organic Materials. *Advanced Materials* **14**, 701-707, doi:10.1002/1521-4095(20020517)14:10<701::aid-adma701>3.0.co;2-4 (2002).
- 114 Clarke, T. M. & Durrant, J. R. Charge photogeneration in organic solar cells. *Chemical reviews* **110**, 6736-6767 (2010).
- 115 Palik, E. D. *Handbook of optical constants of solids*. Vol. 3 (Academic press, 1998).

- 116 Jansson, R., Arwin, H., Gustafsson, G. & Inganäs, O. Thin films of poly (3-hexylthiophene) studied with spectroscopic ellipsometry. *Synthetic Metals* **28**, 371-376 (1989).
- 117 Lei, D. Y. *et al.* Revealing plasmonic gap modes in particle-on-film systems using dark-field spectroscopy. *Acs Nano* **6**, 1380-1386 (2012).
- 118 Okamoto, T. & Yamaguchi, I. Optical absorption study of the surface plasmon resonance in gold nanoparticles immobilized onto a gold substrate by self-assembly technique. *The Journal of Physical Chemistry B* **107**, 10321-10324 (2003).
- 119 Pinchuk, A., Hilger, A., von Plessen, G. & Kreibig, U. Substrate effect on the optical response of silver nanoparticles. *Nanotechnology* **15**, 1890 (2004).
- 120 Knight, M. W., Wu, Y., Lassiter, J. B., Nordlander, P. & Halas, N. J. Substrates matter: influence of an adjacent dielectric on an individual plasmonic nanoparticle. *Nano letters* **9**, 2188-2192 (2009).
- 121 Myroshnychenko, V. *et al.* Modelling the optical response of gold nanoparticles. *Chemical Society Reviews* **37**, 1792-1805 (2008).
- 122 Noguez, C. Surface plasmons on metal nanoparticles: the influence of shape and physical environment. *The Journal of Physical Chemistry C* **111**, 3806-3819 (2007).
- 123 Lumdee, C., Yun, B. & Kik, P. G. Effect of surface roughness on substrate-tuned gold nanoparticle gap plasmon resonances. *Nanoscale* **7**, 4250-4255 (2015).
- 124 Catchpole, K. & Polman, A. Design principles for particle plasmon enhanced solar cells. *Applied Physics Letters* **93**, 191113 (2008).
- 125 Nemes, C. T., Vijapurapu, D. K., Petoukhoff, C. E., Cheung, G. Z. & O'Carroll, D. M. Absorption and scattering effects by silver nanoparticles near the interface of organic/inorganic semiconductor tandem films. *Journal of nanoparticle research* **15**, 1-13 (2013).
- 126 Xiao, L., Qiao, Y., He, Y. & Yeung, E. S. Three dimensional orientational imaging of nanoparticles with darkfield microscopy. *Analytical chemistry* **82**, 5268-5274 (2010).
- 127 Li, T. *et al.* Three-dimensional orientation sensors by defocused imaging of gold nanorods through an ordinary wide-field microscope. *ACS nano* **6**, 1268-1277 (2012).
- 128 Raether, H. (Berlin: Springer, 1988).
- 129 Ciraci, C. *et al.* Probing the ultimate limits of plasmonic enhancement. *Science* **337**, 1072-1074 (2012).
- 130 Hahm, S.-W., Hwang, H.-S., Kim, D. & Khang, D.-Y. Buckling-based measurements of mechanical moduli of thin films. *Electronic Materials Letters* **5**, 157-168 (2009).
- 131 Matsuura, T., Nakajima, M. & Shimoyama, Y. Growth of self-assembled monolayer of thiophene on gold surface: An infrared spectroscopic study. *Japanese journal of applied physics* **40**, 6945 (2001).



- 132 Dedecker, P. *et al.* Defocused Wide - field Imaging Unravels Structural and Temporal Heterogeneity in Complex Systems. *Advanced materials* **21**, 1079-1090 (2009).
- 133 Heydari, E., Pastoriza-Santos, I., Flehr, R., Liz-Marzán, L. M. & Stumpe, J. Nanoplasmonic enhancement of the emission of semiconductor polymer composites. *The Journal of Physical Chemistry C* **117**, 16577-16583 (2013).
- 134 Patrick, G. N. & Fernando, A. C. Organic photovoltaics: principles and techniques for nanometre scale characterization. *Nanotechnology* **21**, 492001 (2010).
- 135 Chen, Y.-C., Hsu, C.-Y., Lin, R. Y.-Y., Ho, K.-C. & Lin, J. T. Materials for the Active Layer of Organic Photovoltaics: Ternary Solar Cell Approach. *ChemSusChem* **6**, 20-35, doi:10.1002/cssc.201200609 (2013).
- 136 Itskos, G. *et al.* Optical Properties of Organic Semiconductor Blends with Near - Infrared Quantum - Dot Sensitizers for Light Harvesting Applications. *Advanced Energy Materials* **1**, 802-812 (2011).
- 137 Groves, C. Suppression of geminate charge recombination in organic photovoltaic devices with a cascaded energy heterojunction. *Energy & Environmental Science* **6**, 1546-1551 (2013).
- 138 Kim, H., Shin, M. & Kim, Y. Distinct annealing temperature in polymer: fullerene: polymer ternary blend solar cells. *The Journal of Physical Chemistry C* **113**, 1620-1623 (2009).
- 139 Kim, Y. *et al.* Organic photovoltaic devices based on blends of regioregular poly (3-hexylthiophene) and poly (9, 9-dioctylfluorene-co-benzothiadiazole). *Chemistry of Materials* **16**, 4812-4818 (2004).
- 140 Koppe, M. *et al.* Near IR sensitization of organic bulk heterojunction solar cells: towards optimization of the spectral response of organic solar cells. *Advanced Functional Materials* **20**, 338-346 (2010).
- 141 Sharma, G., Singh, S. P., Roy, M. & Mikroyannidis, J. Solution processed bulk heterojunction polymer solar cells with low band gap DPP-CN small molecule sensitizer. *Organic Electronics* **13**, 1756-1762 (2012).
- 142 Choi, J. W. *et al.* Solution-processed bulk heterojunction organic solar cells with high polarity small molecule sensitizer. *Solar Energy Materials and Solar Cells* **95**, 2069-2076 (2011).
- 143 Dou, L. *et al.* Synthesis of 5 H-dithieno [3, 2-b: 2' , 3' -d] pyran as an electron-rich building block for donor - acceptor type low-bandgap polymers. *Macromolecules* **46**, 3384-3390 (2013).
- 144 Liang, Y. *et al.* For the bright future—bulk heterojunction polymer solar cells with power conversion efficiency of 7.4%. *Advanced Materials* **22** (2010).
- 145 Kanimozhi, C., Balraju, P., Sharma, G. & Patil, S. Synthesis of diketopyrrolopyrrole containing copolymers: a study of their optical and photovoltaic properties. *The Journal of Physical Chemistry B* **114**, 3095-3103 (2010).

- 146 Kim, J.-H. *et al.* Thieno [3, 2-b] thiophene-substituted benzo [1, 2-b: 4, 5-b' ] dithiophene as a promising building block for low bandgap semiconducting polymers for high-performance single and tandem organic photovoltaic cells. *Chemistry of Materials* **26**, 1234-1242 (2014).
- 147 Ameri, T., Li, N. & Brabec, C. J. Highly efficient organic tandem solar cells: a follow up review. *Energy & Environmental Science* **6**, 2390-2413 (2013).
- 148 Hori, T. *et al.* Non-peripheral octahexylphthalocyanine doping effects in bulk heterojunction polymer solar cells. *Organic Electronics* **13**, 335-340 (2012).
- 149 Hori, T. *et al.* Bulk heterojunction organic solar cells utilizing 1, 4, 8, 11, 15, 18, 22, 25-octahexylphthalocyanine. *Solar Energy Materials and Solar Cells* **95**, 3087-3092 (2011).
- 150 Yang, F., Lunt, R. R. & Forrest, S. R. Simultaneous heterojunction organic solar cells with broad spectral sensitivity. *Applied Physics Letters* **92**, 053310 (2008).
- 151 Feron, K., Belcher, W. J., Fell, C. J. & Dastoor, P. C. Organic solar cells: understanding the role of forster resonance energy transfer. *International journal of molecular sciences* **13**, 17019-17047 (2012).
- 152 Machui, F., Rathgeber, S., Li, N., Ameri, T. & Brabec, C. J. Influence of a ternary donor material on the morphology of a P3HT: PCBM blend for organic photovoltaic devices. *Journal of Materials Chemistry* **22**, 15570-15577 (2012).
- 153 Li, N., Machui, F., Waller, D., Koppe, M. & Brabec, C. J. Determination of phase diagrams of binary and ternary organic semiconductor blends for organic photovoltaic devices. *Solar Energy Materials and Solar Cells* **95**, 3465-3471 (2011).
- 154 Mor, G. K. *et al.* Visible to near-infrared light harvesting in TiO<sub>2</sub> nanotube array–P3HT based heterojunction solar cells. *Nano letters* **9**, 4250-4257 (2009).
- 155 Walker, B. *et al.* Nanoscale Phase Separation and High Photovoltaic Efficiency in Solution - Processed, Small - Molecule Bulk Heterojunction Solar Cells. *Advanced Functional Materials* **19**, 3063-3069 (2009).
- 156 Izumi, T., Kobashi, S., Takimiya, K., Aso, Y. & Otsubo, T. Synthesis and spectroscopic properties of a series of  $\beta$ -blocked long oligothiophenes up to the 96-mer: revaluation of effective conjugation length. *Journal of the American Chemical Society* **125**, 5286-5287 (2003).
- 157 Cadby, A. *et al.* Film morphology and photophysics of polyfluorene. *Physical Review B* **62**, 15604 (2000).
- 158 Lakowicz, J. R. *Principles of fluorescence spectroscopy*. (Springer Science & Business Media, 2013).
- 159 Shaw, P. E., Ruseckas, A. & Samuel, I. D. Exciton diffusion measurements in poly (3 - hexylthiophene). *Advanced Materials* **20**, 3516-3520 (2008).
- 160 Banerji, N., Cowan, S., Vauthey, E. & Heeger, A. J. Ultrafast relaxation of the poly (3-hexylthiophene) emission spectrum. *The Journal of Physical Chemistry C* **115**, 9726-9739 (2011).

- 161 Yu, B., Woo, J., Kong, M. & O'Carroll, D. M. Mode-specific study of nanoparticle-mediated optical interactions in an absorber/metal thin film system. *Nanoscale* **7**, 13196-13206, doi:10.1039/c5nr02217g (2015).
- 162 Verploegen, E., Miller, C. E., Schmidt, K., Bao, Z. & Toney, M. F. Manipulating the morphology of P3HT-PCBM bulk heterojunction blends with solvent vapor annealing. *Chemistry of materials* **24**, 3923-3931 (2012).
- 163 Sun, K. *et al.* The role of solvent vapor annealing in highly efficient air-processed small molecule solar cells. *Journal of Materials Chemistry A* **2**, 9048-9054 (2014).



## Appendix

$$y_0 + A_1 \times \exp\left(-\frac{x - x_0}{\tau_1}\right) + A_2 \times \exp\left(-\frac{x - x_0}{\tau_2}\right)$$

	A <sub>1</sub>	τ <sub>1</sub> (ps)	A <sub>2</sub>	τ <sub>2</sub> (ps)	A <sub>1</sub> +A <sub>2</sub>	y <sub>0</sub>
With Au	9.50E3±1.64E3	0.43 ±	4.37E3±1.57E3	4.96 ±2.77	1.387E4	1.00432E7
NR	68%	0.14	32%			
Without Au	5.66E3±0.88E3	0.39 ±0.12	5.22E3±0.79E3	4.95 ±1.21	1.088E4	8.5162E6
NR	52%		48%			

Table A1. The second order exponential decay fitting equation of 50-nm-thick P3HT film with or without AuNR present.  $\tau_1$  represents the fast component and  $\tau_2$  represents the slow component.  $A_1$  and  $A_2$  correspond to the amplitude of fast/slow component, respectively.

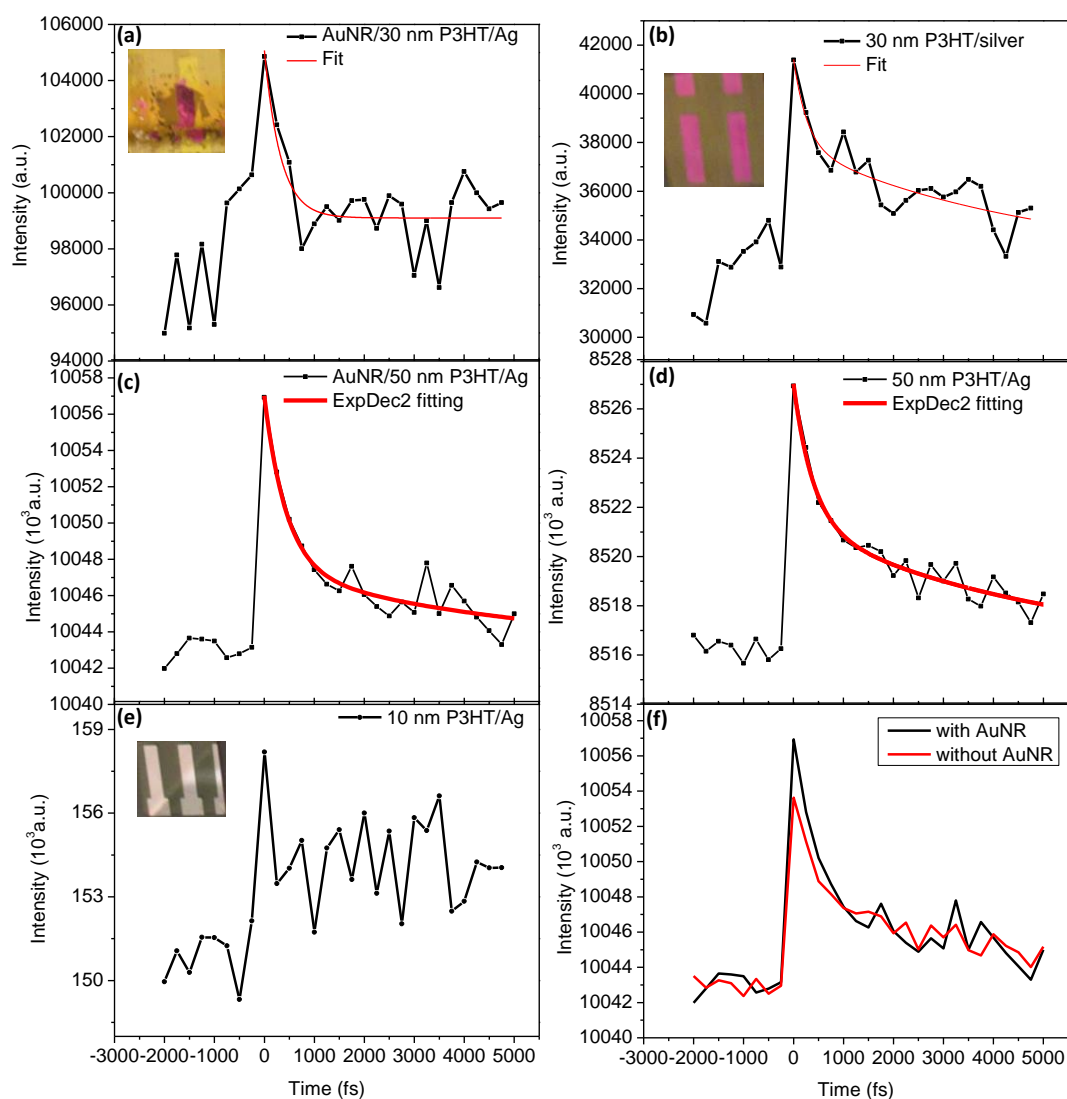


**Figure A1.** Time-resolved fluorescence decay profile of (a) AuNR/30-nm-thick P3HT/Ag film, (b) 30-nm-thick P3HT/Ag film, (c) AuNR/50-nm-thick P3HT/Ag film, (d) 50-nm-thick P3HT/Ag film and (e) 10-nm-thick P3HT/Ag film areas. (e) shows the comparison of fluorescence decay of 30-nm-thick P3HT between AuNR area and no AuNR area. Insets are the corresponding sample area (data acquired by Jianhua Bao).

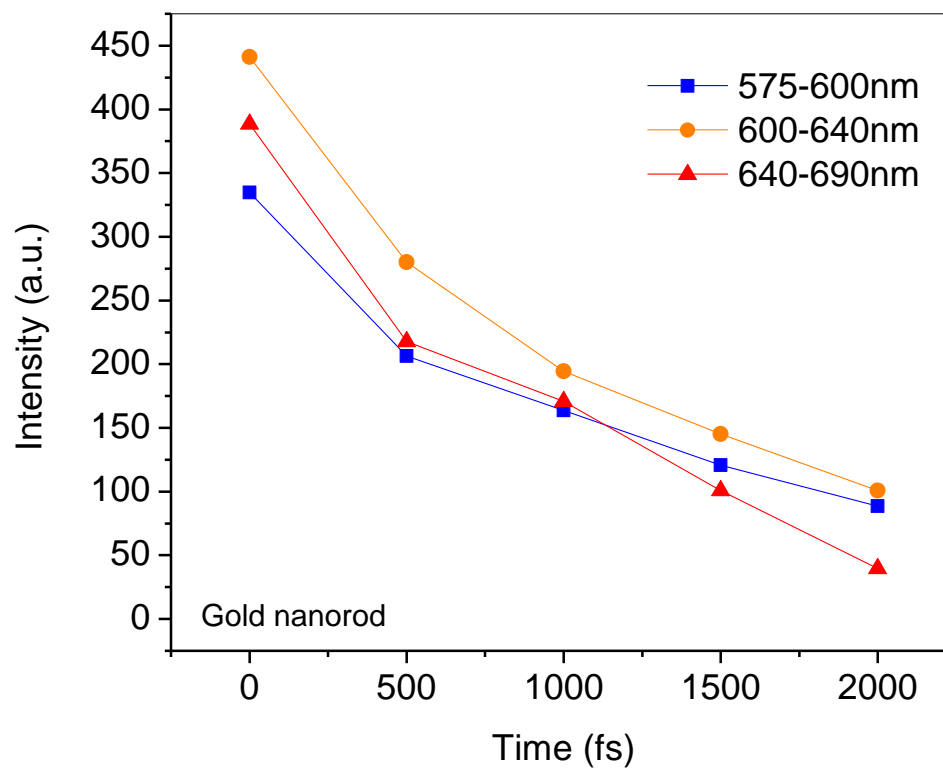


**Figure A2.** Integration of fluorescence intensity of AuNR/50-nm-thick P3HT/Ag film sample at different wavelength ranges for specific decay time.

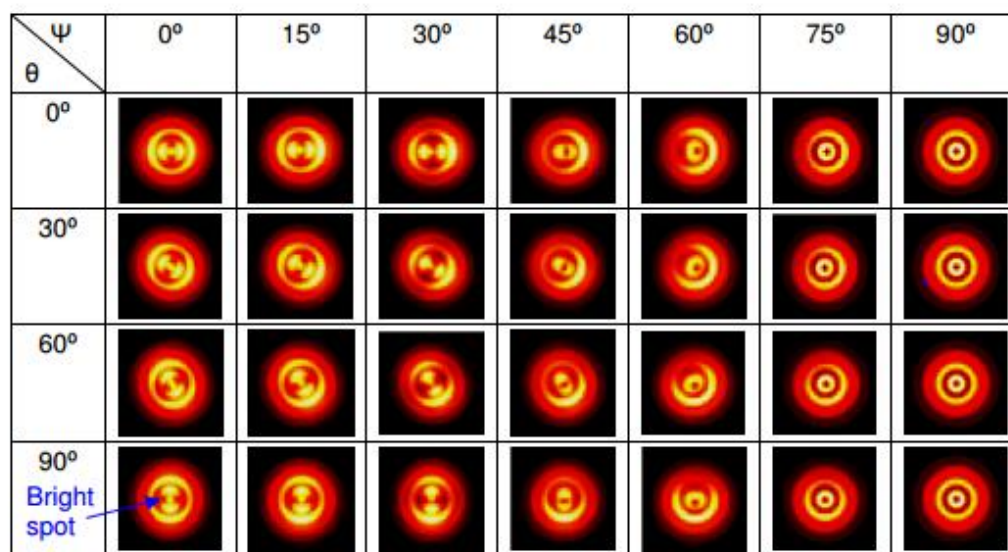


**Figure A3.** Calculated defocused images for AuNRs at a fixed defocusing distance of  $0.99 \mu\text{m}$  with different spatial orientations. The resolving ability for in-plane and out-of-plane angles can reach 1 degree [126]